2016

Formation of the Neoarchean Bad Vermillion Lake Anorthosite Complex and Spatially Associated Granitic Rocks at a Convergent Plate Margin, Superior Province, Western Ontario, Canada

Shuda Zhou
University of Windsor

Ali Polat
University of Windsor

Fred Longstaffe
The University of Western Ontario, flongsta@uwo.ca

Kunguang Yang
China University of Geosciences Wuhan

Brian J. Fryer
University of Windsor

See next page for additional authors

Authors
Shuda Zhou, Ali Polat, Fred Longstaffe, Kunguang Yang, Brian J. Fryer, and Crhis Weisener

Formation of the Neoarchean Bad Vermilion Lake Anorthosite Complex and Spatially Associated Granitic Rocks at a Convergent Plate Margin, Superior Province, Western Ontario, Canada

Shuda Zhou[a], Ali Polat[a,*], Fred J. Longstaffe[b], Kunguang Yang[c], Brian J. Fryer[a, d], Chris Weisener[a, d]

[a] Department of Earth and Environmental Sciences, University of Windsor, Windsor, ON, Canada N9B 3P4

[b] Department of Earth Sciences, The University of Western Ontario, London, N6A 5B7 ON, Canada

[c] Faculty of Earth Sciences, China University of Geosciences, Wuhan 430074, China

[d] Great Lakes Institute for Environmental Research, University of Windsor, Windsor, ON, Canada N9B 3P4

* Corresponding author. E-mail address: polat@uwindsor.ca (A. Polat).

Abstract

The Bad Vermilion Lake Anorthosite Complex (henceforth, the BVLA Complex) in western Ontario is one of the well-exposed, anorthosite-bearing, Archean layered intrusions in the Superior Province, Canada. This study presents new whole-rock major and trace element data for the various units of the Complex, oxygen isotope data for the anorthosite, and major and trace element data for the spatially associated granitic rocks intruding the BVLA Complex to constrain their petrogenetic and geodynamic origin. Zircons from granitic rocks have yielded a $^{207}Pb/^{206}Pb$ age of 2716 ± 18 Ma, constraining the minimum intrusion age of the Complex.

Despite deformation and greenschist facies metamorphism, primary igneous textures are locally well preserved in the BVLA Complex. Its whole-rock major and trace elemental compositions and the oxygen isotopic systematics appear not to have been substantially modified by deformation and metamorphism. Mantle-like oxygen isotope signatures and major and trace element compositions are inconsistent with significant crustal contamination of the BVLA Complex during its emplacement. The existence of primary calcic igneous plagioclase, coherent negative Nb anomalies (Nb/Nb*=0.08-0.88), and geochemical similarities between gabbros from the BVLA Complex and gabbros from Cenozoic arcs collectively suggest an intra-oceanic subduction zone geodynamic setting for the Complex. Near-flat REE patterns in the various units of the BVLA Complex suggest that they were derived from melting of a shallow source beneath a subarc mantle wedge. Trends in immobile major (e.g., MgO) and trace (e.g., Zr) element data indicate that the mineralogical composition of the Complex can be explained by fractional crystallization and accumulation of olivine, orthopyroxene, clinopyroxene, plagioclase and

possibly amphibole.

Compositionally, the bordering granitic rocks are A_2-type and strongly enriched in Th and REE (>100 times chondrite) and depleted of Ba, Sr, Eu and Ti. We suggest that they formed in a post-collisional, extensional, tectonic regime following emplacement of the BVLA Complex in an oceanic arc.

Key words: Bad Vermilion Lake Complex, Anorthosite, Archean, Oxygen Isotope, Zircon U-Pb dating

1. Introduction

Although Archean layered anorthosites and associated leucogabbros, gabbros and ultramafic rocks (Ashwal, 1993; Bédard et al., 2009; Polat et al., 2009, 2010, 2012; Leclerc et al., 2011; Hoffmann et al., 2012; Mohan et al., 2013) are volumetrically minor components of the preserved Archean crust, they occur in most Archean cratons (e.g., Superior Province, Greenland, South India) (Fig. 1). They are typically associated with greenstone belts and hold critical information on the petrogenetic and geodynamic processes that operated in the early Earth (Ashwal, 1993; Polat et al., 2009, 2010, 2012; Mohan et al., 2013).

The petrogenetic origin of Archean anorthosite complexes and the geological processes that contributed to the unique mineralogical, geochemical, and textural characteristics of these complexes are not well understood (Ashwal, 1993; Ashwal et al., 1994; Phinney et al., 1988; Hoffmann, 2012; Polat et al., 2012). The conventional viewpoint has been that Archean anorthosite complexes formed from the residual liquid of an anhydrous basaltic melt that remained after crystallization and accumulation of ultramafic minerals, such as olivine and pyroxene. This geodynamic setting is similar to that of the mid-ocean ridge basalts (Ashwal, 1993; Ashwal et al., 1994; Phinney et al., 1988). Other studies of Archean anorthosite complexes in various cratons, such as Greenland and India, have suggested, however, that the complexes were derived from hydrous sub-arc mantle sources (Windley et al. 1973; Polat et al., 2009, 2010, 2011, 2012; Rollinson, 2010; Rao et al., 2013; Hoffmann et al., 2012).

The reason for the debate is that all Archean anorthosite complexes underwent multiple phases of metamorphism and deformation, resulting in strong modification of their primary textures and mineralogical compositions. These modifications make it difficult to determine the parental magma compositions and tectonic setting of these complexes. Moreover, many typical Archean anorthosite complexes are understudied; only a few have been examined in detail using modern, high-precision, geochemical techniques (Berger et al., 2013; Mohan et al., 2013; Polat et al., 2009, 2010, 2012; Rao et al., 2013). Thus, their source characteristics, and petrogenetic and geodynamic origins are not well constrained.

Anorthosite complexes are best known and well exposed in the Archean granite-greenstone terranes of the Superior Province of Canada (Fig. 1). Some important features of several typical Archean anorthosite complexes in the Superior Province are listed in Table 1. All underwent various grades of metamorphism and degrees of deformation. Most complexes, however, preserve pristine igneous textures with large equant, euhedral to subhedral calcic plagioclase megacrysts (An＞80) being present in many layers (e.g., Ashwal, 1993; Ashwal et al., 1983;

Bédard et al., 2009; Leclerc et al., 2011).

Among these anorthosite complexes, the Neoarchean (ca. 2700 Ma) Bad Vermilion Lake Anorthosite Complex (BVLA Complex) is one of the least metamorphosed and least deformed examples of Archean anorthositic layered intrusions in the Superior Province (Table 1). Primary field relationships are well exposed in which the Complex intrudes mafic to felsic volcanic rocks of the Bad Vermilion Lake greenstone belt (Wood et al., 1980). The BVLA Complex has been variably metamorphosed to greenschist facies as reflected by the presence of hydrothermal alteration and greenschist metamorphic mineral assemblages (Ashwal et al., 1983). Shear zones, foliation and small-scale folds are not widespread in the BVLA Complex. Primary igneous textures are well preserved in many outcrops (Ashwal et al., 1983). Most plagioclase grains retain their primary equant shapes, and show elongation only in the shear zones (Phinney et al., 1988). Thus, the BVLA Complex provides an excellent opportunity to study the petrogenesis and tectonic setting of Archean anorthosite complexes in the Superior Province.

Despite its good preservation, there remain several outstanding problems in regards to the petrogenetic and geodynamic origin of the BVLA Complex: (1) The petrography and mineralogy of the BVLA Complex are understudied. For example, several significant lithological units (such as leucogabbros) of the Complex, as well as temporally and spatially associated granitic rocks, remain uninvestigated. (2) The existing whole-rock major and trace element data, which were obtained by X-ray Fluorescence and Instrumental Neutron Activation Analysis (Ashwal et al., 1983), are insufficient for describing the petrogenesis of the BVLA Complex. Data for several petrogenetically important elements (e.g., Ba, V, Nb, Zr, Y, Pr, Gd, Dy, Ho, Er, and Tm) are still required. (3) Previous studies (Ashwal, 1983; Ashwal et al., 1985) did not define the tectonic setting of the BVLA Complex. (4) The origin and evolution of the parental magmas to the BVLA Complex are not well understood. (5) The ages of the BVLA Complex and the bordering granitic rocks are poorly constrained (Ashwal et al., 1983, 1985).

In order to address these problems, we have conducted integrated field, petrographic, whole-rock major and trace element, whole-rock and mineral oxygen isotope studies of the BVLA Complex, and petrographic, whole-rock major and trace element and zircon U-Pb dating studies of the spatially associated granitic rocks. The objectives of this study of the BVLA Complex are: (1) to identify its primary versus secondary (metamorphic) textures and mineral assemblages; (2) to gain new insights into the petrogenesis of its anorthosites and associated rock types; (3) to constrain its age and that of the bordering granitic intrusions; (4) to determine the tectonic setting in which the BVLA Complex formed; and (5) to better constrain the nature of the crust (oceanic versus continental) into which it was emplaced.

2. Regional Geology

2.1. Western Superior Province

The Superior Province (Figs. 1 and 2) is the largest Archean craton in the world, composing 23% of the Earth's exposed Archean crust (Percival et al., 2012). It is exposed in the central part of the North American continent and together with other Archean cratons and Proterozoic orogens, makes up the Canadian Shield (Hoffman, 1988). It is composed of diverse types of igneous and sedimentary rocks metamorphosed at sub-greenschist to granulite facies and stabilized around 2.65 Ga ago (Percival et al., 1988, 2012).

Based on general structural and lithological characteristics, the Superior Province is divided into four regions: the Western Superior Province, the Central Superior Province, the Moyen-Nord Province, and the Northeastern Superior Province (Percival et al., 2012). The Western Superior region is composed of the area extending from Phanerozoic cover rocks in the west and north, to Lake Superior to the southeast.

On the basis of identified tectonic boundaries, the Western Superior Province is divided into eleven east-west-trending subprovinces (Fig. 2) (Card and Ciesielski, 1986; Williams et al., 1992; Stott, 1997; Card and Poulsen, 1998; Percival et al., 2012). These subprovinces consist mainly of alternating sedimentary and igneous terranes. The northernmost subprovince of the Western Superior Province is the North Caribou Superterrane, which is characterized by well-exposed crustal rocks having ca. 3.0 Ga depleted mantle model ages. This subprovince has been thought to be a relict fragment of Mesoarchean continental crust and the nucleus of the Superior Province (Thurston et al., 1991; Stott and Corfu, 1991). Later sedimentary and tectonic processes added the younger lithotectonic assemblages to this continental nucleus (Corfu and Stott, 1993, 1996; Sanborn-Barrie et al., 2001; Thurston, 2002; Percival et al., 2001, 2002). The English River subprovince to the south is composed predominantly of turbiditic greywackes that are interpreted to have been deposited in a syn-orogenic sedimentary basin (Percival et al., 2006). Deposition of the greywackes in the English River subprovince is attributed to the tectonic juxtaposition of the ca. 2.70 Ga Winnipeg River subprovince and an old (<3.4 Ga) relatively small continental fragment to the south (Westerman, 1978; Gower and Clifford, 1981; Davis et al., 1988; Davis and Smith, 1991; Beakhouse, 1991; Cruden et al., 1997, 1998). The Winnipeg River subprovince appears to extend eastward into the central Wabigoon subprovince (Fig. 2). The Wabigoon subprovince farther south contains numerous sequences of volcanic and sedimentary supracrustal rocks and granitoid plutons. The <2698 Ma metasedimentary rocks of the Quetico subprovince represent a flysch sequence deposited in response to a collision between the Wabigoon subprovince to the north and the Abitibi–Wawa composite terrane to the south (Davis et al., 1990).

2.2. The Western Wabigoon subprovince

The Wabigoon subprovince (Fig. 2) is a 900 km-long, 150 km-wide granite-greenstone subprovince in the western Superior Province (Blackburn et al., 1991). It is bounded by the metaplutonic Winnipeg River subprovince to the northwest, the metasedimentary to migmatitic English River subprovince to the northeast and the metasedimentary Quetico subprovince to the south. The Wabigoon subprovince is composed of ca. 3.0 to 2.71 Ga metamorphosed volcanic rocks and subordinate sedimentary rocks. These rocks were surrounded and intruded by circa 3.0 to 2.69 Ga gabbroic sills, granitoid batholiths and stocks.

The subprovince is divided into three distinct domains based on geographic distribution of lithological associations, including the western, central, and eastern Wabigoon regions (Blackburn et al., 1991). The western Wabigoon region is dominated by interconnected supracrustal belts and intruding large tonalite-granodiorite plutons (Blackburn et al., 1991). Volcanic rocks in the region are compositionally variable, ranging from ultramafic (komatiite), through mafic and intermediate, to felsic rocks. They are compositionally tholeiite and calc-alkaline suites and are interpreted to represent fragments of Archean oceanic crust and island arcs, respectively (Percival et al., 2012). The ages of the volcanic rocks range mainly between 2.745 to 2.720 Ga, with minor older (2.775 Ga) and younger (2.71-2.70 Ga) components (Corfu and Davis 1992). Sedimentary sequences in the western Wabigoon region are commonly younger than the volcanic counterparts and were deposited between ~2.711 and 2.698 Ga, as illustrated by local unconformable relationships and geochronological data (Davis, 1996; 1998; Fralick 1997; Fralick and Davis 1999). The central region is characterized by large volume of granitoid batholiths and small volume of supracrustal rocks (Blackburn et al., 1991). The eastern Wabigoon region consists mainly of Mesoarchean to Neoarchean supracrustal rocks and granitoid plutons (Percival et al., 2012).

2.3. The Bad Vermilion Lake area

The Bad Vermilion Lake area is underlain by low-grade metaigneous and metasedimentary rocks and forms part of the southwestern end of the Wabigoon subprovince in western Ontario (Fig. 3) (Mackasey et al., 1974). It is located at the boundary between the Wabigoon and Quetico subprovinces (Fig. 3). It is separated by the Quetico Fault from migmatitic rocks (Rainy Lake batholithic complex) to the north, and by the Seine River Fault to the south from higher-grade epiclastic metasedimentary rocks (Seine metasedimentary rocks) of the Quetico subprovince (Wood et al., 1980).

The ca. 2700 Ma BVLA Complex (Figs. 3 and 4) is exposed over an area of about 100 km^2

(Ashwal et al., 1983). It composed of anorthosite, leucogabbro and gabbro with minor mafic dykes and sills. The anorthosites in the BVLA Complex occur within a wedge of gabbros, mafic to felsic volcanic rocks, and granitic rocks (Figs. 3 and 4). The anorthosites are exposed along the shores of Bad Vermilion Lake, the southern shores of Seine Bay, and on the Seven Sisters Islands near the international border (Wood et al., 1980; Harris, 1974). They form a tadpole-shaped mass with an open "s"-fold configuration. The anorthosites are intruded by 50 centimeters to 15 meters wide, discontinuous mafic dykes, with a relict ophitic (microgabbroic) texture. Large, elongate gabbroic bodies are exposed along the northern and southern margins of the anorthositic layers. The northern gabbro contains discrete layers or lenses of massive Fe-Ti oxides with northeast strikes and vertical dips (Harris 1974; Wood et al., 1980). These Fe-Ti oxide masses are particularly abundant in the exposures north of Seine Bay (Ontario Department of Mines, 1961; Ashwal, 1983).

Boundaries between gabbro and anorthosite layers are sharp, whereas they are transitional between the leucogabbro and anorthosite layers (Fig. 5). The anorthosites are composed of coarse-grained (1-20 cm), equidimensional, euhedral to subhedral plagioclase, in a finer-grained mafic matrix (Fig. 5). The amount of mafic matrix in individual anorthosite and gabbro samples ranges from near zero to about 60% by volume (Ashwal et al., 1983). Distinct cumulate layers within the anorthositic unit are not well exposed, but many outcrops display changes in grain-size (Morrison et al., 1987). Layering within the gabbroic parts of the Complex is more obvious and common. The gabbros are fine-grained but locally they contain megacrystic plagioclase grains (Fig. 5).

The BVLA Complex has been metamorphosed to greenschist facies with most plagioclase having undergone partial to complete pseudomorphic replacement by aggregates of zoisite and other epidote minerals; many anorthosite outcrops, nonetheless, contain some relict primary plagioclase. Nearly all of the mafic silicates of the BVLA Complex have been altered to a mixture of fine-grained chlorite, actinolite and amphibole with only rare remnants of pyroxene. There is very little deformation in the Complex except in localized shear zones.

3. Analytical methods

3.1. Sampling

A total of 40 samples devoid of any surface alteration or weathering were collected from the BVLA Complex and associated intrusive granitic rocks. The sample suite provides a comprehensive spatial distribution of the anorthosite unit in the BVLA Complex, and covers all of its major rock types.

3.2. Petrographic investigation

The microscopic images were obtained at the Department of Earth and Environmental Sciences, University of Windsor, Windsor (Ontario) Canada, using an Olympus BX51 petrographic microscope. This microscope is equipped with a Luminera Infinity 1 high-resolution, digital/video camera coupled with capture software. It has both transmitted- and reflected-light capabilities. Some minerals that were difficult to identify using traditional microscopic methods were identified using an Environmental Scanning Electron Microscope

(EDAX FEI Quanta 200 FEG environmental SEM) at the Great Lakes Institute for Environmental Research (GLIER), University of Windsor. This SEM is equipped for Backscattered Electron (BSE) imaging and elemental analysis/mapping using Energy Dispersive X-ray Spectrometry (EDS) and cathodoluminescence. EDS analyses were performed under high-vacuum conditions, using a beam size of ~3.0 μm, an accelerating voltage of 20 kV, a counting time of at least 30 seconds and an approximate working distance of 12 millimeters.

3.3. Zircon separation and U-Pb analysis

About 8 kg of two representative samples (BVL2013-042, BVL2013-043) of granitic rocks intruding the BVLA Complex were crushed and milled. Standard heavy liquid and magnetic techniques were used to separate zircon concentrates, which were then purified by hand picking under a binocular microscope. The least metamict and least damaged grains were chosen for analyses. These grains were cast into epoxy resin discs and polished to expose the mid-sections of grains. Further assessment of grains and choice of sites for analyses was based on transmitted and reflected light, as well as cathodoluminescence (CL) and back-scattered electron (BSE) images.

Zircon U-Pb dating of the samples was carried out using LA-ICP-MS at the State Key Laboratory of Geological Processes and Mineral Resources, China University of Geosciences, Wuhan, People's Republic of China. Details of the operating conditions for the laser ablation system and the ICP-MS instrument and data reduction are the same as described in Liu et al. (2010). An Agilent 7500a ICP-MS instrument was used to acquire ion-signal intensities. A "wire" signal smoothing device is included in this laser ablation system, by which smooth signals are produced even at very low laser repetition rates down to 1 Hz (Hu et al., 2012). Helium was used as a carrier gas. Argon was used as the make-up gas and mixed with the carrier gas via a T-connector before entering the ICP. Nitrogen was added into the central gas flow (Ar+He) of the Ar plasma to decrease the detection limit and improve precision (Liu et al., 2010). Each analysis incorporated a background acquisition of approximately 20-30 seconds (gas blank) followed by 50 seconds data acquisition from the sample. The Agilent Chemstation was utilized for the acquisition of each individual analysis.

Grouped ages discussed in the text are reported with uncertainties of $\pm 1\sigma$. Data were plotted on Concordia diagrams using Isoplot/Ex (Ludwig, 2008).

3.4. Major and trace elements

Details of analytical methods for major and trace elements are given in Polat et al. (2009). All samples were powdered using an agate mill and were analyzed for major and some trace elements (e.g., Zr, V, Ba, Sr) at Actlabs, Ancaster (Ontario) Canada using a Thermo Jarrell-Ash ENVIRO II ICP and following the lithium metaborate/tetraborate fusion method. Samples were mixed with a flux of lithium tetraborate and lithium metaborate, and then fused at 1000°C in an induction furnace. The molten beads were rapidly dissolved in a solution of 5% HNO_3 containing an internal standard, and mixed continuously until digestion was complete (~30 minutes). Loss on ignition (LOI) was determined by measuring weight loss upon heating to 1100°C over a three-hour period. Totals of major elements were 100 ± 1 wt.%, with an analytical precision of 1–2% for most major elements.

Other trace element concentrations, including large ion lithophile elements (LILE; e.g., Rb), rare earth elements (REE; e.g., La-Lu) and, high field strength elements (HFSE: e.g., Zr, Nb, Ta), were determined using an inductively coupled plasma-mass spectrometer (ICP-MS Thermo X Series II) at GLIER, following the protocols of Jenner et al. (1990). Sample dissolution was conducted under clean laboratory conditions using doubly distilled acids. Approximately 100-120 mg of sample powder was used for acid digestion. Briefly, samples were dissolved in Teflon bombs in a concentrated mixture of HF-HNO_3 at ~120°C for 4 days and then further digested using 50% HNO_3 and H_3BO_4 (5000 ppm B) until no solid residue remained. International standards BHVO-1 and BIR-1 were used as reference materials. Anomalies of HFSE relative to neighboring REE are given as Nb/Nb*, Zr/Zr*, Hf/Hf* and Ti/Ti*. Mg-numbers (%) were calculated as the molar ratio of $Mg^{2+}/(Mg^{2+} + Fe^{2+})$, where Fe^{2+} is assumed to be 90% of the total Fe.

3.5. Oxygen isotope analyses

Five whole-rock samples, and ten fresh and five altered plagioclase separates were analyzed for oxygen isotope compositions. The sample selection was designed to determine the isotopic differences between least and most altered samples, and hence assess the effect of metamorphic alteration on plagioclase oxygen isotope composition. Mineral separation was performed at the University of Windsor. Crushed-samples were cleaned with distilled water, after which the fresh plagioclase and altered plagioclase grains were hand-picked using a reflected binocular microscope.

Oxygen-isotope analyses of mineral separates and whole-rock powders were performed at the Laboratory for Stable Isotope Science (LSIS), The University of Western Ontario, London (Ontario), Canada. Details of oxygen isotope analyses are given in Polat and Longstaffe (2014). For all samples, approximately 8 mg of sample powder were weighed into spring-loaded sample holders, evacuated overnight at ca. 150 °C, and then placed into nickel reaction vessels and heated *in vacuo* at 300 °C for further 3 hours to remove surface water. The samples were then reacted overnight at ca. 580 °C with ClF_3 to release silicate-bound oxygen (Borthwick and Harmon, 1982 following Clayton and Mayeda, 1963). The oxygen was converted to CO_2 over red-hot graphite, followed by isotopic measurement using a Prism II dual-inlet, stable-isotope-ratio mass- spectrometer.

The oxygen isotopic analyses are reported using δ-notation in parts per thousand (‰) relative to Vienna Standard Mean Ocean Water (VSMOW). Details of the calibration to VSMOW are given in Polat and Longstaffe (2014). The reproducibility of $\delta^{18}O$ values for samples was ±0.2 ‰. Accuracy was evaluated using internal laboratory quartz and CO_2 gas standards for which values of +11.5 ‰ and +10.27 ‰ were obtained, which compares well with their expected values of +11.5 ‰ and +10.30 ‰, respectively.

4. Results

4.1. Petrography

Thirty polished thin sections from all major lithological units were examined (Figs. 6 and

7). The anorthosite consists of plagioclase (85-90%), amphibole (0-5%), clinopyroxene (0-5%) and accessory minerals (3%) such as magnetite and titanite (Fig. 6). Although many anorthite crystals have been altered to albite and epidote, high-Ca, primary anorthite crystals have been preserved in many samples (Figs. 6 and 7). The interstitial mafic matrix consists mainly of chlorite, amphibole, albite, calcite, and quartz. Quartz and calcite contents occasionally exceed 5%, mainly adjacent to and within highly strained regions where quartz veining is common.

The leucogabbro and gabbro are mineralogically comparable to the anorthosite but contain higher proportions of amphibole, clinopyroxene and orthopyroxene. Coarse-grained layered gabbro and microgabbro (mafic dyke) have similar mineralogical compositions. They have undergone greenschist metamorphism and/or hydrothermal alteration (Figs. 6 and 7). The alteration is mainly characterized by epidote (clinozoisite) after plagioclase, and chlorite after amphibole, clinopyroxene and orthopyroxene. The gabbroic rocks display typical metamorphic textures characterized by a large percentage of rutile grains (10%) interlayered with titanite (10%) within the presumed cleavages of pyroxene (Fig. 7).

Granitic rocks generally have a heterogranular texture. They are medium- to coarse-grained, and contain ~25% plagioclase, ~55% quartz, ~10% biotite and ~5-10% K-feldspar with accessory magnetite, titanite, apatite and zircon (Fig. 8). In plane-polarized light, areas that are clear and white are mostly quartz and plagioclase (Fig. 8). Plagioclase grains are subhedral to euhedral and commonly twinned, but some plagioclase has been altered to fine-grained epidote (Fig. 8). Quartz occurs as aggregates of large grains, or as small grains either in plagioclase or along some grain boundaries (Fig. 8). Biotite occurs mainly as interstitial grains around larger crystals of plagioclase, K-feldspar and quartz (Fig. 8).

4.2. Zircon U-Pb dating

The selected CL images for zircons from samples BVL-2013-042 and BVL-2013-043 are presented in Figures 9 and 10. Zircon grains from granitic sample BVL2013-042 are colorless to light yellowish green. The grains range from long to short prismatic with lengths of 75-200 μm and length-width ratios of 1.5-3. Most grains are euhedral to subhedral with a few having well rounded edges or relict cores resulting from partial corrosion through dissolution and recrystallization. The CL images (Fig. 9) display broad oscillatory or striped zoning patterns typical of zircons from high-temperature magmatic intrusions (cf., Wu and Zheng, 2004). Twenty-eight U–Pb analyses on 28 grains from sample BVL2013-042 were performed (Table 2). All spots were situated on the oscillatory zones (Fig. 9) and have Th/U ratios of 0.47–1.00 (Table 2). The analyses yield a weighted mean $^{207}Pb/^{206}Pb$ age of 2649 ± 17 Ma (MSWD= 1.01) (Fig. 11; Table 2).

Zircon crystals from granitic sample BVL2013-043 are euhedral to subhedral, transparent and light yellow. They range in length from 100 to 200 μm with aspect ratios of 1.5:1–2.5:1. CL imaging reveals that these zircon crystals generally have oscillatory zoning (Fig. 10). Thirty-two spot analyses were obtained on rims of 32 zircon grains, and have Th/U ratios of 0.54–0.92 (Table 2). The analyses yield a weighed $^{207}Pb/^{206}Pb$ age of 2716 ± 18 Ma (MSWD = 0.58) (Fig. 11; Table 2).

4.3. Geochemistry

The geological data and key elemental ratios for the major rock types of the BVLA Complex and the associated granitic rocks are presented in Tables 3, 4 and 5. The salient major, trace and REE features of the rocks in the BVLA Complex and the granitic rocks are presented below.

4.3.1. Anorthosites and leucogabbros

The anorthosite and leucogabbro exhibit small to moderate variations in SiO_2 (43.0–49.7 wt.%), Al_2O_3 (17.2–28.8 wt.%) and CaO (8.8–17.4 wt.%) (Figs. 12 and 13; Table 3). In contrast, they are characterized by large variations in TiO_2 (0.14–0.92 wt.%), MgO (0.73–6.02 wt.%), Fe_2O_3 (2.57–10.42 wt.%), K_2O (0.02–1.20 wt.%), and Na_2O (0.19–3.30 wt.%) (Table 3). They also have large ranges of Zr (5–51 ppm), Ni (24–154 ppm), and Cr (9–518 ppm) contents (Fig. 14; Table 3). Mg-numbers range from 35 to 64 (Table 3). In addition, they display a large range of Al_2O_3/TiO_2 (17.7–193), Ti/Zr (67–1051), and Zr/Y (1.0–6.4) ratios (Table 3). Except for one outlier, the ratios of Y/Ho range from 20 to 38 in comparison to the primitive mantle values of 28 (Table 3) (Hofmann, 1988).

On chondrite-normalized REE and primitive-normalized trace element diagrams (Fig. 15), the anorthosite and leucogabbro samples have the following characteristics: (1) slightly enriched LREE patterns (La/Sm_{cn}=1.04–2.82; La/Yb_{cn}=1.28–5.48) and slightly enriched to flat HREE (Gd/Yb_{cn}=1.04–2.02) patterns with one outlier; (2) strong positive Eu anomalies (Eu/Eu*=

1.35-4.49); (3) minor to absent Ce anomalies (Ce/Ce*= 0.98-1.05); and (4) negative anomalies of Nb (Nb/Nb* = 0.08–0.88) and Ti (Ti/Ti* = 0.20–0.95 with a few exceptions).

4.3.2. Gabbro

The gabbro samples, with one outlier, are compositionally variable with 41–59 wt.% SiO_2, 11.3–22.6 wt.% Al_2O_3, 6.8–15.1 wt.% CaO, 7.5–16.4 wt.% Fe_2O_3, 0.02–3.63 wt.% Na_2O, 0.39–1.57 wt.% TiO_2, and 2.25–8.44 wt.% MgO (Figs. 12 and 13; Table 4). They display a large range of Al_2O_3/TiO_2 (9–34), Zr/Y (0.73–4.22) and Ti/Zr (114–1146) ratios. Mg- numbers span 37–60 (Table 4).

On basis of trace element patterns, the gabbro samples can be divided into two groups. Group 1 possesses zero to slightly negative Eu anomalies (Eu/Eu* = 0.73–1.06) and slightly positive Ti anomalies (Ti/Ti*= 0.96-1.31) (Fig. 15). Group 1 gabbro also shows moderate negative Nb anomalies with Nb/Nb* ratio ranging from 0.21 to 0.86. In addition, SiO_2 concentration ranges from 47.4 to 49.6 wt.%, Zr concentration (55-104 ppm) is relatively high, and Ti/Zr ratios range from 134 to 160. Group 2 gabbro has strongly enriched Eu with a Eu/Eu* ratio of 2.0-3.3 and strong positive Ti anomalies (1.75-2.55) (Fig. 15). Group 2 gabbro also shows slightly depleted to moderately enriched Nb with Nb/Nb* ranging from 0.93-3.08 (Fig. 15). SiO_2 contents are low (41.0-44.6 wt.%) and Zr contents are very low (5-8 ppm). Ti/Zr ratios range from 713-1146 (Table 4). Both groups display slightly depleted to slightly enriched LREE patterns (La/Sm_{cn}=0.68 - 1.47; Gd/Yb_{cn}=0.74 - 2.05) and slightly enriched HREE patterns with one outlier (La/Yb_{cn}=1.07 – 2.52). In addition, cerium anomalies (Ce/Ce* = 0.99–1.06) are minor to absent (Fig. 15; Table 4).

4.3.3. Granitic rocks

The granitic rocks are characterized by high SiO_2 (75.6-77.8 wt.%), relatively low Al_2O_3 (10.8 to 11.6 wt.%), low K_2O (0.26-2.13 wt.%), variable Na_2O/K_2O (Na_2O/K_2O=1.3-19.7) and low MgO (0.03-0.15 wt.%). They display metaluminous to peraluminous features with A/CNK ratios from 0.83-1.17 (Supplementary Fig. 1). They have very low Ni (8.33-14.26 ppm) contents. In addition, they show slightly enriched LREE patterns with La/Yb_{cn}=2.36 to 3.22 and negative Eu anomalies (Eu/Eu*=0.43-0.59) on the chondrite-normalized REE diagram (Fig. 16, Table 5). All samples have minor Ce anomalies (Ce/Ce*=1.0-1.07) and very low Sr/Y (0.40-1.25) ratios. The primitive mantle-normalized trace element patterns are characterized by elevated Th, and negative Nb (Ta) (Nb/Nb*=0.42 – 0.59), Sr (Sr/Sr*=0.05 – 0.14) and Ti (Ti/Ti*=0.04 – 0.07) anomalies (Fig. 16; Table 5).

4.4. Oxygen isotopes

Except for one outlier (BVL2013-077), the whole-rock oxygen isotope compositions ($\delta^{18}O$ = +5.5 to +6.7 ‰) of anorthosite samples from the BVLA Complex are similar to, or slightly higher than, the mantle (+5.5±0.5 ‰; Ito et al., 1987; Eiler, 2001) (Table 6). Sample BVL2013-077, by comparison, has a $\delta^{18}O$ value of +4.9 ‰. Without this sample, the average anorthosite whole-rock $\delta^{18}O$ value is +6.1±0.6 ‰ (all errors reported as SD), comparable to the

Fiskenæsset Complex (+6.3±0.3 ‰) (Polat and Longstaffe, 2014).

With only one exception (again BVL2013-077), BVLA Complex fresh plagioclase $\delta^{18}O$ values range from +5.8 to +7.2 ‰ (avg. +6.3±0.7 ‰), comparable to the Fiskenæsset Complex anorthosite (plagioclase avg. $\delta^{18}O$ = +6.4±0.5 ‰; Polat and Longstaffe, 2014). Partially altered plagioclase (to epidote) from BVLA Complex anorthosite has slightly lower $\delta^{18}O$ values (+5.3 to +6.0 ‰; avg. +5.8±0.3 ‰) (Table 6).

5. Discussion

5.1. The age of the Bad Vermilion Lake Anorthosite Complex

Most of the spots analyzed for U-Pb dating of the two granitic samples (BVL2013-042 and BVL2013-043) were located in the oscillatory zones of the zircon grains (Figs. 9 and 10). The Th/U ratios of these spots range from 0.47 to 1.00, consistent with a magmatic origin (cf., Wu and Zheng, 2004). Thus, the weighted mean $^{207}Pb/^{206}Pb$ ages of 2716 ± 18 Ma and 2649 ± 17 Ma for these samples are interpreted as the crystallization age of the granitic rocks that intruded the BVLA Complex. In outcrop, the granitic rocks display large variations in mineralogical composition, texture and structure, suggesting multiple phases of magma intrusion. Although continuous contacts between different intrusive phases are not well exposed, the measured dates are consistent with at least two phases of granitic rock emplacement in the study area. The older (2716 Ma) is therefore interpreted as the minimum formation age for the BVLA Complex.

Ashwal et al. (1985) reported whole-rock Rb-Sr (2.69±0.1 Ga) and Sm-Nd (2.74±0.07 Ga) regression ages for the BVLA Complex. The Rb-Sr date, however, is considered here to be unreliable given its large error and apparent younger value than the oldest date for the granitic rocks that intrude the Complex. The Sm-Nd isochron age of ca. 2.74 Ga for the BVLA Complex is more reliable and probably represents its intrusion age. The latter age also, within analytical error, corresponds well to previously reported dates of ~2.735-2.720 Ga for the regional syn-volcanic batholiths (tonalite-diorite-gabbro) (Corfu and Davis 1992; Whalen et al. 2004; Percival et al., 2006).

5.2. Alteration and element mobility

The rocks analyzed for this study have been metamorphosed at greenschist facies and/or undergone hydrothermal alteration. It is critical, therefore, to take account of the effects of post-magmatic alteration on the geochemistry of each lithological unit in the BVLA Complex before making petrogenetic and geodynamic interpretation based on the geochemical data.

Primary igneous textures are widely preserved in the BVLA Complex anorthosite, leucogabbro and gabbro (Fig. 6). At some locations, however, these rocks display extensive metamorphic recrystallization and calc-silicate (epidote, calcite) alteration (Fig. 6). The alteration criteria of Polat and Hofmann (2003) are adopted here to assess the effects of alteration on the original chemistry of the BVLA Complex. Except for three samples, all have loss-on-ignition (LOI) values < 6 wt.%, which suggests that secondary hydration or carbonation was been limited. Samples having a large LOI (> 6%) and displaying different trace element patterns from other samples are designated as severely altered and not considered further in the petrogenetic interpretation (Table 3 and 4). All remaining samples have minor to absent Ce anomalies

(Ce/Ce*= 0.98-1.06), indicating the absence of severe alteration (Table 3 and 4). Samples containing significant quantities of calcite and epidote (>5%) are designated as altered. Anorthosite samples with minor calcite and epidote alteration (<5%) have moderate positive Eu anomalies (Eu/Eu*=1.35-4.49), whereas those containing significant epidote and carbonate alteration have negative Eu (Eu/Eu* = 0.84-0.86) anomalies. The samples having negative Eu anomalies have been designated as altered and are not considered further in the petrogenetic interpretation (Table 3 and 4).

The anorthosite and Group 1 gabbro samples display a good correlation between TiO_2, Nb, Sm and Nd, on one hand, and Zr on the other hand, with few outliers (Fig. 14). Hence it is inferred that these element concentrations have not been significantly affected by metamorphic alteration. Similarly, REE, HFSE (Ti, Nb, Ta, Zr, Y) in most anorthosite samples, and both groups of gabbros display coherent patterns on primitive-mantle normalized diagrams (Fig. 15), indicating that these elements were also relatively immobile during post-magmatic alteration.

In addition, based on the following observations, we suggest that, except for one whole-rock sample (BVL2013-077), the whole-rock and fresh plagioclase oxygen isotope compositions of all samples analyzed remained near-pristine magmatic values despite metamorphism. (1) The $\delta^{18}O$ values of fresh plagioclase from the BVLA Complex anorthosite (+6.5±0.5‰) compare well with the compositions that typify plagioclase ($\delta^{18}O$ = ~ +6.4‰) of primary (juvenile) origin (cf., Eiler, 2001). (2) The range (SD) of $\delta^{18}O$ values for fresh plagioclase (±0.5 ‰, n=9) and whole-rock (±0.6 ‰, n=4) samples is quite small (Table 6). (3) The $\delta^{18}O$ values of fresh plagioclase (+6.5±0.5 ‰) are higher than that of altered plagioclase (+5.8±0.3 ‰) (Table 6). The whole-rock $\delta^{18}O$ values of the BVLA Complex anorthosite are slightly higher than average mantle-like composition (+5.5±0.5 ‰; Ito et al., 1987; Eiler, 2001). This composition is consistent with the classic Taylor and Epstein (1962a, 1962b) sequence of preferential partitioning of ^{18}O into Si- and Al-rich versus Mg- and Fe-rich phases during crystallization and high-temperature (re)equilibration. (4) There is no correlation between $\delta^{18}O$ values and the alteration-sensitive Ce anomalies (Fig. 17), consistent with limited mobility of oxygen in the BVLA Complex anorthosite, at least on the scale of sampling (see Polat and Longstaffe, 2014). (5) The oxygen isotope compositions of fresh and altered plagioclase are distinct.

The $\delta^{18}O$ value of anorthosite sample BVL2013-77 (+4.9 ‰) is lower than the rest of the samples. It displays relatively strong epidotization (Supplementary Fig. 2) and plots separately from other samples on many $\delta^{18}O$ versus major and trace element diagrams (Fig. 17). The fresh and altered plagioclase values for this sample are +4.8 ‰ and +5.8 ‰ respectively. We suggest that the primary $\delta^{18}O$ value of this sample was modified by high-temperature alteration (cf., Bosch et al., 2004; Craig et al., 2011) that reset its value to +4.8 ‰ followed by hydrothermal alteration that caused the altered plagioclase to become enriched in ^{18}O. Hence this sample is excluded from further discussion.

Collectively, the whole-rock and plagioclase $\delta^{18}O$ values of ‘fresh’ samples of the BVLA Complex anorthosite are consistent with a near-pristine magmatic signatures rather than an extensive metamorphic overprinting over a range of temperatures. The latter process likely would have produced larger variations in oxygen isotope composition (cf., Valley, 1986; Peck and Valley, 1996; Polat and Longstaffe, 2014).

5.3. Crustal contamination and depth of partial melting

The anorthosite and Group 1 gabbro of the BVLA Complex display strong negative Nb anomalies relative to REE and LILE (Fig. 15; Tables 3 and 4). Such anomalies can be related to primary mantle source characteristics or may reflect crustal contamination (Pearce and Peate, 1995; Polat et al., 2009). There is no field evidence indicating that the BVLA Complex was emplaced into older continental crust (Ashwal et al., 1983). Large positive initial εNd (+2.0 ± 1.4) values (Ashwal et al., 1985) for the BVLA Complex are inconsistent with its contamination by significantly older continental rocks. In addition, there are no correlations between SiO_2 abundances and contamination-sensitive elements and ratios (e.g., Th, Zr, La, Ni, La/Sm_{cn}, Nb/Nb*, Zr/Zr*). Moreover, the near-mantle whole-rock and fresh plagioclase $\delta^{18}O$ values (+6.1±0.6 ‰ and +6.5±0.5 ‰, respectively) of the ca. 2.7 Ga BVLA Complex anorthosite are inconsistent with substantial continental crust contamination, thus suggesting a setting away from continental sources. In addition, anorthosite, leucogabbro and gabbro of the BVLA Complex share near flat to slightly enriched HREE patterns (Fig. 15). This feature is consistent with a shallow depth of partial melting of a mantle source that did not contain garnet.

5.4. Role of fractional crystallization on cumulate processes and the emplacement of the BVLA Complex

Accepting that alteration and crustal contamination has had only a very small effect on the geochemistry of the BVLA Complex, these data can be used to constrain the role of fractional crystallization on its petrogenesis. Geochemical trends on MgO versus Al_2O_3, CaO, Fe_2O_3(T), Ni and Co plots (Fig. 13) for anorthosite, leucogabbro and gabbro samples reflect fractionation of olivine, pyroxene and plagioclase, as also observed in the Fiskenæsset Complex (Polat et al., 2009). In addition, low abundances of MgO, Ni, Cr, Co, and Sc in the anorthosite and leucogabbro (Table 3) are consistent with the removal of olivine, clinopyroxene and/or orthopyroxene prior to plagioclase accumulation (see Polat et al., 2009, 2010). These geochemical characteristics indicate that the anorthosite, leucogabbro and gabbro were derived from fractionated magmas.

Ashwal et al. (1983) suggested that the BVLA Complex was a cumulate mass from a subvolcanic intrusive chamber. Similar petrogenetic processes have been proposed to explain the origin of the Fiskenæsset and Naajat Kuuat complexes in Greenland and the Sittampundi Complex in southern India (Polat et al., 2009; Hoffmann et al., 2012; Mohan et al., 2013; Huang et al., 2014). These studies suggest that the layering in Archean anorthosite complexes indicate compositionally stratified magma chamber(s), with thick layers of late-stage crystallization of plagioclase on top and early-stage olivine-rich dunite layers at the bottom (Polat et al., 2009; Hoffmann et al., 2012; Mohan et al., 2013; Huang et al., 2014). Late accumulation of calcic plagioclase is consistent with differentiation of hydrous parental melts, and such a scenario is commonly reported for arc-related geodynamic settings (Windley, 1995).

Ultramafic layers do not crop out in the BVLA Complex. They may lie beneath its exposed level, but they may also have been removed tectonically or magmatically. For the Fiskenæsset Complex, Polat et al. (2011) suggested that there was originally a 500-m thick ultramafic unit (dunite, peridotite, pyroxenite, and hornblendite) at its bottom, of which $<$ 50 m now remains.

This suggests that more than 90% of the ultramafic rocks of the Fiskenæsset were either delaminated or recycled into the mantle as a residual cumulate, or were destroyed during thrusting and intrusion of granitoid rocks. Such processes may have also affected the BVLA Complex.

5.5. New geochemical constraints on the geodynamic setting

All samples of the BVLA Complex anorthosite, leucogabbro, and Group 1 gabbro are characterized by depletion of Nb relative to Th and La. Considering that crustal contamination of the BVLA Complex was likely minimal, the negative Nb anomalies (Fig. 15) may represent mantle source characteristics. These anomalies are consistent with a subduction zone (forearc-arc-backarc) signature (Pearce and Peate, 1995; Pearce, 2008; Polat et al., 2009).

For some elements, Group 2 gabbro is geochemically distinctive from Group 1 gabbro. Group 2 gabbro is characterized by relatively low concentrations of SiO_2 (Fig. 12) and Zr (Fig. 14), and display flat to positive Nb anomalies and strongly elevated Eu anomalies and Ti anomalies (Fig. 15). Compared to silicates, Nb partitions strongly into titanite and rutile, and moderately into ilmenite and Ti-magnetite (Green and Pearson 1987; Moore et al., 1992). Thus, positive Ti and Nb anomalies are likely to reflect the presence of Ti-bearing oxide minerals, which is consistent with the petrographic observations (15-20% titanite, rutile and/or ilmenite) (Fig. 7). These minerals likely formed during metamorphic recrystallization of pyroxene grains; they occur as small grains either in former cleavages of pyroxene grains or along some grain boundaries (Fig. 7).

Positive Eu anomalies indicate that plagioclase crystallization was limited before the formation of Group 2 gabbro (Fig. 15). However, except for the Eu anomalies, anorthosite, and Group 1 and Group 2 gabbro have very similar REE patterns with near flat to slightly enriched LREE patterns (Fig. 15). These similarities suggest that these rocks are cogenetic.

On the Nb/Nb* versus La/Sm_{cn} and Th/Nb versus La/Nb diagrams (Fig. 18), both Group 1 and Group 2 gabbro plot predominantly within the field of gabbro from Cenozoic oceanic arc settings (e.g., Aleutian Arc, Mariana Arc, Scotia Arc and Tonga Arc). In addition, they are very similar in composition to gabbro from the Semail Ophiolite in Oman (Fig. 18), which is a typical suprasubduction-zone type ophiolite (Lippard et al., 1986; Hacker et al., 1996; Dilek and Furnes 2009; Alabaster et al., 1982). Moreover, on $\delta^{18}O$ versus major and trace element diagrams (Fig. 17), anorthosite from the BVLA Complex shares similar characteristics with anorthosite from the Fiskenæsset Complex, which is interpreted to have formed in an intra-oceanic arc setting (Polat et al., 2009, 2010). Therefore, based on the sum of evidence, we suggest that the BVLA Complex likely formed in an oceanic arc.

The interpretation of the BVLA Complex as the product of low-pressure partial melting at a supra-subduction zone is consistent with the experimental study of Takagi et al. (2005). They showed that at constant composition, in a low-alkali, high-alumina, arc tholeiite (17 wt.% Al_2O_3), there is a linear relationship between plagioclase An content and water content of the melt. High-An plagioclase is the liquidus phase in such melts containing up to 5% H_2O at low pressure. The highly calcic plagioclase reported by Takagi et al. (2005) (An_{90}) is comparable with the peak anorthite (An) content reported for BVLA anorthosite (An_{81}) (Ashwal et al., 1983).

5.6. Petrogenesis of intrusive granitic rocks associated with the BVLA Complex

The granitic rocks display near flat to slightly fractionated REE patterns with low La/Yb_{cn} (2.4-3.2) and high Yb_{cn} (65.3-95.3) (Fig. 16). These geochemical characteristics suggest that the granitic rocks formed by partial melting of a mafic source at shallow depths, probably the lower crust, without garnet residue in the source. The presence of negative Eu and Sr anomalies in the granitic rocks (Fig. 16) reflects a plagioclase residue in the source, and thus melting at pressures lower than the plagioclase stability field (＜32 kb, Lindsley, 1968). The low Sr (59-128 ppm) and high Y (95-168 ppm) abundances and correspondingly low Sr/Y (0.40 – 1.25) are consistent with retention of plagioclase in the source (Table 5). Additionally, all samples exhibit strong depletion of Nb, Ta and Ti on the primitive mantle-normalized diagram (Fig. 16), which may be attributed to rutile in the residue or melting of mafic crust in a thickened arc (Martin et al., 2005; Nagel et al., 2012).

The Bad Vermilion Lake granitic rocks possess high SiO_2 (~77 wt.%), $Fe_2O_3(T)/MgO$ ratios (28 to 55) and HFSE (>100 times chondrite), and low CaO, Sr, Ba and Eu contents (Table 5). These features are similar to those of A-type granites (Whalen et al., 1987). On plots of Zr versus 10,000×Ga/Al and Nb versus 10,000×Ga/Al (Whalen et al., 1987), the Bad Vermilion Lake granitic rocks plot within the field of A-type granites (Supplementary Fig. 3).

A-type granites are generally considered to form in extensional settings (Bonin, 2007; Dostal et al., 2015 and references therein). They can be further divided into A_1 and A_2 chemical subgroups (Eby, 1992). A_1-type granites have certain geochemical characteristics similar to those observed for oceanic-island basalts (OIB) and thus their sources are considered to be from within intraplate settings (Eby, 1992). In contrast, A_2-type granites are similar to rocks from continental crusts or island arcs developed at convergent plate margins (Eby, 1992). It has been suggested that the arc geochemical signature of A_2-type granites is related to fluids released during subduction (Li et al., 2012).

The Neoarchean Bad Vermilion Lake granitic rocks reported in this study plot in the field of A_2 subgroup and overlap with IAB field, consistent with an arc setting (Supplementary Fig. 4). Thus, we suggest that the Bad Vermilion Lake granitic rocks formed in a post-collisional extensional setting following emplacement of the BVLA Complex in a magmatic arc (Fig. 19).

5.7. Geochemistry of Archean rocks and plate tectonics

A detailed discussion of Archean igneous petrogenesis and tectonics is beyond the scope and objectives of this study. Interested readers are referred to Polat et al. (2015) for a comparison between mobilist, uniformitarian (i.e., Phanerozoic-like plate tectonics) and fixist, non-uniformitarian (i.e., gravity-driven sinking, sagduction, dripping, delamination, diapiric rising, crustal overturn, and heat pipe processes) models proposed for the Archean Earth. The non-uniformitarian models cannot explain the occurrence of similar field relationships (e.g., cross-cutting relationships, unconformities, tectonically juxtaposed crustal blocks), lithological associations (e.g., ophiolites, volcanic suites, mélanges, granitoid rocks), and structural (e.g., asymmetric folds, strike-slip, normal and reverse faults) and geochemical (e.g., HFSE, REE, LILE, transition metal systematics) characteristics in both the Archean and Phanerozoic rock records (see de Wit, 1998; Furnes et al., 2007, 2013, 2015; Burke, 2011; Kisters et al., 2012;

Percival et al., 2012; Kusky et al., 2013; Santosh et al., 2013; Backeberg et al., 2014; Nutman et al., 2015). The non-uniformitarian models have no Archean field analogs.

Lithological, structural, sedimentological and metamorphic characteristics of various rock associations are controlled mainly by tectonics, reflecting the physical and chemical processes associated with different tectonic settings (e.g., mid-ocean ridge, arc, forearc, continental rift). The Archean and Phanerozoic geological records have similar igneous (e.g., basalt, andesite, dacite, rhyolite, granite, granodiorite, diorite, gabbro, dunite, peridotite, and so on), metamorphic (e.g., greenschist, amphibolite, granulite) and sedimentary (conglomerate, sandstone, shale, carbonate, chert) rock types, and structures, indicating that geological processes operated in both eons are broadly similar.

The trace element compositions of igneous rocks occurring in different tectonic settings are distinct in terms their REE, LILE, and HFSE systematics (Sun and McDonough, 1989; Hofmann, 1997; Polat and Kerrich, 2006; Pearce, 2008), differences that stem from the physical and chemical processes involved in the genesis of these rocks in a particular tectonic environment. Because certain groups of elements (e.g., HFSE, REE, LREE, transition metals) behave consistently in petrogenesis, including processes affecting source composition, residual mineralogy, partial melting, magma differentiation, metasomatism and hybridization, these elements are expected to have had similar behavior throughout Earth's history (Polat and Kerrich, 2006).

Although the Archean Eon had higher mantle temperatures than its Phanerozoic counterpart (see Herzberg et al., 2010 and references therein), Archean volcanic rocks share the trace element characteristics of Phanerozoic equivalents (see Szilas et al., 2012, 2013a, 2013b; Polat, 2013), suggesting that uniformitarian geochemical behavior also prevailed in the Archean despite counter arguments (e.g., Bédard, 2006). Accordingly, we suggest that the geochemical characteristics of the BVLA Complex and the spatially associated granitic rocks represent regional-scale tectonic processes operated at a Neoarchean convergent margin in the southwestern Superior Province. Given the presence of polyphase deformation and metamorphism in Archean terranes, however, we continue to caution that the trace element systematics of Archean rocks should be used in conjunction with field characteristics to constrain their geodynamic setting.

8. Conclusions

On the basis of new field, petrographic, U-Pb zircon age, whole-rock major and trace element, and whole-rock and plagioclase mineral oxygen isotope data, we reach the following conclusions concerning the origin of the Neoarchean BVLA Complex and the spatially associated granitic rocks:

1. Zircon U-Pb ages from the intruding granitic rocks suggest a minimum age of 2716±18 Ma for the BVLA Complex. Zircon ages indicate that the granitic rocks were emplaced as multiple batches of magma between 2716 and 2649 Ma.
2. Although the BVLA Complex underwent greenschist-facies metamorphism, its original geochemical composition was not affected significantly. The geochemical and oxygen isotopic data do not indicate substantial crustal contamination of the BVLA Complex.

3. The parental magmas of the anorthosite, leucogabbro and gabbro in the BVLA Complex originated from partial melting of a shallow mantle source. Trends of Zr and MgO versus immobile major and trace elements indicate that the concentrations of most elements were controlled by fractional crystallization involving the removal and accumulation of olivine, orthopyroxene, clinopyroxene, amphibole and plagioclase.
4. The trace element systematics of the anorthosite, leucogabbro, and gabbro of the BVLA Complex and the oxygen isotope systems of its anorthosite are consistent with an intra-oceanic subduction zone geodynamic setting. On the basis of these geochemical characteristics, the BVLA Complex is interpreted as a remnant of a Neoarchean oceanic island arc.
5. Geochemical data indicate that the granitic rocks intruded into the BVLA Complex are A_2-type. We suggest that they formed in a post-collisional, extensional setting following formation of the BVLA Complex in the arc.

Acknowledgements

This research was supported by NSERC grants to A. Polat and F.J. Longstaffe, and made possible, in part, through release time provided by the Canada Research Chairs Program. Constructive comments by one anonymous reviewer and M.R. Mohan resulted in significant improvements to the paper. We acknowledge and thank J.C. Barrette for assistance with the trace element analyses, S. Lackie for assistance with the SEM analyses, and N. Naderi for assistance with the oxygen isotopic analyses. We thank Dr. Y. Eyuboglu and Dr. M. Santosh for the invitation to join this special issue. This is Laboratory for Stable Isotope Science (LSIS)

Contribution #330.

References

Alabaster, T., Pearce, J.A., Malpas, J., 1982. The volcanic stratigraphy and petrogenesis of the Oman ophiolite complex. Contributions to Mineralogy and Petrology 81, 168-183.

Allard, G.O., 1970. The Dore Lake complex, Chibougamau, Quebec-a metamorphosed Bushveld-type layered intrusion. In Symposium on the Bushveld igneous complex and other layered intrusions, Editors: JL Visser and G. Von Gruenewaldt. Geological Society of South Africa, pp. 477-491.

Ashwal, L.D., Wooden, J.L., Phinney, W.C., Morrison, D.A., 1985. Sm−Nd and Rb−Sr isotope systematics of an Archean anorthosite and related rocks from the Superior Province of the Canadian Shield. Earth and Planetary Science Letters 74, 338-346.

Ashwal, L.D., Jacobsen, S.B., Myers, J.S., Kalsbeek, F., Goldstein, S.J., 1989. Sm-Nd Age of the Fiskenæsset Anorthosite Complex, West Greenland. Earth and Planetary Science Letter 91, 261-270.

Ashwal, L.D., 1993. Anorthosites. Minerals and Rocks Series 21. Springer-Verlag, Berlin, 422 pp.

Ashwal, L.D., Myers, J.S., 1994. Archean anorthosites. Archean Crustal Evolution. Elsevier, Amsterdam, 315-355.

Ashwal, L.D., Phinney, W.C., Morrison, D.A., Wooden, J.L., 1982. Underplating of Archean continents: evidence from the Bad Vermillion Lake Anorthosite Complex, Ontario. In Lunar and Planetary Science Conference 13, 20-21.

Ashwal, L.D., 1981. The Bad Vermilion Lake Anorthosite Complex, Ontario: Sr and Nd isotopic evidence for depleted Archean mantle. Abstract with Program, Geological Society of America 13, 399.

Ashwal, L.D., 2004. Origin of anorthosites: petrological and tectonic considerations. Transactions of American Geophysical Union (Eos) 85, 514.

Ashwal, L.D., Morrison, D.A., Phinney, W.C., Wood, J., 1983. Origin of Archean anorthosites: evidence from the Bad Vermilion Lake Anorthosite Complex, Ontario. Contributions to Mineralogy and Petrology 82, 259-273.

Ashwal, L.D., 2010. The temporality of anorthosites. The Canadian Mineralogist 48, 711-728.

Backeberg, N.R., Rowe, C.D., van Hinsberg, V.J., Bellefroid, E.J., 2014. Structural and metamorphic evidence for Mesoarchaean subduction in the Finlayson Lake greenstone belt, Superior Province, Ontario. Precambrian Research 249, 100–114.

Beakhouse, G.P., 1991. Winnipeg River subprovince. In: Thurston, P.C., Williams, H.R., Sutcliffe, R.H., Stott, G.M. (Eds.), Geology of Ontario. Ontario Geological Survey Special Volume 4, Pt. 1, pp. 279–301.

Bédard, J.H., 2006. A catalytic delamination-driven model for coupled genesis of Archaean crust and sub-continental lithospheric mantle. Geochimica et Cosmochimica Acta 70, 1188–1214.

Bédard, J.H., Leclerc, F., Harris, L.B., Goulet, N., 2009. Intra-sill magmatic evolution in the Cumming Complex, Abitibi greenstone belt: Tholeiitic to calc-alkaline magmatism recorded in an Archean subvolcanic conduit system. Lithos 111, 47-71.

Berger, J., Diot, H., Lo, K., Ohnenstetter, D., Femenias, O., Pivin, M., Demaiffe, D., Bernard, A., Charlier, B., 2013. Petrogenesis of Archean PGM-bearing chromitites and associated ultramafic-mafic-anorthositic rocks from the Guelbel Azib layered complex (West African craton, Mauritania). Precambrian Research 224, 612-628.

Bhaskar Rao, Y.J., Chetty, T.R.K., Janardhan, A.S., Gopalan, K., 1996. Sm–Nd and Rb–Sr ages and P–T history of the Archean Sittampundi and Bhavani layered meta-anorthosite complexes in the Cauvery shear zone, South India: evidence for Neoproterozoic reworking of Archean crust. Contributions to Mineralogy and Petrology 125, 237-250.

Blackburn, C.E., John, G.W., Ayer, J., Davis, D.W., 1991. Wabigoon Subprovince. In: Thurston, P.C., Williams, H.R., Sutcliffe, R.H., Stott, G.M. (Eds.), Geology of Ontario. Ontario Geological Survey Special Volume 4, Pt. 1, pp. 303–381.

Bosch, D., Jamais, M., Boudier, F., Nicolas, A., Dautria, J.M., Agrinier, P., 2004. Deep and high-temperature hydrothermal circulation in the Oman ophiolite—petrological and isotopic evidence. Journal of Petrology 45(6), 1181-1208.

Bonin, B., 2007. A-type granites and related rocks: evolution of a concept, problems and prospects. Lithos 97, 1 – 29.

Borthwick, J., Harmon, R.S., 1982. A note regarding ClF3 as an alternative to BrF5 for oxygen isotope analysis. Geochimica et Cosmochimica Acta 46, 1665–1668.

Burke, K., 2011. Plate tectonics, the Wilson cycle, and mantle plumes: geodynamics from the top. Annual Review of Earth and Planetary Sciences 39, 1–29.

Card, K.D., Ciesielski, A., 1986. Subdivisions of the Superior Province of the Canadian Shield.

Geoscience Canada 13, 5–13.

Card, K.D., Poulsen, K.H., 1998. Geology and mineral deposits of the Superior Province of the Canadian shield. Chapter 2 in Geology of the Precambrian Superior and Grenville Provinces and Precambrian Fossils in North America. In: Lucas, S. (Coord.), Geological Survey of Canada Geology of Canada 7, pp. 13−194.

Clayton, R.N., Mayeda, T.K., 1963. The use of bromine pentafluoride in the extraction of oxygen from oxides and silicates for isotopic analysis. Geochimica et Cosmochimica Acta 27, 43–52.

Corfu, F., Davis, D.W., 1992. A U-Pb geochronological framework for the western Superior Province, Ontario. In: Thurston, P.C., Williams, H.R., Sutcliffe, R.H., Stott, G.M. (Eds.), Geology of Ontario. Ontario Geological Survey Special Volume 4, Pt. 2, pp. 1335–1346.

Corfu, F., Stott, G.M., 1993. Age and petrogenesis of two late Archean magmatic suites, northwestern Superior Province, Canada: zircon U–Pb and Lu–Hf isotopic relations. Journal of Petrology 34, 817–838.

Corfu, F., Stott, G.M., Breaks, F.W., 1995. U–Pb geochronology and evolution of the English River subprovince, an Archean low P–high T metasedimentary belt in the Superior Province. Tectonics 14, 1220–1233.

Corkery, M.T., Davis, D.W., Lenton, P.G., 1992. Geochronological constraints on the development of the Cross Lake greenstone belt, northwest Superior Province, Manitoba. Canadian Journal of Earth Sciences, 29(10), 2171-2185.

Cruden, A.R., Davis, D.W., Menard, T., Robin, P.Y.R., 1997. Structural and geochronological relationships between the Winnipeg River and Wabigoon Subprovinces: implications for the terrane accretion model. In: Harrap, R.M., Helmstaedt, H. (Eds.), Western Superior Transect Second Annual Workshop. Lithoprobe Report 63, pp. 18–26.

Cruden, A.R., Davis, D.W., Melnyk, M., Robin, P.Y.R., Menard, T., 1998. Structural and geochronological observations at Kenora: implications for the style and timing of deformation during the Kenoran orogeny, northwestern Ontario. In: Harrap, R.M., Helmstaedt, H. (Eds.), Western Superior Transect Second Annual Workshop. Lithoprobe Report 65, pp. 54–62.

Davis, D.W., Sutcliffe, R.H., Trowell, N.F., 1988. Geochronological constraints on the tectonic evolution of a late Archean greenstone belt, Wabigoon subprovince, northwest Ontario. Precambrian Research 39, 171–191.

Davis, D.W., Pezzuto, F., Ojakangas, R.W., 1990. The age and provenance of metasedimentary rocks in the Quetico subprovince, Ontario, from single zircon analyses: implications for Archean sedimentation and tectonics in the Superior Province. Earth and Planetary Science Letters 99, 195–205.

Davis, D.W., Smith, P.M., 1991. Archean gold mineralization in the Wabigoon subprovince, a product of crustal accretion: evidence from U–Pb geochronology in the Lake of the Woods area, Superior Province, Canada. Journal of Geology 99, 337–353.

Davis, D.W., 1996. Provenance and depositional age constraints on sedimentation in the western Superior transect area from U-Pb ages of zircons. In: Harrap, R.M., Helmstaedt, H. (Eds.), Western Superior Transect Second Annual Workshop. Lithoprobe Report 53, pp. 18–23.

Davis, D.W., 1998. Speculations on the formation and crustal structure of the Superior province from U-Pb geochronology. In: Harrap, R.M., Helmstaedt, H. (Eds.), Western Superior Transect Second Annual Workshop. Lithoprobe Report 65, pp. 21–28.

de Wit, M.J., 1998. On Archean granites, greenstones, cratons, and tectonics: does the evidence demand a verdict? Precambrian Research 91, 181–226.

Dilek, Y., Furnes, H., 2009. Structure and geochemistry of Tethyan ophiolites and their petrogenesis in subduction rollback systems. Lithos 113, 1-20.

Dilek, Y., Furnes, H., 2014. Ophiolites and their origins. Elements 10, 93-100.

Dostal, J., Owen, V., Shellnutt, G., Keppie, D., Gerel, O., Corney, R., 2015. Petrogenesis of the Triassic Bayan-Ulan alkaline granitic pluton in the North Gobi rift of central Mongolia: Implications for the evolution of Early Mesozoic granitoid magmatism in the Central Asian Orogenic Belt. Journal of Asian Earth Sciences 109, 50-62.

Eby, G.N., 1992. Chemical subdivision of the A-type granitoids: petrogenetic and tectonic implications. Geology 20, 641-644.

Eiler, J.M., 2001. Oxygen isotope variations in basaltic lavas and upper mantle rocks. In: Valley, J.W., Cole, D.R. (Eds.), Stable Isotope Geochemistry. In: Reviews in Mineralogy and Geochemistry, vol. 43. Mineralogical Society of America, Washington, pp. 319–364.

Fralick, P., 1997. Neoarchean evolution of the Wabigoon Subprovince: evidence from the sedimentary record. In: Harrap, R.M., Helmstaedt, H. (Eds.), 1999 Western Superior Transect Fifth Annual Workshop. Lithoprobe Report 63, Lithoprobe Secretariat, University of British Columbia, pp. 97–99.

Fralick, P., Davis, D.W., 1999. The Seine-Couchiching problem revisited: sedimentology, geochronology and geochemistry of sedimentary units in the Rainy Lake and Sioux Lookout areas. In: Harrap, R.M., Helmstaedt, H.H. (Eds.), 1999 Western Superior Transect Fifth Annual Workshop. Lithoprobe Report 70, Lithoprobe Secretariat, University of British Columbia, pp. 66–75.

Furnes, H., de Wit, M., Staudigel, H., Rosing, M., Muehlenbachs, K., 2007. A vestige of Earth's oldest ophiolite. Science 315, 1704–1707.

Furnes, H., de Wit, M.J., Robins, B., 2013. A review of new interpretations of the tectonostratigraphy, geochemistry and evolution of the Onverwacht Suite, Barberton Greenstone Belt, South Africa. Gondwana Research 23, 403–428.

Furnes, H., Dilek, Y., de Wit, M., 2015. Precambrian greenstone sequences represent different ophiolite types. Gondwana Research 27, 649–685.

Gower, C.F., Clifford, P.M., 1981. The structural geometry and geological history of Archean rocks at Kenora, northwestern Ontario; a proposed type area for the Kenoran Orogeny. Canadian Journal of Earth Science 18, 1075–1091.

Green, T.H., Pearson, N.J., 1987. An experimental study of Nb and Ta partitioning between Ti-rich minerals and silicate liquids at high pressure and temperature. Geochimica et Cosmochimica Acta 51, 55-62.

Grimes, C.B., Ushikubo, T., John, B.E., Valley, J.W., 2011. Uniformly mantle-like $\delta^{18}O$ in zircons from oceanic plagiogranites and gabbros. Contributions to Mineralogy and Petrology 161, 13-33.

Hacker, B.R., Mosenfelder, J.L., Gnos, E., 1996. Rapid emplacement of the Oman ophiolite, thermal and geochronological constraints. Tectonics 15, 1230-1247.

Halama, R., Waight, T., Markl, G., 2002. Geochemical and isotopic zoning patterns of plagioclase megacrysts in gabbroic dykes from the Gardar Province, South Greenland: implications for crystallisation processes in anorthositic magmas. Contributions to Mineralogy and Petrology 144, 109–127.

Hart, S.R., Davis, G.L., 1969. Zircon U-Pb and whole-rock Rb-Sr ages and early crustal development near Rainy Lake, Ontario. Geological Society of America Bulletin 80, 595–616.

Henry, P., Stevenson, R., Gariepy, C., 1998. Late Archean mantle composition and crustal growth in the western Superior Province of Canada: Neodymium and lead isotopic evidence from the Wawa, Quetico, and Wabigoon subprovinces. Geochimica et Cosmochimica Acta 62, 143–157.

Henry, P., Stevenson, R., Laribi, Y., Gariepy, C., 2000. Nd isotopic evidence for Early to Late Archean (3.4–2.7 Ga) crustal growth in the Western Superior Province (Ontario, Canada). Tectonophysics 322, 135–151.

Herzberg, C., Condie, K., Korenaga, J., 2010. Thermal history of the Earth and its petrological expression. Earth and Planetary Science Letters 292, 79–88.

Hofmann, A.W., 1997. Mantle geochemistry: the message from oceanic volcanism. Nature 385, 219-229.

Hofmann, A.W., 1988. Chemical differentiation of the Earth: the relationship between mantle, continental crust, and oceanic crust. Earth and Planetary Science Letters 90, 297-314.

Hoffmann, J.E., Svahnberg, H., Piazalo, S., Schersten, A., Munker, C., 2012. The geodynamic evolution of Mesoarchean anorthosite complexes inferred from the Naajat Kuuat Complex, Southern West Greenland. Precambrian Research 196-197, 149-170.

Hu, Z., Liu, Y., Gao, S., Liu, W., Zhang, W., Tong, X., Yang, L., 2012. Improved in situ Hf isotope ratio analysis of zircon using newly designed X skimmer cone and jet sample cone in combination with the addition of nitrogen by laser ablation multiple collector ICP-MS. Journal of Analytical Atomic Spectrometry 27, 1391-1399.

Hubregtse, J. J. M. W., 1980. The Archean Pilcwitonei granulite domain and its position at the margin of the northwestern Superior Province (Manitoba). Manitoba Dept. of Energy and Mines, Geological Survey, Geology Paper GP8O-3, 16 pp.

Ito, E., White, W.M., Goepel, C., 1987. The O, Sr, Nd and Pb isotope geochemistry of MORB. Chemical Geology 62, 157-176.

Jenner, G.A., Longerich, H.P., Jackson, S.E., Fryer, B.J., 1990. ICP-MS; a powerful tool for high-precision trace-element analysis in earth sciences; evidence from analysis of selected U. S. G. S. Reference samples. Chemical Geology 83, 133-148.

Kisters, A.F.M., van Hinsberg, V.J., Szilas, K., 2012. Geology of an Archaean accretionary complex — the structural record of burial and return flow in the Tartoq Group of South West Greenland. Precambrian Research 220–221, 107–122.

Kusky, T.M., Windley, B.F., Safonova, I., Wakita, K., Wakabayashi, J., Polat, A., Santosh, M., 2013. Recognition of plate stratigraphy in accretionary orogens through Earth history: A record of 3.8 billion years of sea floor spreading, subduction, and accretion. Gondwana

Research 24, 501-547.

Leclerc, F., Bédard, J.H, Harris, L.B., McNicoll, V.J., Goulet, N., Roy, P., Houle, P., 2011. Tholeiitic to calc-alkaline cyclic volcanism in the Roy Group, Chibougamau area, Abitibi Greenstone Belt — revised stratigraphy and implications for VHMS exploration. Canadian Journal of Earth Sciences 48, 661–694.

Li, H., Ling, M.X., Li, C.Y., Zhang, H., Ding, X., Yang, X.Y., Fan, W.M., Li, Y.L., Sun, W.D., 2012. A-type granite belts of two chemical subgroups in central eastern China: indication of ridge subduction. Lithos 150, 26-36.

Lindsley, D. H., 1968. Melting relations of plagioclase at high pressures. Origin of anorthosite and related rocks (YW Isachsen, ed.), Memoir 18, 39-46.

Lippard, S.J., Shelton, A.W., Gass, I.G., 1986. The Ophiolite of Northern Oman. Blackwell Scientific Publications, Oxford, 178 pp.

Liu, Y.S., Hu, Z.C., Zong, K.Q., Gao, C.G., Gao, S., Xu, J. and Chen, H.H., 2010. Reappraisement and refinement of zircon U-Pb isotope and trace element analyses by LA-ICP-MS. Chinese Science Bulletin 55, 1535-1546.

Ludwig, K.R., 2003. ISOPLOT 3.00: A Geochronological Toolkit for Microsoft Excel. Berkeley Geochronology Center, California, Berkeley, 39 pp.

MacKasey W.O., Blackburn C.E., Trowell N.F., 1974. A regional approach to the Wabigoon-Quetico belts and its bearing on exploration in northwestern Ontario. Ontario Division of Mines Miscellaneous Publication 58 pp 29.

Martin, H., Smithies, R.H., Rapp, R., Moyen, J.F., Champion, D., 2005. An overview of adakite, tonalite–trondhjemite–granodiorite (TTG), and sanukitoid: relationships and some implications for crustal evolution. Lithos 79, 1-24.

Melnyk, M.J., Cruden, A.R., Davis, D.W., 2000. Structural geometry and deformational chronology of the Kenora gneisses. In: Harrap, R.M., Helmstaedt, H. (Eds.), Western Superior Transect Second Annual Workshop. Lithoprobe Report 77, pp. 82-89.

Mohan, M.R., Satyanarayanan, M., Santosh, M., Sylvester, P.J., Tubrett, M., Lam, R., 2013. Neoarchean suprasubduction zone arc magmatism in southern India: Geochemistry, zircon U-Pb geochronology and Hf isotopes of the Sittampundi Anorthosite Complex. Gondwana Research 23, 539-557.

Moore, R.O., Griffin, W.L., Gurney, J.J., Ryan, C.G., Cousens, D.R., Sie, S.H., Suter, G., 1992. Trace element geochemistry of ilmenite megacrysts from the Monastery kimberlite, South Africa. Lithos 29, 1-18.

Morrison, D.A., Haskin, L., Qui, Y.Z., Phinney, W.C., MacZuga, D., 1985. Alteration in Archean anorthosite complexes. In Lunar and Planetary Science Conference Vol. 16, 589-590.

Morrison, D.A., Phinney, W.C., Maczuga, D.E., 1987. Archean anorthosites: Constraints on the accumulation process. Lunar and Planetary Institute Science Conference Abstracts Vol. 18.

Mortensen, J.K., 1993, U-Pb geochronology of the eastern Abitibi subprovince: Part 1. Chibougamau-Matagami-Joutel region: Canadian Journal of Earth Sciences, v. 30, p. 11−28.

Nagel, T.J., Hoffmann, J.E., Münker, C., 2012. Generation of Eoarchean tonalite-trondhjemite-granodiorite series from thickened mafic arc crust. Geology 40, 375-378.

Nutman, A.P., Bennett, V.C., Friend, C.R.L., Yi, K., Lee, S.R., 2015. Mesoarchaean collision of Kapisilik terrane 3070 Ma juvenile arc rocks and >3600 Ma Isukasia terrane continental crust (Greenland). Precambrian Research 258, 146–160.

Peck, W.H., Valley, J.W., 1996. The Fiskenæsset Anorthosite complex: stable isotope evidence for shallow emplacement into Archean oceanic crust. Geology 24, 523-526.

Pearce, J.A., 2008. Geochemical fingerprinting of oceanic basalts with applications to ophiolite classification and the search for Archean oceanic crust, Lithos 100, 14-48.

Pearce, J.A., Peate, D.W., 1995. Tectonic implications of the composition of volcanic arc magmas. Annual Review of Earth and Planetary Sciences 23, 251-286.

Percival, J.A., 1998. Structural transect of the central Wabigoon subprovince between the Sturgeon Lake and Obonga Lake greenstone belts. In: Current Research 1998-C, Geological Survey of Canada, pp. 127-136.

Percival, J.A., Bailes, A.H., McNicoll, V., 2001. Mesoarchean western margin of the Superior craton in the Lake Winnipeg area, Manitoba. In: Current Research 2001-C16, Geological Survey of Canada, 19 p.

Percival, J.A., Bailes, A.H., McNicoll, V., 2002. Mesoarchean breakup, Neoarchean accretion in the western Superior craton, Lake Winnipeg, Canada. Geological Association of Canada Field Trip B3 Guidebook, 42 pp.

Percival, J.A., Sanborn-Barrie, M., Stott, G., Helmstaedt, H., Skulski, T., White, D.J. 2006. Tectonic evolution of the Western Superior Province from NATMAP and LITHOPROBE studies: Canadian Journal of Earth Sciences 43, 1085-1117.

Percival, J.A., Skulski, T., Sanborn-Barrie, M., Stott, G.M., Leclair, A.D., Corkery, M.T., Boily, M., 2012. Geology and tectonic evolution of the Superior Province, Canada. In Tectonic Styles in Canada: The Lithoprobe Perspective Edited by J.A. Percival, F.A. Cook and R.M. Clowes. Geological Association of Canada Special Paper 49, pp. 321-378.

Phinney, W.C., Donald A.M., David E.M., 1988. Anorthosites and related megacrystic units in the evolution of Archean crust. Journal of Petrology 29, 1283-1323.

Polat, A., 2012. Growth of Archean continental crust in oceanic island arcs. Geology 40, 383–384.

Polat, A., 2013. Geochemical variations in Archean volcanic rocks, southwestern Greenland: Traces of diverse tectonic settings in the early Earth. Geology 41, 379-380.

Polat, A., Hofmann, A.W., 2003. Alteration and geochemical patterns in the 3.7–3.8 Ga Isua greenstone belt, West Greenland. Precambrian Research 126, 197-218.

Polat, A., Appel, P.W.U., Fryer, B., Windley, B., Frei, R., Samson. I.M., Huang, H., 2009. Trace element systematic of the Neoarchean Fiskenæsset anorthosite complex and associated metavolcanic rocks, SW Greenland: Evidence for a magmatic arc origin. Precambrian Research 175, 87-115.

Polat, A., Frei, R., Scherstén, A., Appel, P.W., 2010. New age (ca. 2970Ma), mantle source composition and geodynamic constraints on the Archean Fiskenæsset anorthosite complex, SW Greenland. Chemical Geology 277, 1-20.

Polat, A., Fryer, B.J., Appel, P.W., Kalvig, P., Kerrich, R., Dilek, Y., Yang, Z., 2011. Geochemistry of anorthositic differentiated sills in the Archean (~ 2970Ma) Fiskenæsset

Complex, SW Greenland: Implications for parental magma compositions, geodynamic setting, and secular heat flow in arcs. Lithos 123, 50-72.

Polat, A., Fryer, B.J., Samson, I.M., Weisener, C., Appel, P.W., Frei, R., Windley, B.F., 2012. Geochemistry of ultramafic rocks and hornblendite veins in the Fiskenæsset layered anorthosite complex, SW Greenland: Evidence for hydrous upper mantle in the Archean. Precambrian Research 214, 124-153.

Polat, A., Longstaffe, F.J., 2014. A juvenile oceanic island arc origin for the Archean (ca. 2.97 Ga) Fiskenæsset Anorthosite Complex, southwestern Greenland: Evidence from oxygen isotopes. Earth and Planetary Science Letters 396, 252-266.

Polat, A., Wang, L., Appel, P.W.U., 2015. A review of structural patterns and melting processes in the Archean craton of West Greenland: Evidence for crustal growth at convergent plate margins as opposed to non-uniformitarian models. Tectonophysics, http://dx.doi.org/10.1016/j.tecto.2015.04.006.

Rao, C.D., Santosh, M., Sajeev, K., Windley, B.F., 2013. Chromite–silicate chemistry of the Neoarchean Sittampundi Complex, southern India: Implications for subduction-related arc magmatism. Precambrian Research 227, 259-275.

Riccio, L., 1981, Geology of the northeastern portion of the Shawmere anorthosite complex, District of Sudbury: Ontario Geological Survey Open File Report 5338, 113 pp.

Rollinson, H., Claire R., Brian W., 2010. Chromitites from the Fiskenæsset Anorthositic Complex, West Greenland: clues to late Archean mantle processes. Geological Society, London, Special Publications 338, 197-212.

Sanborn-Barrie, M., Skulski, T., Parker, J.R., 2001. Three hundred million years of tectonic history recorded by the Red Lake greenstone belt, Ontario. In: Current Research 2001-C19, Geological Survey of Canada 19 pp.

Santosh, M., Shaji, E., Tsunogae, T., Ram Mohan, M., Satyanarayanan, M., Horie, K., 2013. Suprasubduction zone ophiolite from Agali hill: Petrology, zircon SHRIMP U–Pb geochronology, geochemistry and implications for Neoarchean plate tectonics in southern India. Precambrian Research 231, 301–324.

Souders, A.K., Sylvester, P.J., Myers, J.S., 2013. Mantle and crustal sources of Archean anorthosite: a combined in situ isotopic study of Pb-Pb in plagioclase and Lu-Hf in zircon. Contributions to Mineralogy and Petrology 165, 1-24.

Stott, G.M., Corfu, F., 1991. Uchi Subprovince. In: Thurston, P.C., Williams, H.R., Sutcliffe, R.H., Stott, G.M. (Eds.), Geology of Ontario. Ontario Geological Survey Special Volume 4, Pt. 1, pp. 145-238.

Stott, G.M., 1997. The Superior Province, Canada. In: de Wit, M.J., Ashwal, L.D. (Eds.), Greenstone Belts. Oxford Monographs Geology and Geophysics, vol. 35. Oxford, Clarendon, pp. 480-507.

Sun, S.S., McDonough, W.F., 1989. Chemical and isotopic systematics of oceanic basalts: implications for mantle composition and processes. In: Saunders, A.D., Norry, M.J. (Eds.), Magmatism in the Ocean Basins. Geological Society of London Special Publication 42, pp. 313-345.

Szilas, K., Hoffmann, J.E., Schersten, A., Kokfelt, T.F., Münker, C., 2013a. Archean andesite petrogenesis: Insights from the Gradefjord Supracrustal Belt, southern West Greenland. Precambrian Research 235, 1-15.

Szilas, K., Hoffmann, J.E., Schersten, A., Rosing, M., Windley, B.F., Kokfelt, T.F., Keulen, N., van Hinsberg, V.J., Naraa, T., Frei, R., Munker, C., 2012. Complex calc-alkaline volcanism recorded in Mesoarchean supracrustal belts north of Frederikshab Isblink, southern West Greenland: Implication for subduction zone processes in the early Earth. Precambrian Research 208-211, 90-123.

Szilas, K., Van Hinsberg, V.J., Kisters, A.F.M., Hoffmann, J.E., Windley, B.F., Kokfelt, T.F., Schersten, A., Frei, R., Rosing, M.T., Münker, C., 2013b. Remnants of arc-related Mesoarchean oceanic crust in the Tartoq Group of SW Greenland. Gondwana Research 23, 436-451.

Tagai, T., Ichikawa, J., Takeda, H., Morrison, D.A., 1988. Crystallographic investigations of calcic plagioclase from the Bad Vermilion Lake Anorthosite Complex, Ontario. In Lunar and Planetary Institute Science Conference Abstracts Vol. 19, p. 1167.

Takagi, D., Sato, H., Nakagawa, M., 2005. Experimental study of a low-alkali tholeiite at 1–5 kbar: optimal condition for the crystallization of high-An plagioclase in hydrous arc tholeiite. Contributions to Mineralogy and Petrology 149, 527-540.

Taylor Jr, H.P., Epstein, S., 1962a. Relationship between O^{18}/O^{16} ratios in coexisting minerals of igneous and metamorphic rocks. Part 1. Application to petrologic problems. Geological Society of America Bulletin 73, 461–480.

Taylor Jr, H.P., Epstein, S., 1962b. Relationship between O^{18}/O^{16} ratios in coexisting minerals of igneous and metamorphic rocks. Part 2. Principles and experimental results. Geological Society of America Bulletin 73, 675–694.

Thurston, P.C., 2002. Autochthonous development of Superior Province greenstone belts. Precambrian Research 115, 11–36.

Thurston, P.C., Osmani, I.A., Stone, D., 1991. Northwestern Superior Province: review and terrane analysis. In: Thurston, P.C., Williams, H.R., Sutcliffe, R.H., Stott, G.M. (Eds.), Geology of Ontario. Ontario Geological Survey Special Volume 4, Pt. 1, pp. 81–144.

Thurston, P.C, Sage, R.P., Siragusa, G.M., 1979. Geology of the Winisk Lake Area, District of Kenora, Patricia Portion. Ontario Ministry of Natural Resources, Ontario Geological Survey Report 193, 169 pp.

Trueman, D.L., 1971. Petrological, structural and magnetic studies of a layered basic intrusion, Bird River Sill, Manitoba. Master's Thesis, University of Manitoba. Winnipeg, Manitoba, Canada.

Valley, J.W., 1986. Stable isotope geochemistry of metamorphic rocks. In: Valley, J.W., Taylor, H.P., O'Neil, J.R. (Eds.), Stable Isotopes in High Temperature Geological Processes. In: Mineralogical Society of America Reviews in Mineralogy vol. 16, pp. 445–489.

Whalen, J.B., Currie, K.L., Chappell, B.W., 1987. A-type granites geochemical characteristics, discrimination and petrogenesis. Contributions to Mineralogy and Petrology 95, 407-419.

Whalen, J.B., McNicoll, V., Longstaffe, F.J., 2004. Juvenile ca. 2.735–2.720 Ga high- and low-Al tonalitic plutons: implications for TTG and VMS petrogenesis, western Superior

Province, Canada. Precambrian Research 132, 275–301.

Westerman, C.J., 1978. Tectonic evolution of a part of the English River Subprovince, northwestern Ontario. Ph.D. thesis, McMaster University. Hamilton, Ontario, Canada, 292 p.

Williams, H.R., Stott, G.M., Thurston, P.C., Sutcliffe, R.H., Bennett, G., Easton, R.M., Armstrong, D.K., 1992. Tectonic evolution of Ontario: summary and synthesis. In: Thurston, P.C., Williams, H.R., Sutcliffe, R.H., Stott, G.M. (Eds.), Geology of Ontario. Ontario Geological Survey Special Volume 4, Pt. 2, pp. 1255–1332.

Windley, B.F., 1973. Archean anorthosites: a review with the Fiskenæsset Complex, West Greenland, as a model for interpretation. Geological Society of South Africa., Special Publication 3, 319-332.

Windley, B.F., 1995. The evolving continents (3rd ed.). London, Wiley, 526 p.

Wood, J., 1980. Epiclastic sedimentation and stratigraphy in the North Spirit Lake and Rainy Lake areas: a comparison. Precambrian Research 12, 227-255.

Wood, J., Dekker, J., Jansen, J.G., Keay, J.P., Panagapko, D., 1980. Mine Center Area, District of Rainy River. Ontario Geological Survey Preliminary Maps P2201 and P2202; Geological series, Scale, 1:15, 840

Wu, Y., Zheng, Y., 2004. Genesis of zircon and its constraints on interpretation of U-Pb age. Chinese Science Bulletin 49, 1554-1569.

FIGURE CAPTIONS

Fig. 1. World map showing the locations of known Archean anorthosites (solid black circles) and areas known or suspected to be underlain by Archean rocks and reworked equivalents (shaded). The solid red circle is the location of the BVLA Complex. Base map modified from Condie (1982) and de Wit et al. (1988).

Fig. 2. Location of the Wabigoon subprovince within the Superior Province (modified from Card and Ciesielski, 1986).

Fig. 3. Geological map of the Bad Vermilion Lake region.

Fig. 4. Geologic map of the BVLA Complex (modified from Ashwal et al., 1983).

Fig. 5. Field photographs illustrating primary igneous lithological characteristics and field relationships of the Bad Vermilion Lake Complex. (a) Field relationship between the gabbro and anorthosite layers. (b) Field relationship between the leucogabbro and anorthosite. (c-d) Photographs of the anorthosite and gabbro. (e-f) Granitic rocks.

Fig. 6. Photomicrographs illustrating petrographic characteristics of the Bad Vermilion Lake Complex. (a-b) Anorthosite with primary coarse, euhedral plagioclase grains. (c-d) Gabbro with abundant chlorite group minerals. (e-f) Anorthosite containing plagioclase altered to epidote

group minerals. (g-h) Anorthosite with epidote alteration and relict plagioclase.

Fig. 7. Scanning Electron Microscope (SEM) with backscattered electron (BSE) images for rocks from different lithological units in the BVLA Complex. (a) Igneous cumulate textures of the anorthosite. (b-d) Primary and altered (to albite and epidote) plagioclase grains in the anorthosite; mafic matrix is altered to chlorite. (e-f) Primary and altered (to epidote) plagioclase grains in the gabbro, containing magnetite grains. (g-h) Titanium-rich minerals, such as rutile and titanite, which are abundant in Group 2 gabbro samples.

Fig. 8. Photomicrographs illustrating petrographic characteristics of granitic rocks associated with the BVLA Complex. The granitic rocks are composed of 55% quartz, 25% plagioclase (some altered to epidote), 5-10% K-feldspar, 10% biotite and 5% accessory minerals.

Fig. 9. Cathodoluminescence (CL) images of zircons from granitic sample BVL2013-042. The red circles show LA-ICP-MS dating spots.

Fig. 10. Cathodoluminescence (CL) images of zircons from granitic sample BVL2013-043. The red circles show LA-ICP-MS dating spots.

Fig. 11. Zircon U/Pb concordia diagram for the analyzed granitic samples, providing ages of

2716±18 Ma and 2649±17 Ma, respectively.

Fig. 12. SiO_2 (wt.%) versus CaO (wt.%), TiO_2 (wt.%), Al_2O_3 (wt.%), and Fe_2O_3 (wt.%) for the BVLA Complex.

Fig. 13. (a-e). MgO (wt.%) versus Al_2O_3 (wt.%), CaO (wt.%), Fe_2O_3 (wt.%), Ni (ppm) and Co plots for the Bad Vermilion Lake Complex, and (f) Al_2O_3 (wt.%) versus Fe_2O_3 (wt.%) plots for the BVLA Complex.

Fig. 14. Zr (ppm) versus TiO_2 (wt.%), Nb (ppm), Sm (ppm), and Nd (ppm) variation diagrams for the BVLA Complex, suggesting a co-magmatic origin for these rocks.

Fig. 15. (a-c). Chondrite-normalized REE patterns for the Bad Vermilion Lake anorthosite, gabbro and leucogabbro. Normalization values are from Sun and McDonough (1989). (d-f). Primitive mantle-normalized trace element patterns for the Bad Vermilion Lake anorthosite, gabbro and leucogabbro. Normalization values are from Hofmann (1988).

Fig. 16. (a). Chondrite-normalized REE patterns for the Bad Vermilion Lake granitic rocks. Normalization values are from Sun and McDonough (1989). (b). Primitive mantle-normalized trace element patterns for the Bad Vermilion Lake granitic rocks. Normalization values are from Hofmann (1988).

Fig. 17. Whole-rock $\delta^{18}O$(‰) versus (a) Ce/Ce*, (b) Nb/Nb*, (c) Mg# and (d) Al_2O_3 for the BVLA Complex.

Fig. 18. Comparison of the trace element geochemistry of gabbros from the BVLA Complex with gabbros from Cenozoic oceanic arc (e.g. Aleutian Arc, Mariana Arc, Scotia Arc and Tonga Arc), gabbros from the Semail Ophiolite in Oman and gabbros from South West Indian Ridge. (a) Nb/Nb* versus La/Sm_{cn}. (b) Th/Nb versus La/Nb. Both Group 1 and Group 2 gabbros from the BVLA Complex plot predominantly within the field of gabbros from Cenozoic oceanic arc setting. Data for Cenozoic arcs were obtained from GEOROC database (http://georoc.mpch-mainz.gwdg.de). Data from the Oman ophiolite are for samples from the Wadi Abyad section in the south-central part of the ophiolite following the lithological division of MacLeod and Yaouancq (2000). Data for South West Indian Ridge are from Coogan et al. (2001).

Fig. 19. Schematic model illustrating the proposed geodynamic evolution of the BVLA Complex and associated granitic rocks.


80
40
0
40
Archean Terranes
Rest of the world
Archean anorthosites locations
The Bad Vermilion Lake
Anorthosite Complex
180
80 140
100
60
20
20
60
100
140
180

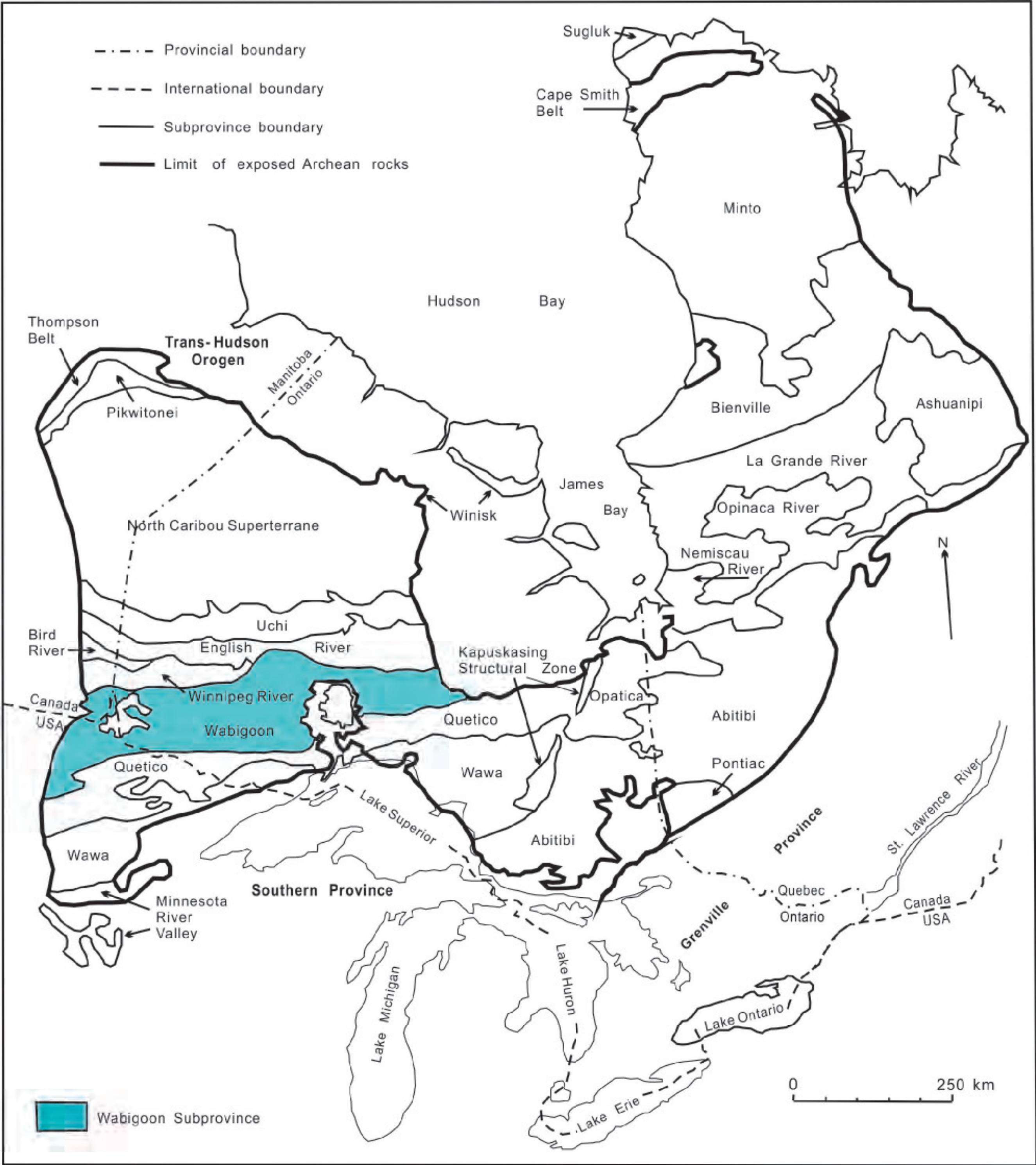

Provincial boundary
International boundary
Subprovince boundary
Limit of exposed Archean rocks
Sugluk
Cape Smith Belt
Minto
Hudson Bay
Thompson Belt
Trans-Hudson Orogen
Manitoba
Ontario
Pikwitonei
Bienville
Ashuanipi
La Grande River
James Bay
Opinaca River
Winisk
North Caribou Superterrane
Nemiscau River
N
Uchi
Bird River
English River
Kapuskasing Structural Zone
Winnipeg River
Opatica
Canada
USA
Wabigoon
Quetico
Abitibi
Quetico
Wawa
Pontiac
Lake Superior
Province
St. Lawrence River
Abitibi
Wawa
Southern Province
Quebec
Ontario
Canada
USA
Minnesota River Valley
Grenville
Lake Huron
Lake Michigan
Lake Ontario
0
250 km
Lake Erie
Wabigoon Subprovince

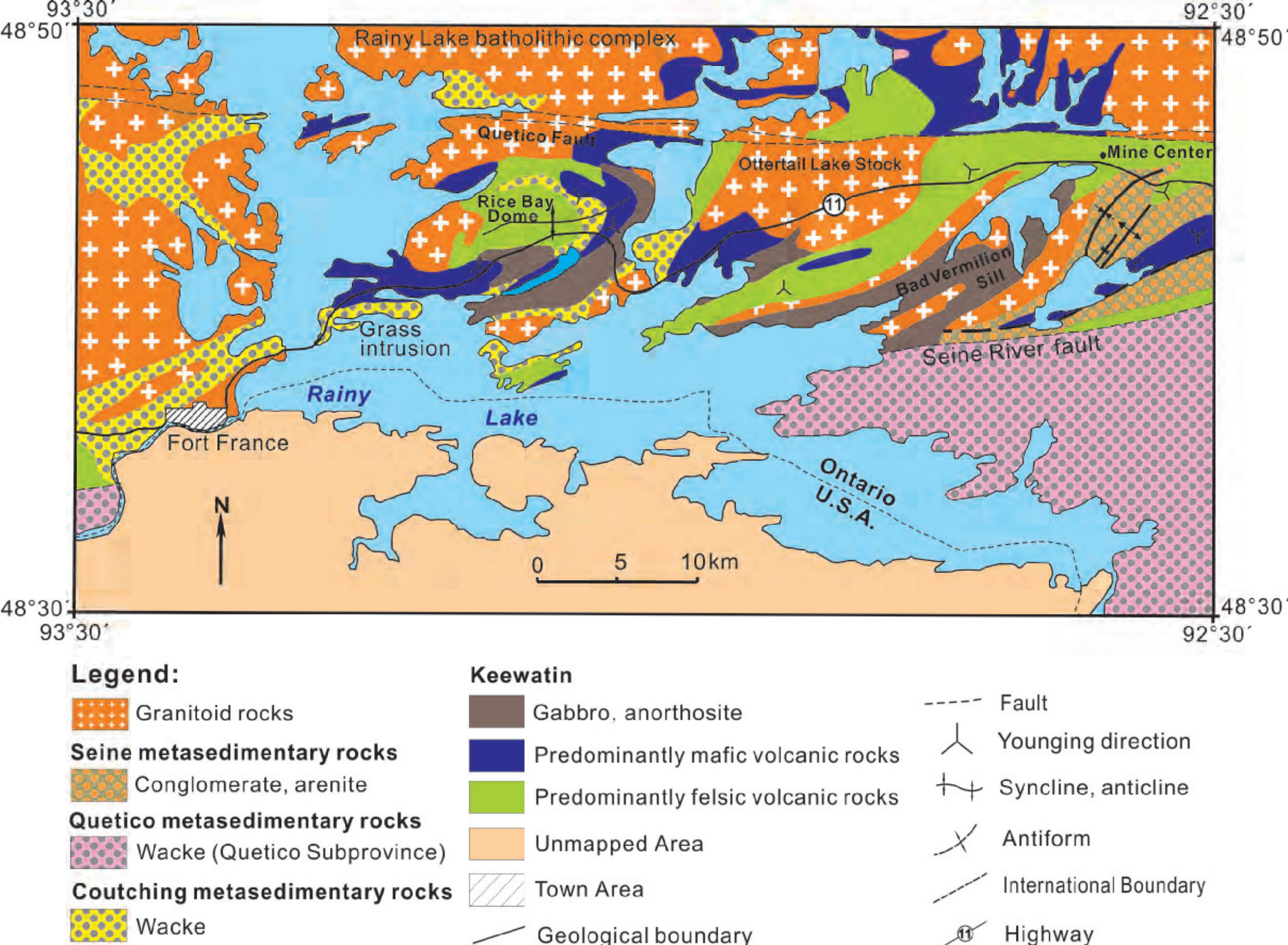

93°30′
92°30′
48°50′
48°30′
Rainy Lake batholithic complex
Quetico Fault
Ottertail Lake Stock
Mine Center
Rice Bay Dome
11
Bad Vermilion Sill
Grass intrusion
Seine River fault
Rainy
Lake
Fort France
Ontario
U.S.A.
N
0
5
10km
Legend:
Granitoid rocks
Seine metasedimentary rocks
Conglomerate, arenite
Quetico metasedimentary rocks
Wacke (Quetico Subprovince)
Coutching metasedimentary rocks
Wacke
Keewatin
Gabbro, anorthosite
Predominantly mafic volcanic rocks
Predominantly felsic volcanic rocks
Unmapped Area
Town Area
Geological boundary
Fault
Younging direction
Syncline, anticline
Antiform
International Boundary
Highway

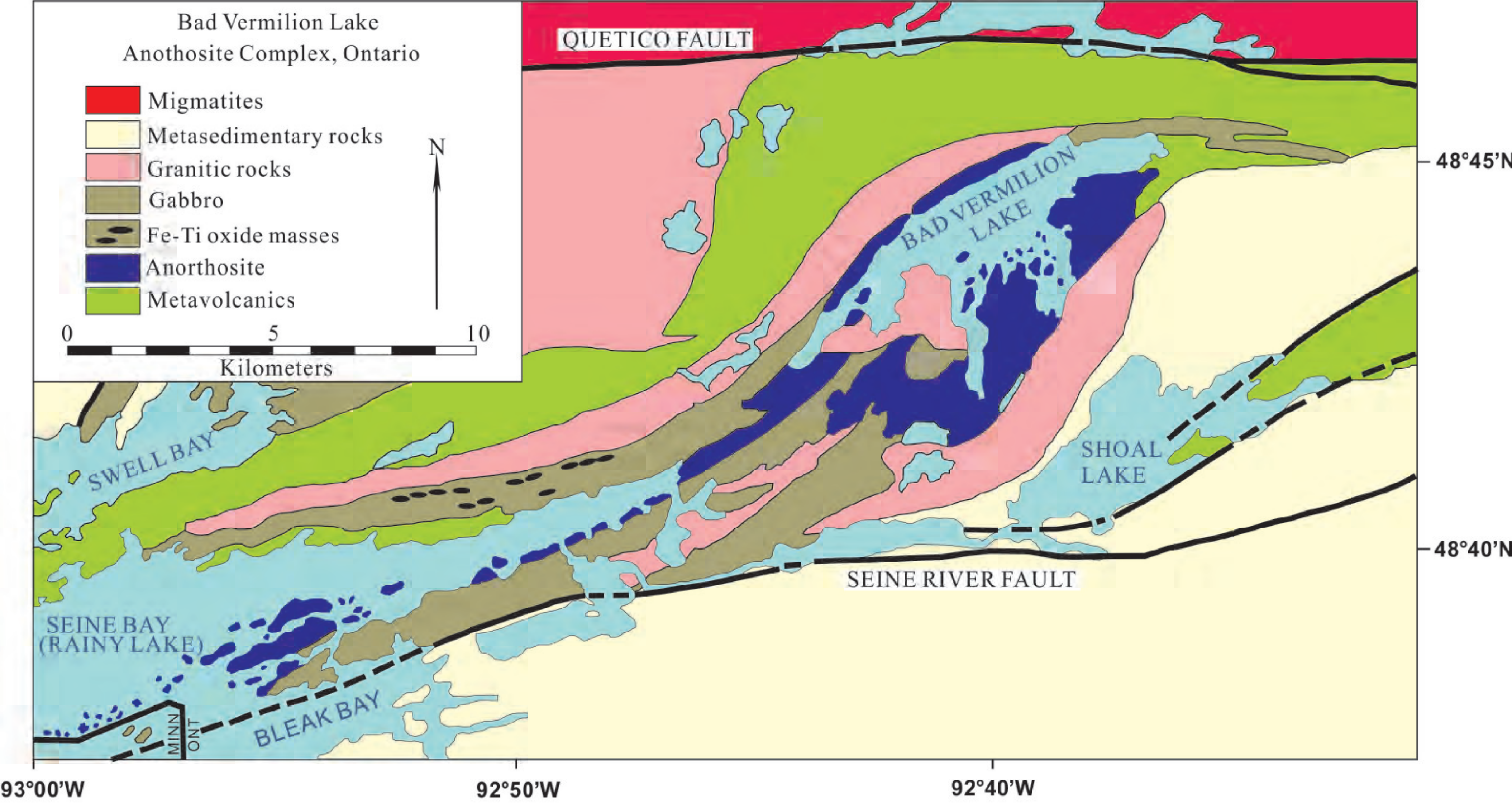
Bad Vermilion Lake
Anothosite Complex, Ontario
Migmatites
Metasedimentary rocks
Granitic rocks
Gabbro
Fe-Ti oxide masses
Anorthosite
Metavolcanics
N
0
5
10
Kilometers
QUETICO FAULT
BAD VERMILION LAKE
SWELL BAY
SHOAL LAKE
SEINE RIVER FAULT
SEINE BAY (RAINY LAKE)
BLEAK BAY
MINN
ONT
48°45'N
48°40'N
93°00'W
92°50'W
92°40'W

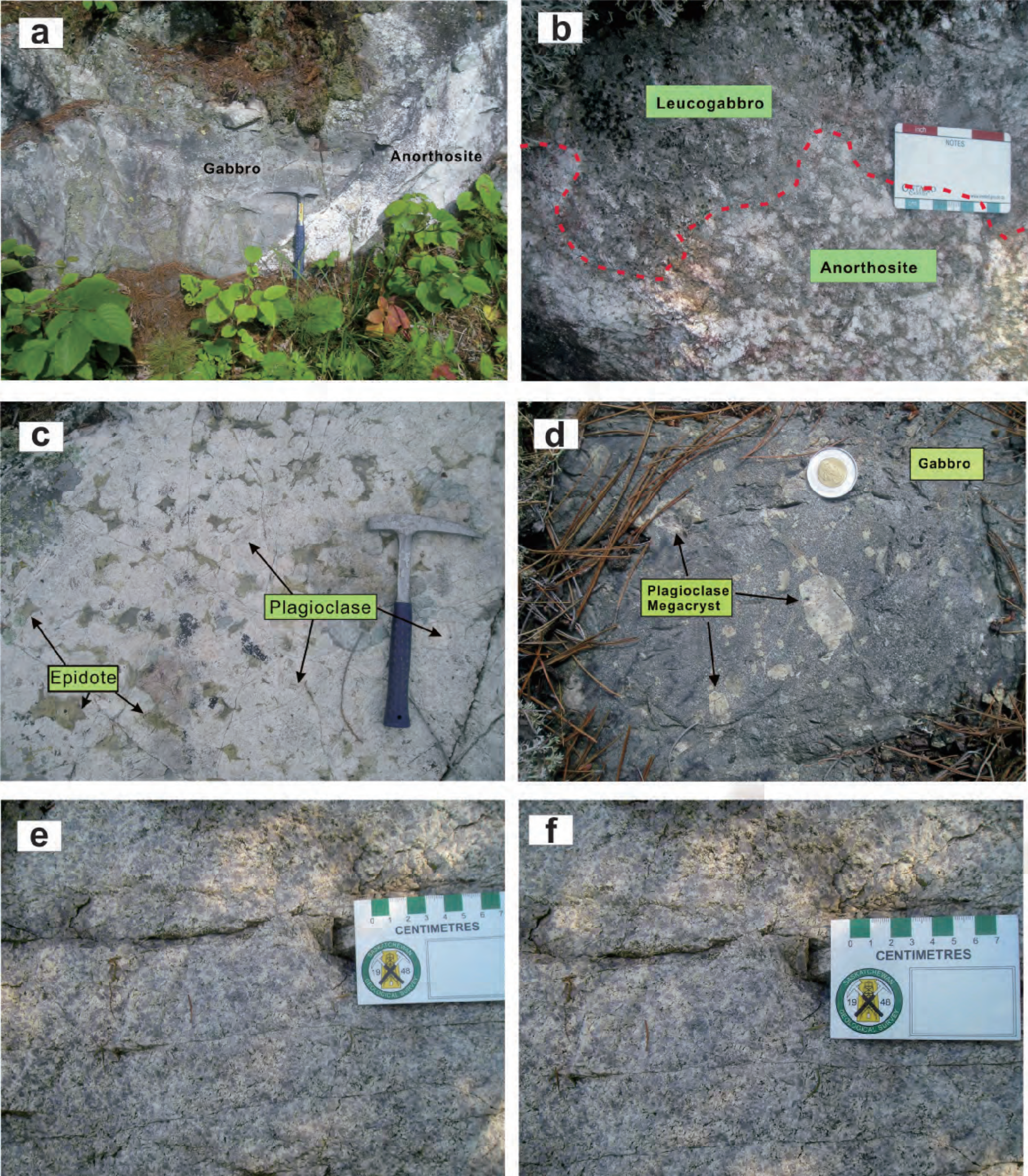
a
Gabbro
Anorthosite
b
Leucogabbro
Anorthosite
c
Plagioclase
Epidote
d
Gabbro
Plagioclase
Megacryst
e
CENTIMETRES
SASKATCHEWAN
GEOLOGICAL SURVEY
f
CENTIMETRES
SASKATCHEWAN
GEOLOGICAL SURVEY

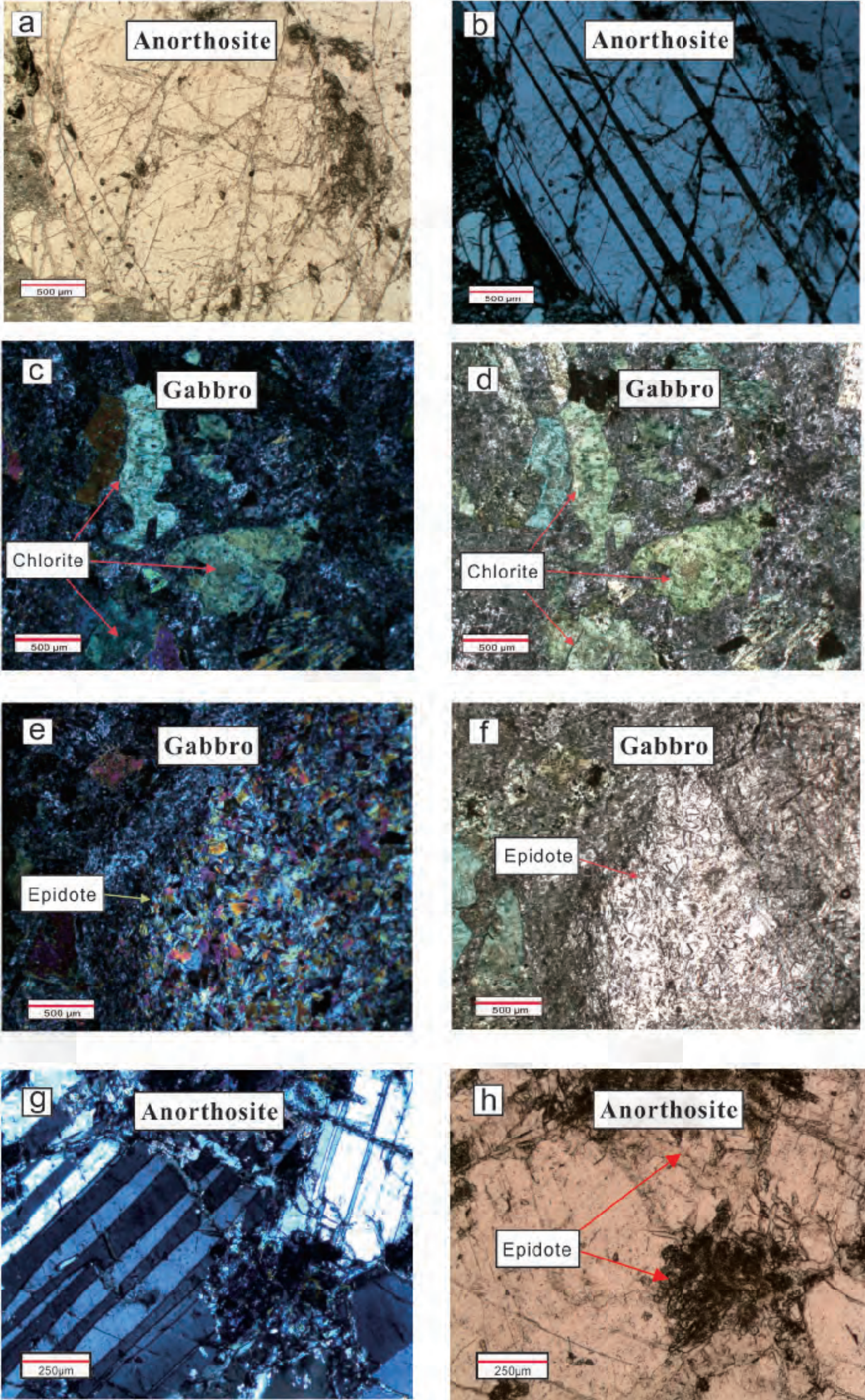
a
Anorthosite
500 μm
b
Anorthosite
500 μm
c
Gabbro
Chlorite
500 μm
d
Gabbro
Chlorite
500 μm
e
Gabbro
Epidote
500 μm
f
Gabbro
Epidote
500 μm
g
Anorthosite
250μm
h
Anorthosite
Epidote
250μm

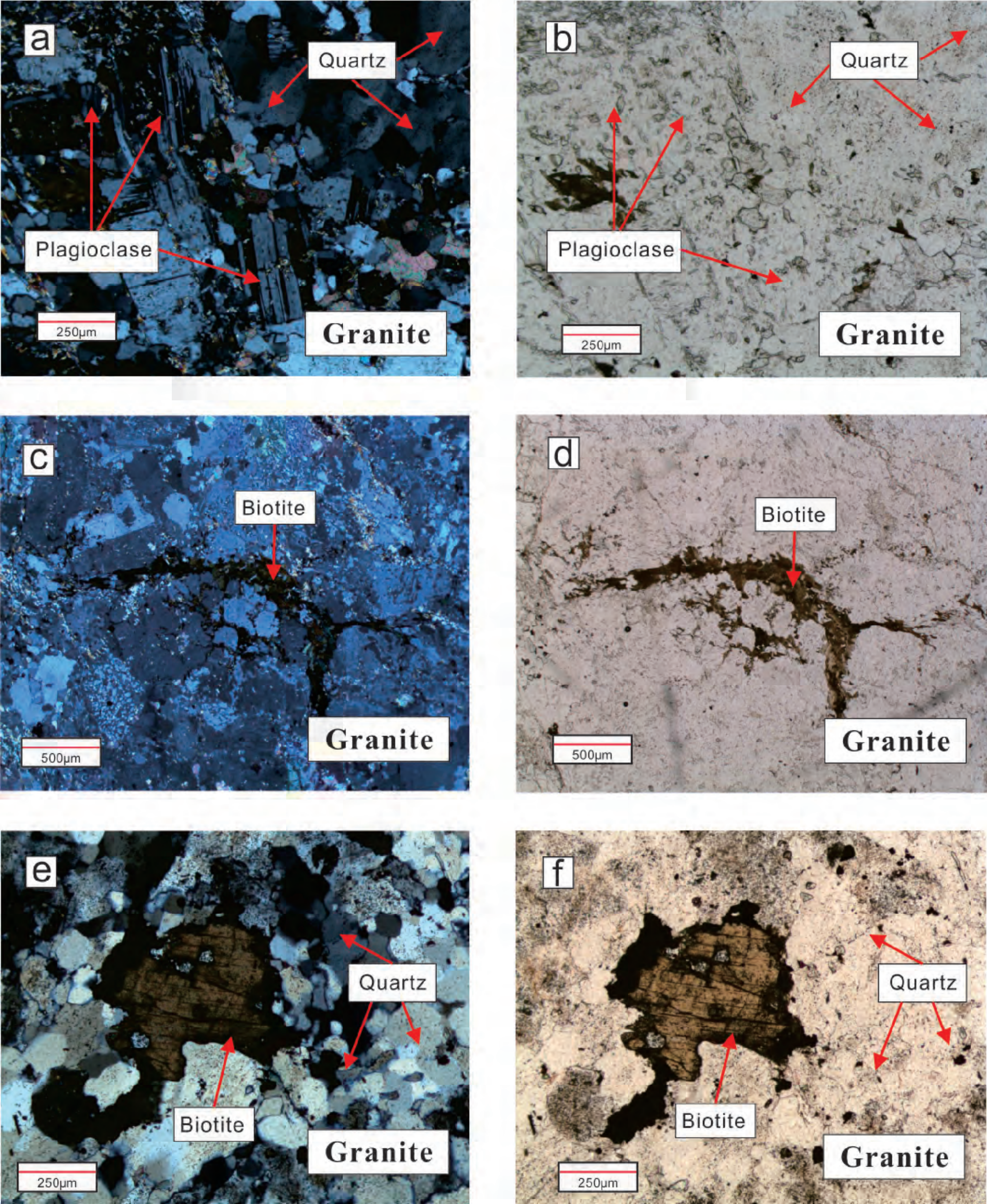
a
Quartz
Plagioclase
250μm
Granite
b
Quartz
Plagioclase
250μm
Granite
c
Biotite
500μm
Granite
d
Biotite
500μm
Granite
e
Quartz
Biotite
250μm
Granite
f
Quartz
Biotite
250μm
Granite

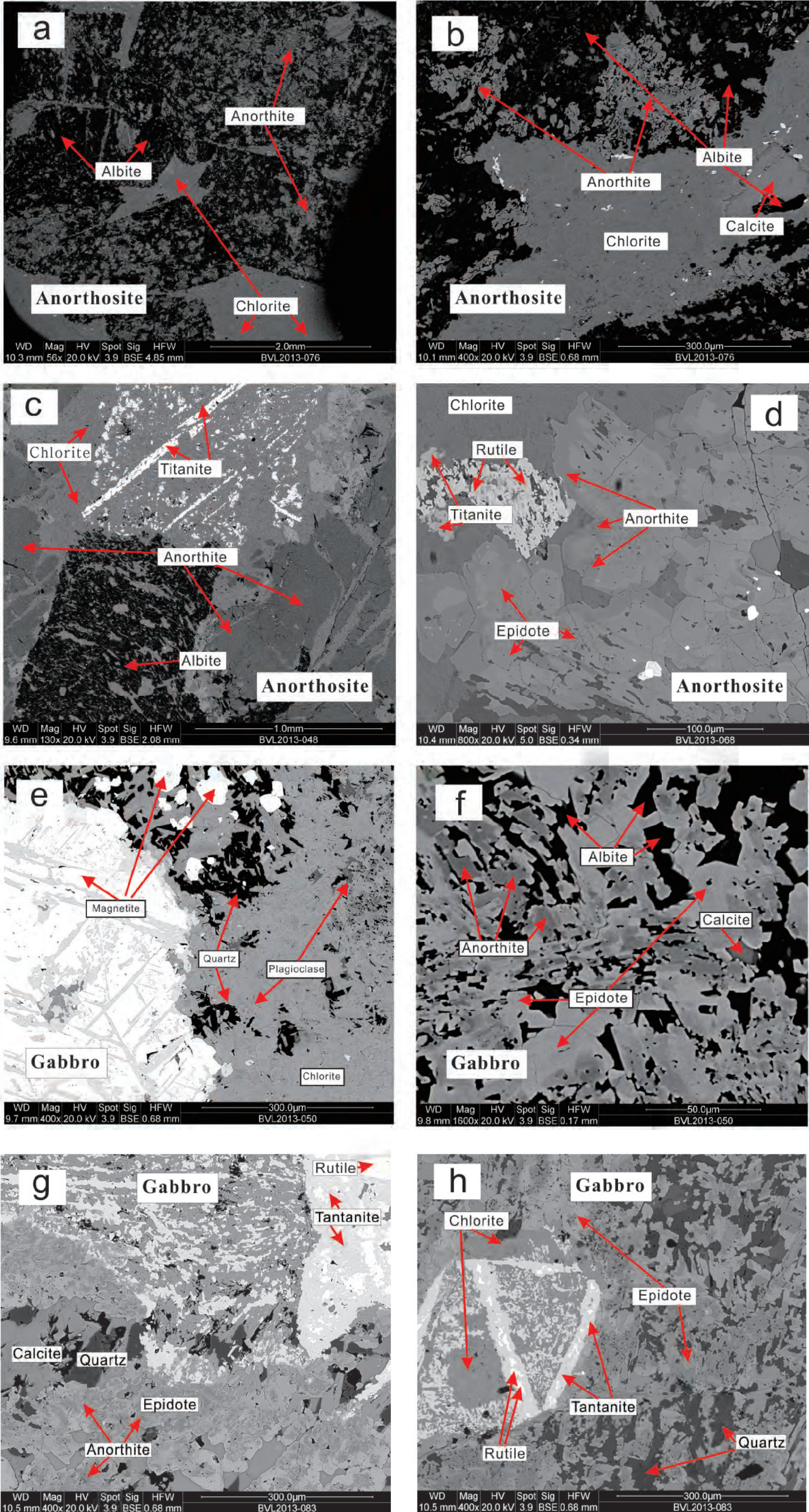
a
Anorthite
Albite
Chlorite
Anorthosite
WD Mag HV Spot Sig HFW
10.3 mm 56x 20.0 kV 3.9 BSE 4.85 mm
2.0mm
BVL2013-076
b
Albite
Anorthite
Calcite
Chlorite
Anorthosite
WD Mag HV Spot Sig HFW
10.1 mm 400x 20.0 kV 3.9 BSE 0.68 mm
300.0µm
BVL2013-076
c
Chlorite
Titanite
Anorthite
Albite
Anorthosite
WD Mag HV Spot Sig HFW
9.6 mm 130x 20.0 kV 3.9 BSE 2.08 mm
1.0mm
BVL2013-048
d
Chlorite
Rutile
Titanite
Anorthite
Epidote
Anorthosite
WD Mag HV Spot Sig HFW
10.4 mm 800x 20.0 kV 5.0 BSE 0.34 mm
100.0µm
BVL2013-068
e
Magnetite
Quartz
Plagioclase
Chlorite
Gabbro
WD Mag HV Spot Sig HFW
9.7 mm 400x 20.0 kV 3.9 BSE 0.68 mm
300.0µm
BVL2013-050
f
Albite
Calcite
Anorthite
Epidote
Gabbro
WD Mag HV Spot Sig HFW
9.8 mm 1600x 20.0 kV 3.9 BSE 0.17 mm
50.0µm
BVL2013-050
g
Gabbro
Rutile
Tantanite
Calcite
Quartz
Epidote
Anorthite
WD Mag HV Spot Sig HFW
10.5 mm 400x 20.0 kV 3.9 BSE 0.68 mm
300.0µm
BVL2013-083
h
Gabbro
Chlorite
Epidote
Tantanite
Rutile
Quartz
WD Mag HV Spot Sig HFW
10.5 mm 400x 20.0 kV 3.9 BSE 0.68 mm
300.0µm
BVL2013-083

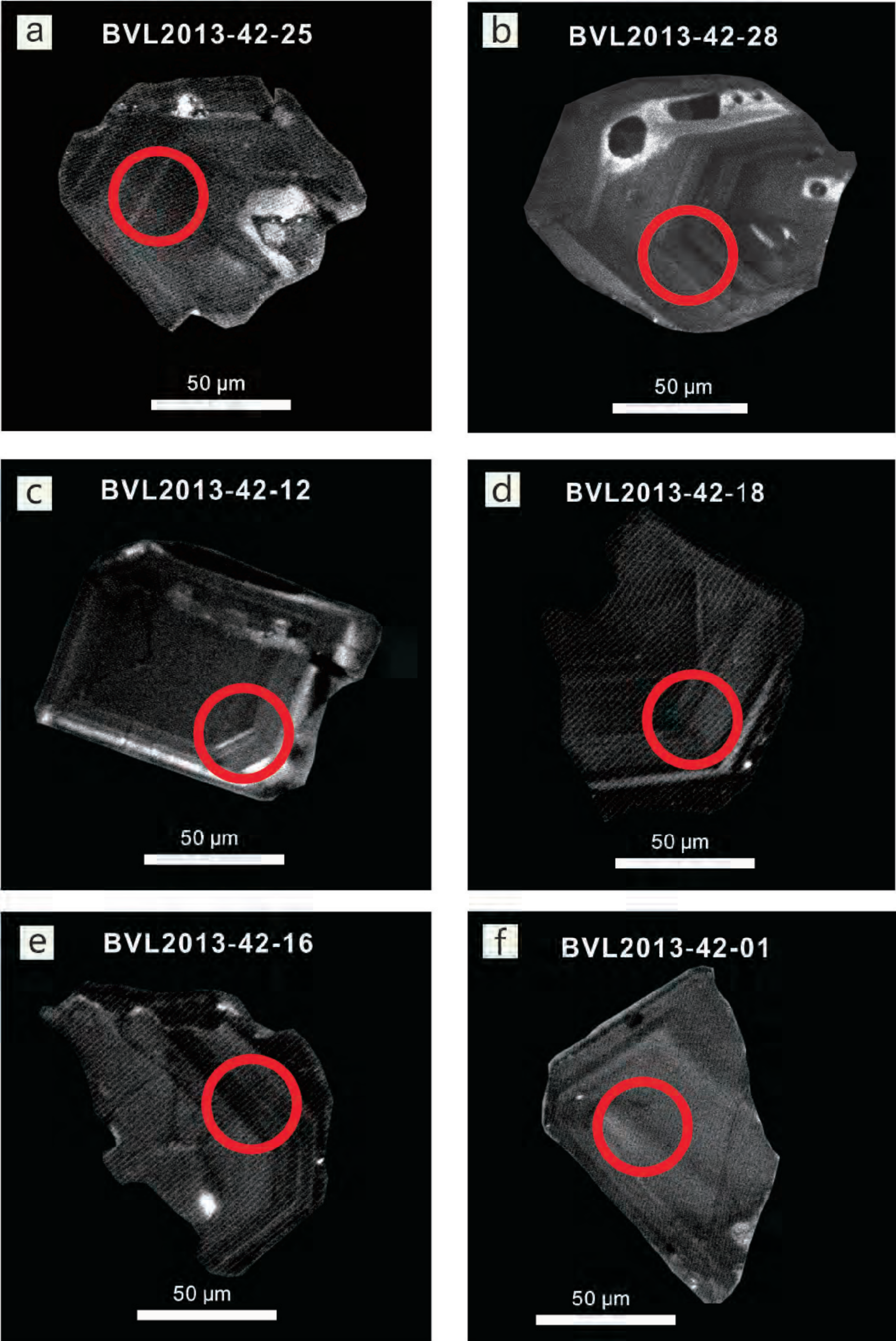
a
BVL2013-42-25
50 μm
b
BVL2013-42-28
50 μm
c
BVL2013-42-12
50 μm
d
BVL2013-42-18
50 μm
e
BVL2013-42-16
50 μm
f
BVL2013-42-01
50 μm


a
BVL2013-043-1
100 μm
b
BVL2013-043-2
100 μm
c
BVL2013-043-3
100 μm
d
BVL2013-043-6
100 μm
e
BVL2013-043-26
100 μm
f
BVL2013-043-27
100 μm

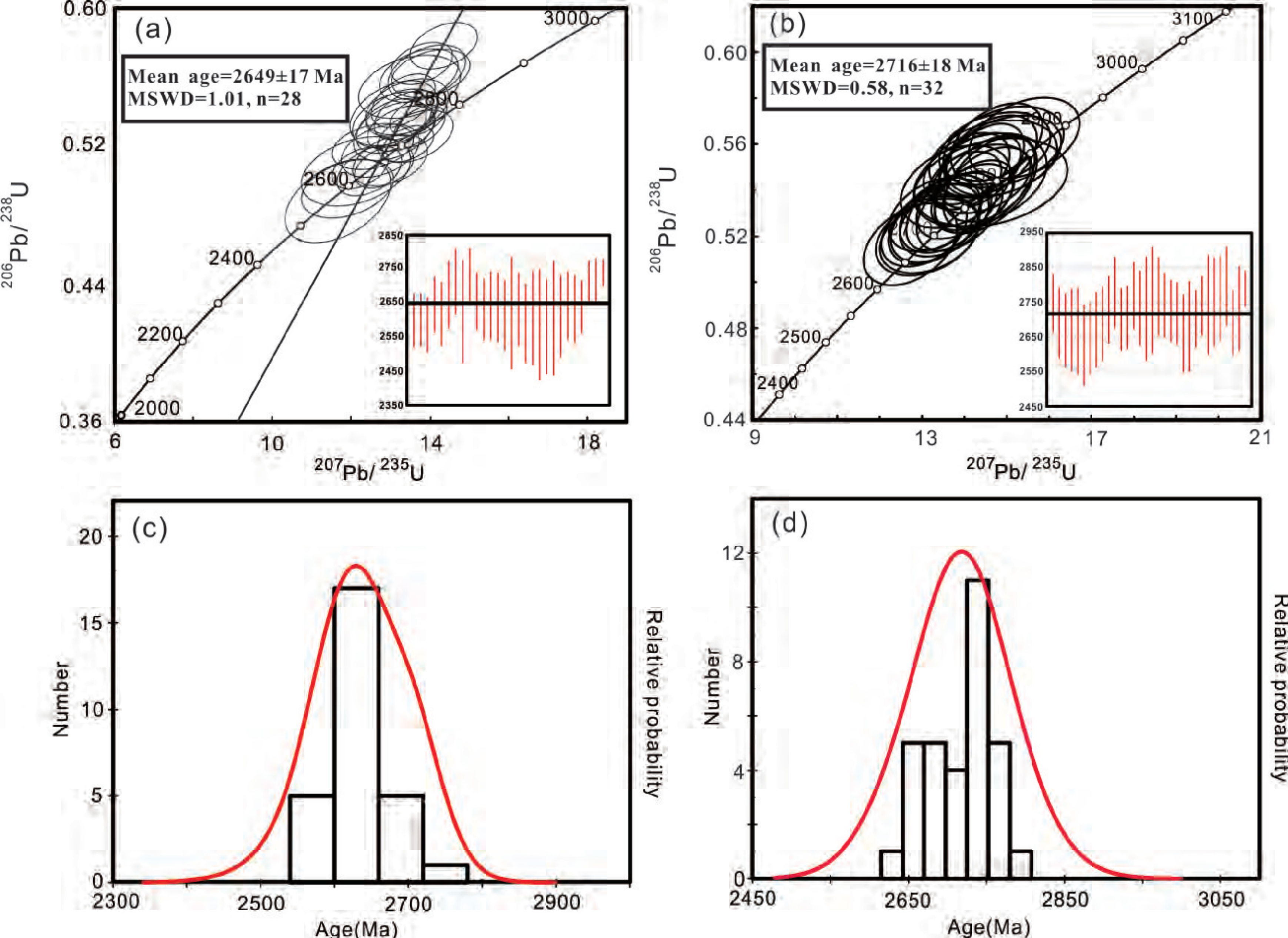

(a)
Mean age=2649±17 Ma
MSWD=1.01, n=28
$^{206}Pb/^{238}U$
$^{207}Pb/^{235}U$
(b)
Mean age=2716±18 Ma
MSWD=0.58, n=32
$^{206}Pb/^{238}U$
$^{207}Pb/^{235}U$
(c)
Number
Relative probability
Age(Ma)
(d)
Number
Relative probability
Age(Ma)

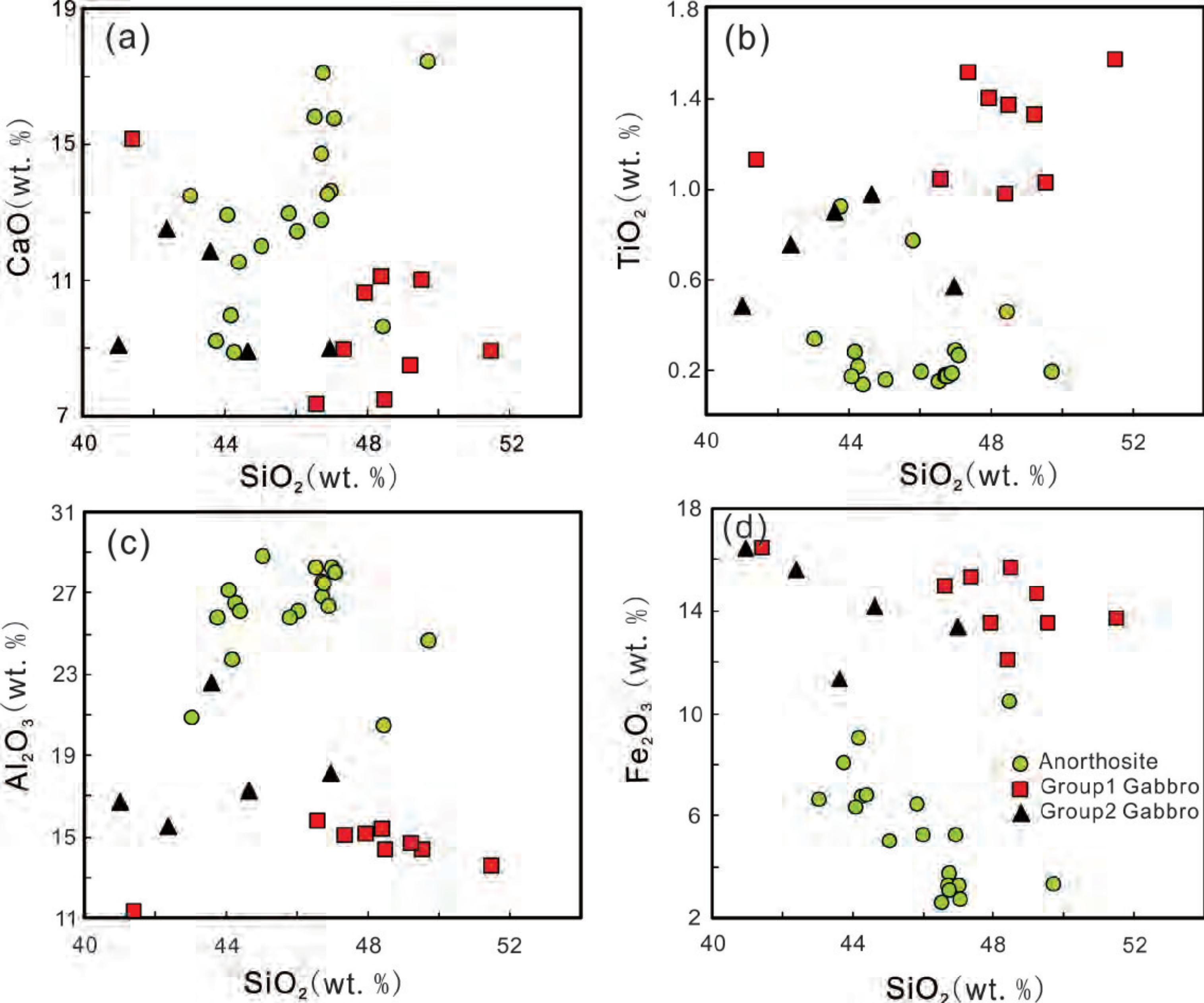

(a)
CaO (wt. %)
SiO2 (wt. %)
(b)
TiO2 (wt. %)
SiO2 (wt. %)
(c)
Al2O3 (wt. %)
SiO2 (wt. %)
(d)
Fe2O3 (wt. %)
SiO2 (wt. %)
Anorthosite
Group1 Gabbro
Group2 Gabbro

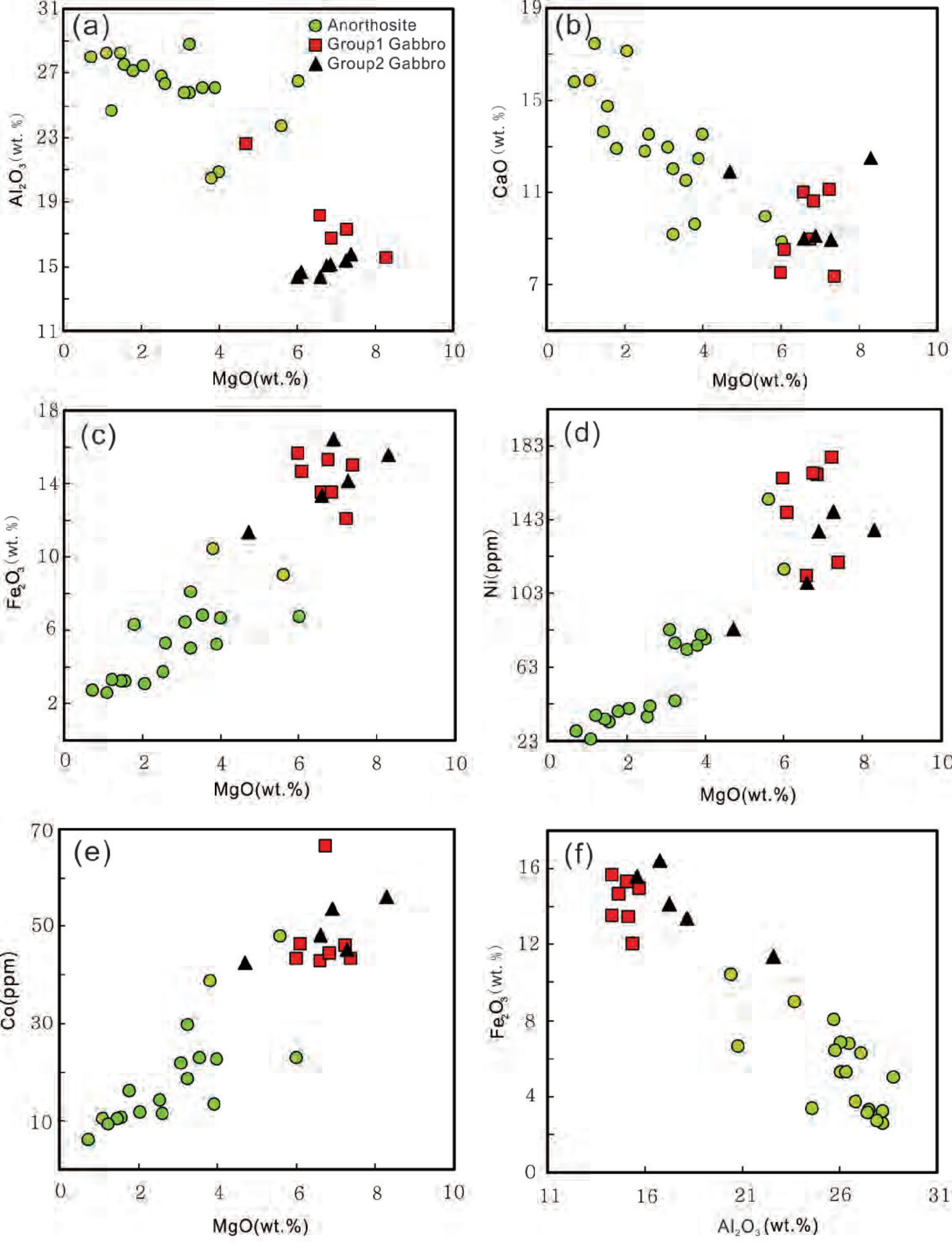

(a)
Anorthosite
Group1 Gabbro
Group2 Gabbro
Al_2O_3 (wt. %)
MgO(wt.%)
(b)
CaO (wt. %)
MgO(wt.%)
(c)
Fe_2O_3 (wt. %)
MgO(wt.%)
(d)
Ni(ppm)
MgO(wt.%)
(e)
Co(ppm)
MgO(wt.%)
(f)
Fe_2O_3 (wt. %)
Al_2O_3 (wt.%)

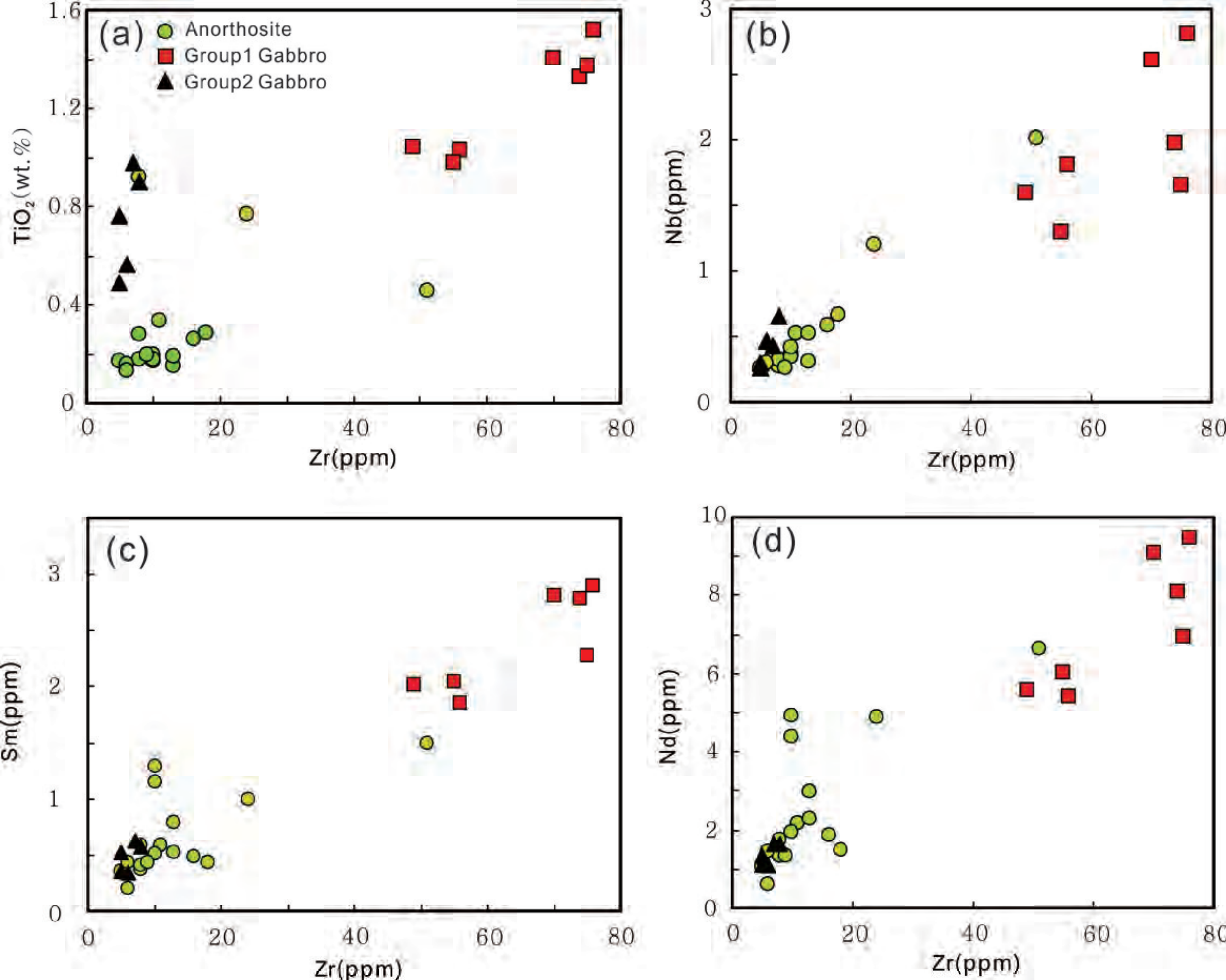
(a)
Anorthosite
Group1 Gabbro
Group2 Gabbro
TiO_2 (wt. %)
Zr(ppm)
(b)
Nb(ppm)
Zr(ppm)
(c)
Sm(ppm)
Zr(ppm)
(d)
Nd(ppm)
Zr(ppm)

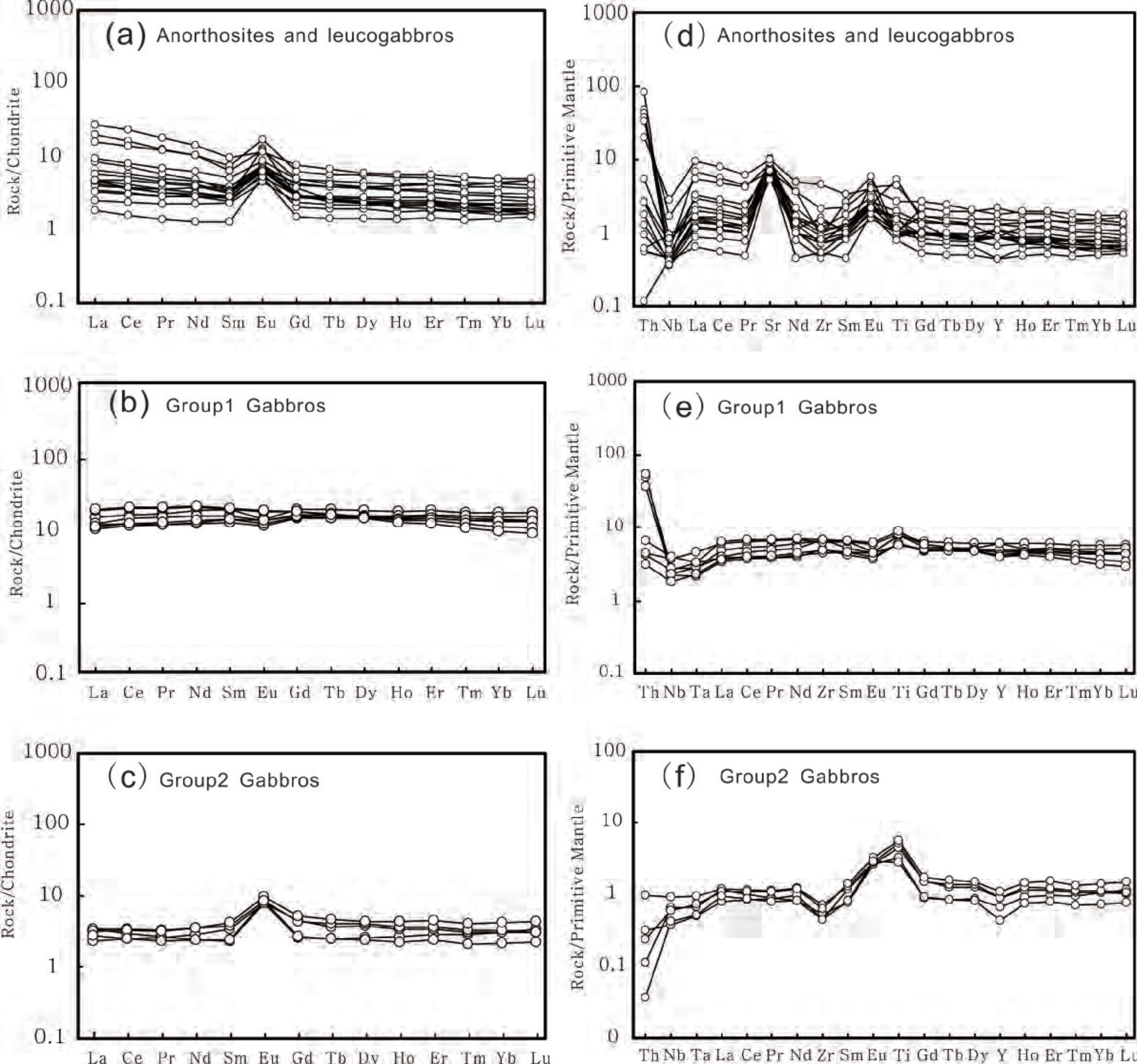
(a) Anorthosites and leucogabbros
Rock/Chondrite
1000
100
10
1
0.1
La Ce Pr Nd Sm Eu Gd Tb Dy Ho Er Tm Yb Lu
(d) Anorthosites and leucogabbros
Rock/Primitive Mantle
1000
100
10
1
0.1
Th Nb La Ce Pr Sr Nd Zr Sm Eu Ti Gd Tb Dy Y Ho Er Tm Yb Lu
(b) Group1 Gabbros
Rock/Chondrite
1000
100
10
1
0.1
La Ce Pr Nd Sm Eu Gd Tb Dy Ho Er Tm Yb Lu
(e) Group1 Gabbros
Rock/Primitive Mantle
1000
100
10
1
0.1
Th Nb Ta La Ce Pr Nd Zr Sm Eu Ti Gd Tb Dy Y Ho Er Tm Yb Lu
(c) Group2 Gabbros
Rock/Chondrite
1000
100
10
1
0.1
La Ce Pr Nd Sm Eu Gd Tb Dy Ho Er Tm Yb Lu
(f) Group2 Gabbros
Rock/Primitive Mantle
100
10
1
0.1
0
Th Nb Ta La Ce Pr Nd Zr Sm Eu Ti Gd Tb Dy Y Ho Er Tm Yb Lu

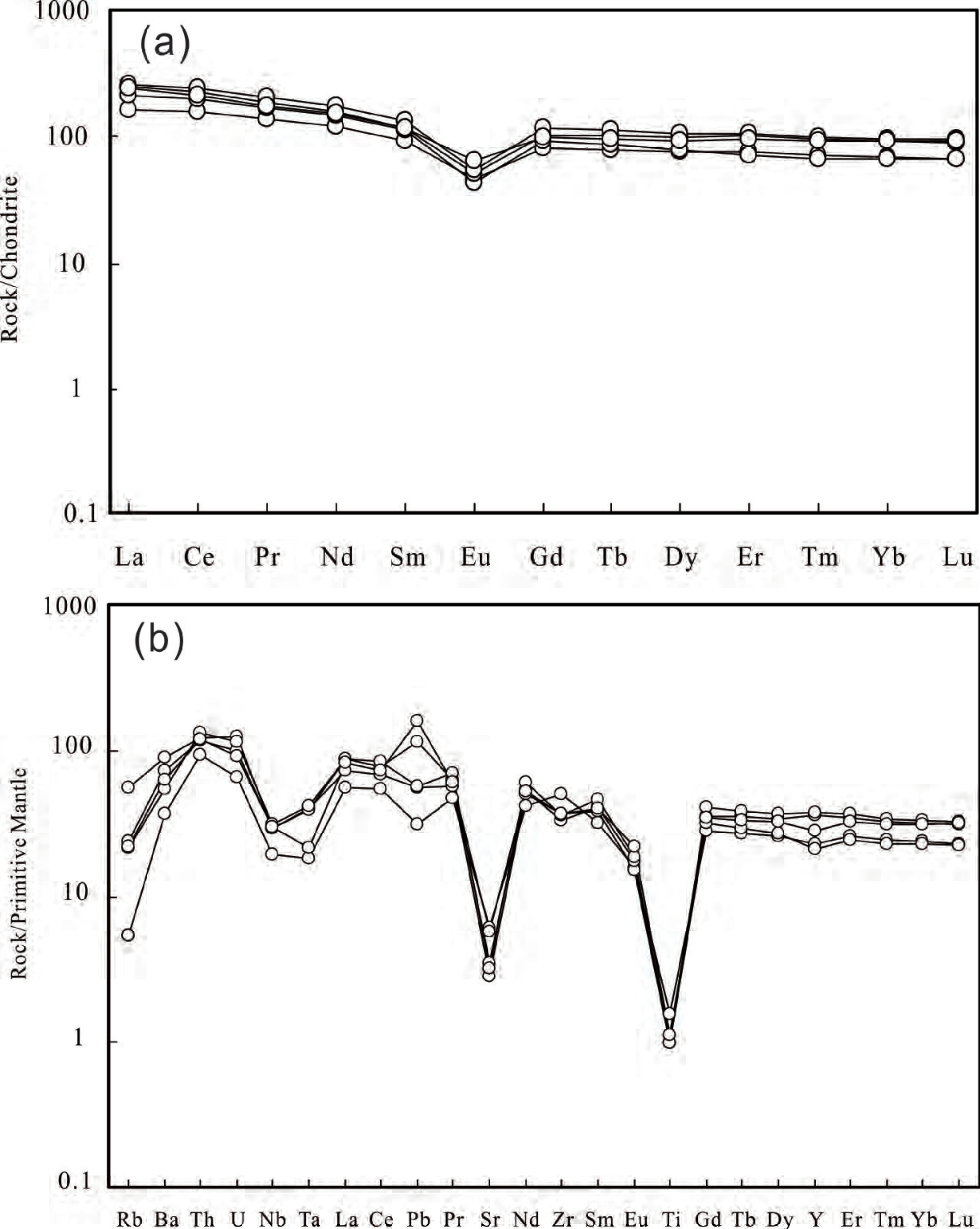
(a)
Rock/Chondrite
1000
100
10
1
0.1
La Ce Pr Nd Sm Eu Gd Tb Dy Er Tm Yb Lu
(b)
Rock/Primitive Mantle
1000
100
10
1
0.1
Rb Ba Th U Nb Ta La Ce Pb Pr Sr Nd Zr Sm Eu Ti Gd Tb Dy Y Er Tm Yb Lu

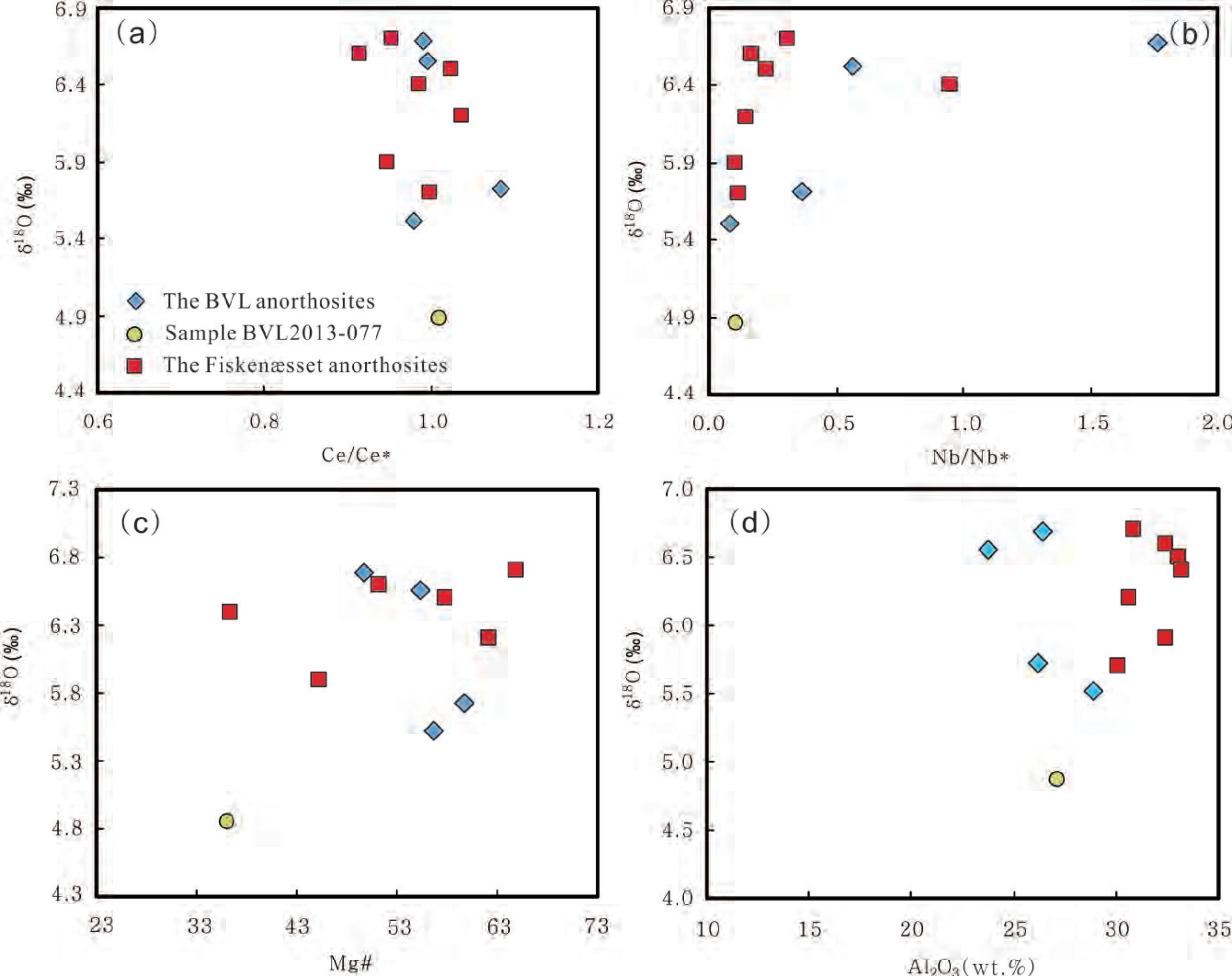

(a)
(b)
(c)
(d)
δ18O (‰)
Ce/Ce*
Nb/Nb*
Mg#
Al2O3 (wt.%)
The BVL anorthosites
Sample BVL2013-077
The Fiskenæsset anorthosites

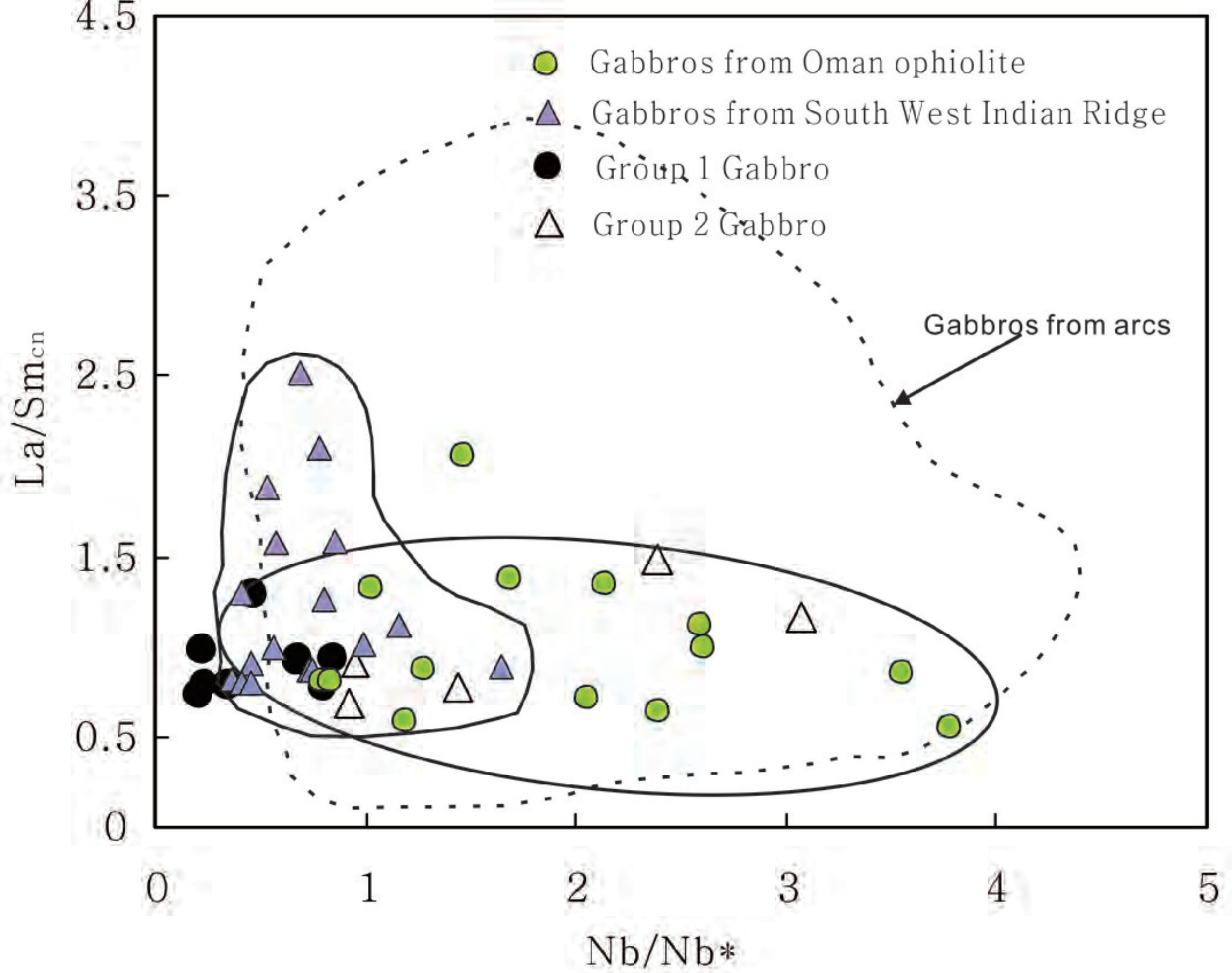
Gabbros from Oman ophiolite
Gabbros from South West Indian Ridge
Group 1 Gabbro
Group 2 Gabbro
Gabbros from arcs
La/Sm$_{cn}$
Nb/Nb*
0
0.5
1.5
2.5
3.5
4.5
0
1
2
3
4
5

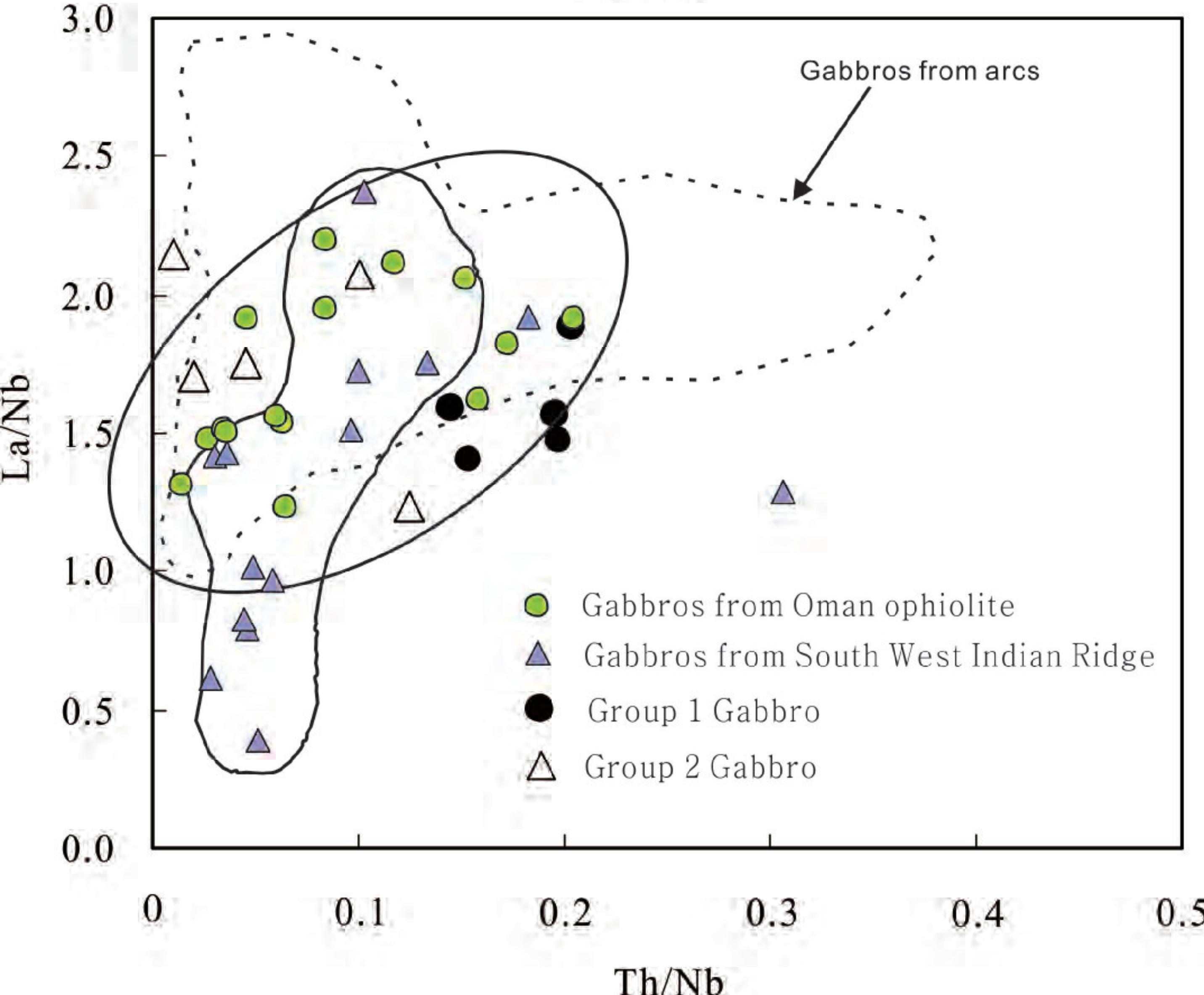
Gabbros from arcs
Gabbros from Oman ophiolite
Gabbros from South West Indian Ridge
Group 1 Gabbro
Group 2 Gabbro
La/Nb
Th/Nb
0.0
0.5
1.0
1.5
2.0
2.5
3.0
0
0.1
0.2
0.3
0.4
0.5

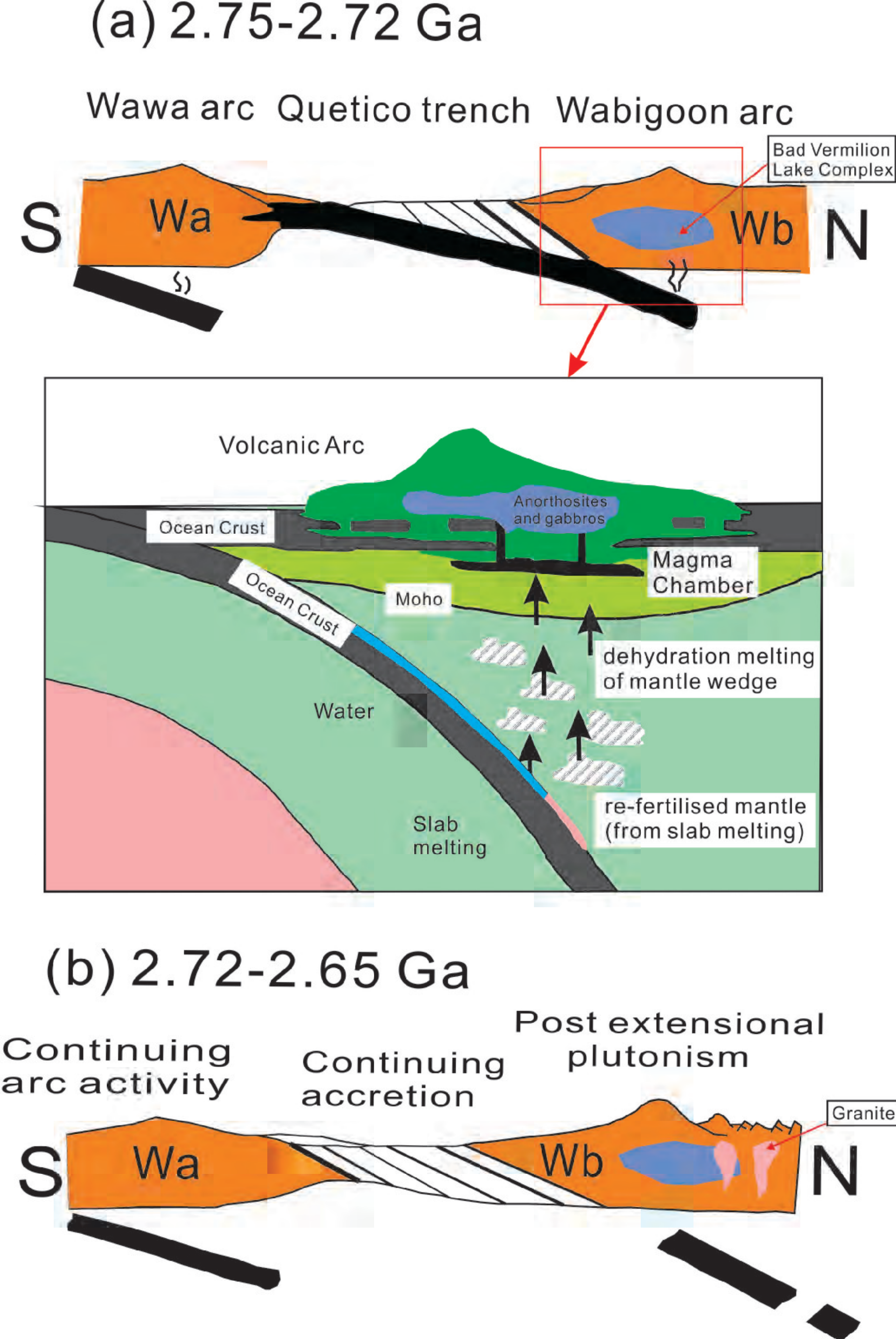
(a) 2.75-2.72 Ga
Wawa arc
Quetico trench
Wabigoon arc
Bad Vermilion Lake Complex
S
Wa
Wb
N
Volcanic Arc
Anorthosites and gabbros
Ocean Crust
Ocean Crust
Magma Chamber
Moho
dehydration melting of mantle wedge
Water
re-fertilised mantle (from slab melting)
Slab melting
(b) 2.72-2.65 Ga
Continuing arc activity
Continuing accretion
Post extensional plutonism
Granite
S
Wa
Wb
N

Table 1. Compilation of Archean anorthosite complexes in the Superior Province.

Name of the complex	Province	Metamorphic grade	Degree of deformation	References
Bird River	Manitoba	Medium	Medium	Trueman et al. (1971)
Pipestone Lake	Manitoba	Low to medium	Medium	Corkery et al. (1992)
Bad Vermilion Lake	Ontario	Low	Low to medium	Ashwal et al. (1983, 1985)
Shawmere	Ontario	High	Low to medium	Riccio (1981)
Doré Lake	Quebec	Low to medium	Low to medium	Mortensen (1993)
Big Trout Lake	Ontario	Medium	Medium	Thurston et al. (1980)
Bell River	Bell River	Low to medium	Low to medium	Ashwal et al. (1993)
Nelson River	Manitoba	Low to high	Low to high	Hubregtse (1980)

Table 2. Results of LA-ICP-MS zircon U-Pb isotope analyses.

Spots	Pb (ppm)	Th (ppm)	U (ppm)	Th/U	$^{207}Pb/^{235}U$	±1σ	$^{206}Pb/^{238}U$	±1σ	rho	$^{207}Pb/^{206}Pb$ age (Ma)	±1σ	$^{207}Pb/^{235}U$ age (Ma)	±1σ	$^{206}Pb/^{238}U$	±1σ
Sample BVL2013-042 N 515070 E 5393874															
BVL-042-1	377	145	210	0.69	13.8062	0.3189	0.5680	0.0050	0.381	2598	38.9	2737	21.9	2899	20.6
BVL-042-2	861	354	414	0.85	13.3359	0.3308	0.5463	0.0063	0.467	2602	38.3	2704	23.5	2810	26.4
BVL-042-3	202	94.8	131	0.72	12.2352	0.2923	0.5072	0.0049	0.401	2587	39.5	2623	22.5	2645	20.8
BVL-042-4	488	209	264	0.79	13.4026	0.3303	0.5379	0.0058	0.441	2646	40.9	2708	23.4	2774	24.6
BVL-042-5	152	65.0	101	0.65	13.0296	0.3659	0.5317	0.0065	0.435	2617	46.3	2682	26.5	2749	27.4
BVL-042-6	408	179	251	0.71	12.9952	0.3893	0.5116	0.0060	0.392	2676	49.4	2679	28.3	2663	25.6
BVL-042-7	377	157	222	0.71	13.6391	0.3924	0.5257	0.0062	0.413	2713	47.8	2725	27.3	2723	26.4
BVL-042-8	140	62.3	98.8	0.63	12.4680	0.3363	0.5055	0.0059	0.432	2626	75.0	2640	25.4	2637	25.3
BVL-042-9	701	344	390	0.88	12.8374	0.3066	0.5080	0.0050	0.411	2733	38.1	2668	22.6	2648	21.4
BVL-042-10	135	58.4	96.2	0.61	13.2886	0.3520	0.5302	0.0054	0.384	2655	41.4	2700	25.1	2742	22.8
BVL-042-11	367	151	218	0.69	13.2953	0.3729	0.5393	0.0056	0.372	2631	44.4	2701	26.6	2781	23.6
BVL-042-12	302	174	174	1.00	13.0945	0.4219	0.5287	0.0070	0.409	2643	49.7	2686	30.4	2736	29.5
BVL-042-13	163	69.6	110	0.63	13.4284	0.4310	0.5427	0.0066	0.381	2637	50.5	2710	30.4	2795	27.8
BVL-042-14	349	152	223	0.68	13.0484	0.4132	0.5352	0.0066	0.391	2614	51.1	2683	29.9	2764	27.9
BVL-042-15	482	190	251	0.76	13.7281	0.4073	0.5609	0.0063	0.380	2620	81.9	2731	28.1	2870	26.1
BVL-042-16	384	177	218	0.81	12.7447	0.4047	0.5173	0.0062	0.380	2631	53.2	2661	30.0	2688	26.6
BVL-042-17	226	101	139	0.73	12.5554	0.4208	0.5197	0.0054	0.310	2591	57.7	2647	31.6	2698	23.0
BVL-042-18	219	90	123	0.74	13.4885	0.5305	0.5545	0.0075	0.342	2606	68.5	2714	37.2	2844	30.9
BVL-042-19	117	52.5	86.6	0.61	12.1301	0.5664	0.5052	0.0082	0.347	2587	81.2	2615	43.8	2636	35.1
BVL-042-20	435	205	257	0.80	11.9157	0.4764	0.4952	0.0069	0.348	2581	68.8	2598	37.5	2593	29.7
BVL-042-21	64.4	27.7	59.1	0.47	11.6752	0.5492	0.4881	0.0099	0.433	2606	83.3	2579	44.0	2563	43.1
BVL-042-22	168	74.8	110	0.68	13.0848	0.4545	0.5390	0.0077	0.411	2611	59.6	2686	32.8	2779	32.3
BVL-042-23	418	176	252	0.70	14.0296	0.4068	0.5621	0.0057	0.348	2643	49.7	2752	27.5	2875	23.4
BVL-042-24	188	77.5	112	0.69	13.9299	0.4021	0.5628	0.0065	0.401	2632	48.9	2745	27.4	2878	26.9
BVL-042-25	501	220	281	0.78	14.3545	0.3495	0.5781	0.0055	0.392	2639	38.4	2773	23.2	2941	22.6
BVL-042-26	133	54	97	0.56	13.4542	0.2665	0.5214	0.0043	0.416	2709	32.3	2712	18.8	2705	18.3
BVL-042-27	143	57	102	0.56	13.7381	0.2699	0.5315	0.0050	0.480	2714	32.4	2732	18.7	2748	21.1
BVL-042-28	145	58	103	0.56	13.7136	0.2953	0.5373	0.0048	0.414	2700	38.7	2730	20.5	2772	20.1
Sample BVL2013-043 N 515030 E 5393907															
BVL-043-1	250	82	115	0.71	14.2339	0.3840	0.5372	0.0064	0.4434	2746	40.9	2765	25.7	2772	27.0
BVL-043-2	919	270	300	0.90	14.3993	0.4102	0.5505	0.0075	0.4784	2725	44.1	2776	27.1	2827	31.2
BVL-043-3	739	222	291	0.76	14.3648	0.3917	0.5510	0.0056	0.3748	2718	44.1	2774	26.0	2829	23.5
BVL-043-4	462	135	217	0.62	13.5215	0.4305	0.5269	0.0065	0.3877	2690	50.6	2717	30.2	2728	27.5
BVL-043-5	463	137	204	0.68	13.2846	0.4396	0.5253	0.0072	0.4118	2668	52.8	2700	31.3	2722	30.3
BVL-043-6	871	279	305	0.92	13.1754	0.4790	0.5200	0.0066	0.3497	2669	58.6	2692	34.4	2699	28.1
BVL-043-7	467	144	201	0.71	13.1314	0.4991	0.5200	0.0070	0.3557	2666	62.0	2689	35.9	2699	29.8
BVL-043-8	272	80	149	0.54	12.7262	0.4506	0.5164	0.0073	0.3966	2626	57.4	2660	33.4	2684	30.9
BVL-043-9	456	139	200	0.70	13.2897	0.4406	0.5293	0.0066	0.3746	2660	55.6	2700	31.4	2739	27.8
BVL-043-10	420	133	205	0.65	13.0482	0.4122	0.5225	0.0064	0.3894	2647	51.7	2683	29.8	2710	27.3
BVL-043-11	996	314	367	0.86	13.3231	0.4342	0.5255	0.0069	0.4046	2670	53.9	2703	30.8	2722	29.3
BVL-043-12	342	101	163	0.62	13.7824	0.5282	0.5415	0.0073	0.3537	2680	64.5	2735	36.3	2790	30.7
BVL-043-13	244	81	119	0.68	13.5523	0.4423	0.5296	0.0069	0.3985	2688	52.3	2719	30.9	2740	29.1

Table 2. Continued.

Spots	Pb (ppm)	Th (ppm)	U (ppm)	Th/U	$^{207}Pb/^{235}U$	±1σ	$^{206}Pb/^{238}U$	±1σ	rho	$^{207}Pb/^{206}Pb$ age (Ma)	±1σ	$^{207}Pb/^{235}U$ age (Ma)	±1σ	$^{206}Pb/^{238}U$	±1σ
BVL-043-14	628	200	265	0.75	13.8868	0.4133	0.5309	0.0071	0.4470	2728	48.1	2742	28.3	2745	29.8
BVL-043-15	164	44.4	79.3	0.56	14.5786	0.4410	0.5432	0.0082	0.4971	2777	50.5	2788	28.8	2797	34.2
BVL-043-16	551	174	236	0.74	13.5276	0.3702	0.5304	0.0068	0.4659	2700	44.4	2717	25.9	2743	28.5
BVL-043-17	928	294	352	0.83	14.0101	0.3519	0.5441	0.0051	0.3767	2702	40.7	2750	23.9	2800	21.5
BVL-043-18	853	269	345	0.78	14.0506	0.4150	0.5492	0.0063	0.3911	2690	46.9	2753	28.1	2822	26.4
BVL-043-19	405	112	171	0.65	14.6195	0.4457	0.5549	0.0072	0.4262	2739	42.4	2791	29.0	2846	29.9
BVL-043-20	829	269	331	0.81	13.8184	0.3870	0.5332	0.0059	0.3925	2706	44.4	2737	26.6	2755	24.7
BVL-043-21	634	194	237	0.82	14.5680	0.4236	0.5424	0.0066	0.4187	2769	47.8	2787	27.7	2794	27.6
BVL-043-22	823	259	282	0.92	14.3937	0.4717	0.5448	0.0061	0.3425	2733	53.1	2776	31.2	2804	25.6
BVL-043-23	736	234	274	0.86	14.7188	0.5357	0.5581	0.0065	0.3179	2732	60.8	2797	34.7	2859	26.8
BVL-043-24	222	62.7	103	0.61	14.3688	0.6422	0.5444	0.0083	0.3395	2732	74.1	2774	42.5	2802	34.5
BVL-043-25	586	174	236	0.74	14.6769	0.6159	0.5535	0.0069	0.2981	2743	70.7	2795	39.9	2840	28.8
BVL-043-26	529	157	208	0.76	14.9248	0.5797	0.5588	0.0072	0.3311	2750	63.6	2810	37.0	2862	29.8
BVL-043-27	483	135	208	0.65	14.9272	0.5547	0.5549	0.0072	0.3472	2761	60.5	2811	35.4	2846	29.7
BVL-043-28	166	47.3	71.9	0.66	15.4103	0.5330	0.5627	0.0072	0.3681	2796	56.5	2841	33.0	2878	29.6
BVL-043-29	247	66.0	113	0.58	14.6247	0.7375	0.5433	0.0078	0.2849	2756	75.8	2791	48.0	2797	32.6
BVL-043-30	132	36.9	68.7	0.54	14.5026	0.4931	0.5425	0.0087	0.4719	2766	55.9	2783	32.4	2794	36.4
BVL-043-31	203	58.6	94.3	0.62	14.7632	0.4415	0.5608	0.0069	0.4132	2739	50.2	2800	28.5	2870	28.7
BVL-043-32	557	174	236	0.74	14.1794	0.3927	0.5370	0.0059	0.3947	2740	45.4	2762	26.3	2771	24.7

Table 3. Major (wt.%) and trace (ppm) element concentrations and significant element ratios for the BVLA Complex anorthosites and leucoga

Sample#	BVL2013-047 (a)	BVL2013-048	BVL2013-049	BVL2013-053	BVL2013-054	BVL2013-055	BVL2013-064	BVL2013-066(a)
SiO_2	43.0	44.2	43.8	46.7	46.5	46.7	46.0	44.3
TiO_2	0.34	0.28	0.92	0.18	0.15	0.17	0.20	0.21
Al_2O_3	20.8	23.7	25.8	26.8	28.2	27.5	26.1	26.5
Fe_2O_3(T)	6.6	9.0	8.1	3.7	2.6	3.3	5.2	6.8
MnO	0.103	0.093	0.076	0.048	0.041	0.053	0.078	0.072
MgO	4.0	5.6	3.3	2.5	1.1	1.6	3.9	6.0
CaO	13.5	10.0	9.2	12.8	15.8	14.7	12.4	8.8
K_2O	0.06	0.03	1.2	0.24	0.33	0.14	0.21	1.12
Na_2O	2.77	1.12	3.01	2.61	2.02	2.51	3.05	2.5
P_2O_5	0.03	0.03	0.02	0.02	0.01	0.03	< 0.01	< 0.01
LOI	7.4	4.6	3.3	3.6	3.0	3.3	3.3	4.6
Mg-number	54.6	55.3	44.5	57.6	45.9	49.1	59.6	63.9
Cr	61	115	92	222	18	33	271	33
Co	22	48	30	14	10	11	13	23
Ni	78	154	76	36	24	33	80	116
Rb	1.02	0.76	31.13	7.74	9.71	4.30	5.09	0.69
Sr	144	113	206	141	197	171	124	87
Ba	25	18	287	55	63	34	29	71
Sc	17	7	31	20	5	8	17	29
V	116	69	331	85	42	52	80	95
Ta	0.04	0.02	0.02	0.02	0.04	0.02	0.02	0.22
Nb	0.52	0.28	0.32	0.32	0.52	0.37	0.35	3.31
Zr	11	8	8	8	13	10	10	8
Th	0.23	0.08	0.05	0.05	0.46	0.22	0.33	2.16
U	0.05	0.02	0.01	0.04	0.08	0.04	0.04	0.61
Y	6	2	4	4	4	3	7	7
La	1.56	1.01	0.95	0.83	2.02	1.40	1.36	5.21
Ce	3.60	2.27	2.29	2.00	4.54	3.21	4.71	13.46
Pr	0.48	0.31	0.34	0.27	0.56	0.43	0.84	1.87
Nd	2.18	1.35	1.76	1.33	2.28	1.95	4.37	9.03
Sm	0.59	0.37	0.59	0.41	0.53	0.51	1.29	2.89
Eu	0.45	0.34	0.41	0.30	0.45	0.41	0.37	0.95
Gd	0.83	0.42	0.89	0.60	0.62	0.59	1.44	4.03
Tb	0.14	0.07	0.14	0.10	0.09	0.09	0.23	0.76
Dy	0.99	0.49	0.94	0.68	0.58	0.58	1.35	5.29
Ho	0.23	0.10	0.20	0.14	0.12	0.11	0.26	1.18
Er	0.69	0.31	0.55	0.42	0.35	0.32	0.74	3.58
Tm	0.10	0.04	0.08	0.06	0.05	0.05	0.09	0.53
Yb	0.74	0.30	0.48	0.38	0.31	0.27	0.59	3.60
Lu	0.12	0.05	0.07	0.05	0.04	0.04	0.08	0.55
Cu	11.09	112.18	12.69	23.94	29.74	16.49	12.52	72.20
Zn	71	165	173	61	48	48	113	160
Ga	47	51	92	60	68	60	52	59
Pb	2.50	0.34	2.29	4.70	9.76	5.59	9.00	6.98
La/Sm_{cn}	1.72	1.75	1.04	1.30	2.46	1.76	0.68	1.16
La/Yb_{cn}	1.51	2.40	1.42	1.57	4.69	3.67	1.66	1.04
Gd/Yb_{cn}	0.92	1.15	1.54	1.30	1.67	1.80	2.02	0.93
Eu/Eu*	1.97	2.60	1.71	1.87	2.38	2.25	0.84	0.85
Ce/Ce*	1.02	1.00	0.98	1.03	1.05	1.01	1.08	1.06
Al_2O_3/TiO_2	62	85	28	149	188	163	133	125
Y/Ho	26.3	19.9	20.4	28.1	34.0	26.1	26.9	5.9
Nb/Ta	12.1	13.2	16.5	14.1	16.5	18.0	14.9	13.7
Zr/Y	1.83	4.00	2.00	2.00	3.25	3.33	1.43	1.14
Ti/Zr	183	208	692	135	69	101	117	159
Nb/Nb*	0.43	0.54	0.78	0.88	0.33	0.44	0.36	0.40
Zr/Zr*	0.67	0.78	0.54	0.75	0.82	0.69	0.29	0.11
Ti/Ti*	1.01	1.35	2.81	0.77	0.52	0.63	0.49	0.20
Sr/Y	24	56	52	35	49	57	18	12
North	517336	517336	517280	518811	518736	518911	526661	526511
East	5393713	5393713	5393561	5393580	5393410	5393607	5399551	5399464

(a): Variably altered sample.

Table 3. Continued.

Sample#	BVL2013-068	BVL2013-069	BVL2013-070	BVL2013-072	BVL2013-074	BVL2013-076	BVL2013-077	BVL2013-079
SiO_2	47.0	46.8	45.1	46.9	47.1	44.4	44.1	45.8
TiO_2	0.29	0.17	0.16	0.19	0.26	0.14	0.18	0.77
Al_2O_3	28.2	27.4	28.8	26.4	28.0	26.1	27.1	25.8
Fe_2O_3(T)	3.2	3.1	5.0	5.3	2.7	6.8	6.3	6.4
MnO	0.075	0.06	0.064	0.06	0.059	0.076	0.052	0.062
MgO	1.5	2.1	3.3	2.6	0.7	3.6	1.8	3.1
CaO	13.6	17.1	12.0	13.5	15.8	11.5	12.9	13.0
K_2O	0.56	0.03	0.79	0.39	0.12	0.63	1.02	0.08
Na_2O	3.24	1.37	2.57	2.47	3.46	3.06	2.5	2.94
P_2O_5	0.02	0.01	< 0.01	0.02	0.04	< 0.01	0.02	0.02
LOI	3.0	2.9	3.0	2.8	2.0	3.5	2.6	2.8
Mg-number	47.2	56.8	56.5	49.6	34.9	50.9	36.0	48.8
Cr	19	307	518	104	9	15	37	32
Co	10	12	19	11	6	23	16	22
Ni	34	40	45	41	28	72	39	83
Rb	13.13	0.77	17.89	9.99	2.70	15.67	26.65	2.35
Sr	176	171	138	141	218	146	149	185
Ba	91	4	102	54	21	96	90	17
Sc	7	16	20	18	6	6	10	17
V	67	71	81	84	56	49	119	59
Ta	0.05	0.01	0.01	0.02	0.04	0.01	0.02	0.08
Nb	0.66	0.26	0.30	0.31	0.59	0.29	0.42	1.21
Zr	18	5	6	13	16	6	10	24
Th	0.05	4.00	7.05	0.01	3.61	0.11	3.18	2.83
U	0.05	0.04	0.07	0.06	0.08	0.03	0.82	0.10
Y	5	4	4	7	4	2	10	6
La	1.13	0.59	1.10	2.23	1.13	0.44	4.73	3.73
Ce	2.57	1.48	2.33	4.94	2.93	0.97	9.83	8.55
Pr	0.34	0.21	0.31	0.67	0.41	0.13	1.21	1.16
Nd	1.50	1.06	1.44	2.97	1.87	0.60	4.91	4.88
Sm	0.43	0.36	0.43	0.79	0.49	0.20	1.15	1.00
Eu	0.39	0.26	0.74	0.51	0.38	0.31	0.99	0.71
Gd	0.79	0.49	0.59	1.00	0.56	0.31	1.31	1.02
Tb	0.10	0.08	0.10	0.17	0.10	0.05	0.21	0.16
Dy	0.59	0.55	0.63	1.12	0.61	0.37	1.44	0.98
Ho	0.13	0.12	0.14	0.24	0.13	0.08	0.30	0.20
Er	0.39	0.36	0.38	0.72	0.37	0.24	0.86	0.60
Tm	0.06	0.05	0.05	0.10	0.06	0.03	0.11	0.08
Yb	0.39	0.32	0.33	0.66	0.36	0.25	0.72	0.53
Lu	0.06	0.05	0.05	0.09	0.05	0.04	0.10	0.08
Cu	143.99	11.34	21.82	84.84	19.57	5.30	37.12	81.33
Zn	102	176	58	59	38	57	50	61
Ga	68	52	66	57	58	64	75	55
Pb	8.86	22.14	5.55	1.74	7.03	5.07	4.33	7.47
La/Sm_{cn}	1.68	1.07	1.64	1.82	1.51	1.42	2.66	2.40
La/Yb_{cn}	2.09	1.31	2.36	2.44	2.23	1.28	4.68	5.00
Gd/Yb_{cn}	1.68	1.25	1.46	1.26	1.28	1.04	1.50	1.57
Eu/Eu*	2.03	1.92	4.49	1.74	2.22	3.76	2.47	2.16
Ce/Ce*	1.02	1.02	0.98	0.99	1.05	0.99	1.01	1.01
Al_2O_3/TiO_2	99	162	182	139	107	193	155	33
Y/Ho	37.7	33.0	29.6	29.3	31.8	25.5	33.4	29.9
Nb/Ta	22.0	20.6	14.5	16.0	21.1	20.4	15.9	19.3
Zr/Y	3.60	1.25	1.50	1.86	4.00	3.00	1.00	4.00
Ti/Zr	95	203	158	87	98	135	105	193
Nb/Nb*	1.10	0.10	0.08	1.76	0.13	0.63	0.14	0.22
Zr/Zr*	1.54	0.56	0.53	0.59	1.16	1.20	0.29	0.75
Ti/Ti*	0.95	0.86	0.44	0.49	1.04	0.81	0.28	1.66
Sr/Y	35	43	34	20	55	73	15	31
North	525876	525458	525185	525362	525964	525806	525564	525727
East	5399371	5398806	5398429	5398224	5398182	5397291	5396817	5396582

Table 3. Continued.

Sample#	BVL2013-080	BVL2013-081
SiO_2	49.7	48.4
TiO_2	0.20	0.46
Al_2O_3	24.6	20.4
Fe_2O_3(T)	3.3	10.4
MnO	0.081	0.107
MgO	1.3	3.8
CaO	17.4	9.6
K_2O	0.02	0.27
Na_2O	0.19	2.31
P_2O_5	0.02	0.02
LOI	2.8	4.1
Mg-number	42.7	42.0
Cr	350	64
Co	9	39
Ni	36	74
Rb	0.92	5.61
Sr	191	211
Ba	6	78
Sc	21	14
V	81	174
Ta	0.01	0.16
Nb	0.26	2.01
Zr	9	51
Th	0.15	1.70
U	0.01	0.18
Y	5	8
La	0.80	6.51
Ce	1.87	14.25
Pr	0.27	1.71
Nd	1.34	6.66
Sm	0.43	1.49
Eu	0.36	0.68
Gd	0.58	1.58
Tb	0.11	0.26
Dy	0.71	1.54
Ho	0.16	0.32
Er	0.46	0.94
Tm	0.06	0.14
Yb	0.43	0.85
Lu	0.06	0.13
Cu	8.92	1.61
Zn	71	95
Ga	52	64
Pb	3.92	2.12
La/Sm_{cn}	1.19	2.82
La/Yb_{cn}	1.31	5.48
Gd/Yb_{cn}	1.11	1.54
Eu/Eu*	2.21	1.35
Ce/Ce*	0.99	1.05
Al_2O_3/TiO_2	126	45
Y/Ho	32.1	24.7
Nb/Ta	12.8	
Zr/Y	1.80	6.38
Ti/Zr	131	53
Nb/Nb*	0.48	0.32
Zr/Zr*	0.82	1.12
Ti/Ti*	0.78	0.81
Sr/Y	38	26
North	520364	519469
East	5396381	5395238

Table 4. Major (wt.%) and trace (ppm) element concentrations and significant element ratios for the gabbros in the BVLA Complex.

	Group 1								
Sample#	BVL2013-050	BVL2013-052	BVL2013-063[d]	BVL2013-065[d]	BVL2013-067[d]	BVL2013-071[d]	BVL2013-073[d]	BVL2013-075	BVL2013-078[d]
SiO_2	41.4	47.4	48.0	51.5	46.6	48.4	48.5	49.2	49.6
TiO_2	1.128	1.52	1.40	1.574	1.042	0.98	1.37	1.329	1.031
Al_2O_3	11.3	15.1	15.1	13.6	15.8	15.4	14.3	14.7	14.3
Fe_2O_3(T)	16.4	15.3	13.5	13.7	15.0	12.0	15.7	14.7	13.5
MnO	0.238	0.19	0.21	0.193	0.228	0.22	0.29	0.205	0.168
MgO	5.5	6.8	6.8	4.7	7.4	7.2	6.0	6.1	6.6
CaO	15.1	9.0	10.6	8.9	7.3	11.1	7.5	8.5	11.0
K_2O	0.09	0.06	0.04	< 0.01	0.03	0.02	0.12	0.12	0.22
Na_2O	0.61	1.77	1.75	0.05	2.57	0.91	3.63	3.17	2
P_2O_5	2.65	0.11	0.11	0.13	0.09	0.09	0.11	0.11	0.08
LOI	4.2	3.6	3.0	5.6	3.4	3.4	2.2	2.2	1.6
Mg-number	39.9	46.6	50.1	40.5	49.4	54.4	43.1	45.2	49.2
Cr	11	161	201	435	176	274	167	110	113
Co	42	66	44	15	43	46	43	46	43
Ni	99	168	167	99	120	177	165	147	113
Rb	1.15	1.28	0.43	23.90	1.05	0.16	2.47	2.03	3.93
Sr	181	157	129	101	53	96	52	75	76
Ba	13	16.00	8.00	2	5	3.00	20.00	18	27
Sc	45	32.00	34.00	38	48	39.00	41.00	42	40
V	166	332.00	331.00	366	324	293.00	360.00	364	298
Ta	0.05	0.13	0.19	0.02	0.09	0.09	0.11	0.11	0.13
Nb	1.01	2.80	2.61	0.31	1.59	1.30	1.65	1.98	1.81
Zr	30	76.00	70.00	104	49	55.00	75.00	74	56
Th	0.60	0.55	0.38	0.31	4.52	0.27	3.09	4.18	0.36
U	0.18	0.49	0.09	0.06	0.07	0.06	0.14	0.11	0.12
Y	41	18.00	18.00	30	22	19.00	27.00	27	21
La	13.85	4.36	4.13	1.46	2.29	2.45	2.74	3.37	2.66
Ce	35.36	11.89	11.44	4.38	6.55	7.08	8.23	9.43	6.99
Pr	5.12	1.85	1.79	0.73	1.06	1.13	1.32	1.52	1.06
Nd	25.51	9.45	9.07	3.51	5.59	6.01	6.93	8.08	5.40
Sm	6.94	2.90	2.81	1.01	2.02	2.04	2.27	2.79	1.85
Eu	1.72	1.03	0.99	0.39	0.66	0.75	0.75	0.77	0.61
Gd	8.69	3.52	3.48	1.27	2.87	3.00	3.14	3.76	2.80
Tb	1.29	0.57	0.58	0.22	0.54	0.51	0.56	0.67	0.52
Dy	7.53	3.45	3.60	1.37	3.66	3.45	3.78	4.48	3.53
Ho	1.50	0.68	0.73	0.27	0.80	0.75	0.83	0.97	0.76
Er	4.01	1.90	2.09	0.79	2.42	2.23	2.47	2.90	2.28
Tm	0.49	0.26	0.29	0.10	0.35	0.32	0.37	0.42	0.32
Yb	2.85	1.53	1.78	0.64	2.23	2.10	2.44	2.75	2.18
Lu	0.41	0.22	0.25	0.09	0.32	0.32	0.38	0.42	0.32
Cu	74	71	119	9	76	124	86	195	14
Zn	182	130	140	98	233	97	485	86	75
Ga	53	59	57	52	43	50	56	53	51
La/Sm_{cn}	1.29	0.95	0.77	0.78	0.73	0.94	0.97	0.78	0.93
La/Yb_{cn}	3.49	1.66	0.84	0.81	0.74	1.63	2.05	0.88	0.88
Gd/Yb_{cn}	2.52	1.62	1.18	1.07	1.07	1.64	1.91	1.13	1.07
Eu/Eu*	0.68	0.96	0.93	0.86	0.84	1.06	0.98	0.73	0.83
Ce/Ce*	1.03	1.03	1.03	1.04	1.03	1.04	1.06	1.02	1.02
Al_2O_3/TiO_2	10	10	11	9	15	16	10	11	14
Y/Ho	27	27	25	109	27	25	33	28	27
Nb/Ta	19.3	21.1	13.9	17.8	17.9	13.8	14.4	17.5	13.6
Zr/Y	0.7	4.2	3.9	3.5	2.2	2.9	2.8	2.7	2.7
Ti/Zr	225	119	120	91	127	107	110	108	110
Nb/Nb*	0.47	0.86	0.81	0.35	0.21	0.68	0.23	0.24	0.69
Zr/Zr*	0.16	1.01	0.96	3.83	1.01	1.09	1.31	1.08	1.23
Ti/Ti*	0.54	1.46	1.39	4.09	1.38	1.20	1.64	1.43	1.44
North	517267	517203	526998	526511	525947	525128	525964	525852	525727
East	5393651	5393059	5399549	5399464	5399438	5398149	5398182	5397852	5396582

d: Microgabbro occurring as dykes

	Group 2				
Sample#	BVL2013-083	BVL2013-084	BVL2013-085[d]	BVL2013-086	BVL2013-087
SiO_2	43.6	42.4	41.0	44.6	47.0
TiO_2	0.899	0.76	0.487	0.976	0.568
Al_2O_3	22.6	15.6	16.7	17.2	18.1
Fe_2O_3(T)	11.4	15.6	16.4	14.2	13.4
MnO	0.123	0.21	0.201	0.194	0.178
MgO	4.7	8.3	6.9	7.3	6.6
CaO	11.9	12.5	9.1	8.9	9.0
K_2O	0.16	0.04	0.02	0.02	0.02
Na_2O	1.19	0.47	1.04	0.84	1.65
P_2O_5	0.02	0.03	0.01	0.02	0.02
LOI	4.2	3.5	8.3	4.8	4.0
Mg-number	45.1	51.3	45.4	50.4	49.4
Cr	192	234	90	394	197
Co	43	56	54	45	48
Ni	83	137	137	147	109
Rb	3.51	0.42	0.36	0.25	0.29
Sr	192	187	157	234	204
Ba	46	8	7	8	12
Sc	39	41	21	39	25
V	370	284	192	329	200
Ta	0.04	0.02	0.02	0.03	0.03
Nb	0.66	0.27	0.30	0.43	0.47
Zr	8	5	5	7	6
Th	0.08	0.03	0.00	0.02	0.01
U	0.01	0.01	0.01	0.01	0.01
Y	4	4	2	5	3
La	0.81	0.55	0.65	0.75	0.79
Ce	2.03	1.47	1.52	1.96	1.80
Pr	0.31	0.24	0.22	0.30	0.25
Nd	1.64	1.32	1.10	1.63	1.12
Sm	0.57	0.52	0.36	0.63	0.35
Eu	0.47	0.45	0.48	0.55	0.44
Gd	0.89	0.91	0.54	1.04	0.53
Tb	0.15	0.14	0.09	0.17	0.09
Dy	1.00	0.94	0.60	1.10	0.65
Ho	0.21	0.19	0.12	0.24	0.15
Er	0.59	0.55	0.39	0.73	0.47
Tm	0.08	0.08	0.05	0.10	0.07
Yb	0.56	0.52	0.36	0.70	0.52
Lu	0.08	0.08	0.06	0.11	0.09
Cu	2	5	2	3	2
Zn	109	200	142	128	111
Ga	58	43	46	50	47
La/Sm_{cn}	0.91	0.68	1.15	0.77	1.47
La/Yb_{cn}	1.04	0.76	1.29	0.77	1.09
Gd/Yb_{cn}	1.32	1.44	1.25	1.23	0.84
Eu/Eu*	2.03	2.01	3.33	2.08	3.18
Ce/Ce*	1.00	1.00	0.99	1.01	1.00
Al_2O_3/TiO_2	25	20	34	18	32
Y/Ho	19.4	21.1	16.1	20.8	19.9
Nb/Ta	17.0	12.8	14.3	14.3	16.9
Zr/Y	2.0	1.3	2.5	1.4	2.0
Ti/Zr	674	911	584	836	567
Nb/Nb*	0.96	0.93	3.08	1.45	2.40
Zr/Zr*	0.57	0.42	0.55	0.48	0.67
Ti/Ti*	2.55	2.18	1.75	2.37	2.15
North	518919	519343	519570	519770	519770
East	5395033	5395783	5396053	5396183	5396183

Table 5. Major (wt.%) and trace (ppm) element concentrations and significant element ratios for the Bad Vermilion Lake granitic rocks

Sample#	BVL2013-041	BVL2013-042	BVL2013-043	BVL2013-044	BVL2013-045
SiO_2	75.6	76.5	77.3	77.1	77.8
TiO_2	0.27	0.17	0.17	0.17	0.19
Al_2O_3	11.1	11.5	11.6	11.6	10.8
Fe_2O_3(T)	5.57	1.98	2.50	1.65	2.51
MnO	0.02	0.04	0.04	0.04	0.06
MgO	0.15	0.06	0.07	0.03	0.09
CaO	1.84	1.95	1.69	1.96	2.51
K_2O	0.26	1.04	2.13	0.72	0.75
Na_2O	5.11	4.91	2.75	5.10	4.62
P_2O_5	0.02	0.01	0.02	0.02	0.04
LOI	0.53	1.97	1.99	1.85	1.61
Mg-number	5.1	5.7	5.3	3.5	6.6
Cr	b.d	12.08	b.d	b.d	17.44
Co	1.53	0.66	0.63	0.43	0.58
Ni	14	10	10	9	8
Rb	3	15	35	14	14
Sr	128	59	73	66	120
Ba	257	505	622	381	438
Sc	2.00	1.00	1.00	< 1	2.00
V	0.30	1.06	0.67	-0.20	0.77
Ta	0.74	1.62	1.59	1.68	0.86
Nb	13.7	20.5	20.5	22.0	21.2
Zr	558	411	367	404	407
Th	7.94	9.90	10.38	11.10	10.09
U	1.36	2.06	2.58	2.40	1.90
Y	102	95	163	168	127
La	37.9	49.9	59.5	60.1	56.6
Ce	95.8	120.7	137.7	147.0	129.1
Pr	12.9	15.5	17.3	19.0	16.5
Nd	55.7	67.0	72.3	81.0	70.7
Sm	14.1	16.9	17.9	20.3	17.6
Eu	2.61	2.50	2.92	3.10	3.65
Gd	16.51	18.81	20.95	24.02	20.24
Tb	2.86	3.16	3.75	4.12	3.54
Dy	18.81	19.53	24.95	26.91	23.55
Ho	4.04		5.38	5.74	5.07
Er	12.40	11.67	16.54	17.37	15.49
Tm	1.79	1.68	2.39	2.48	2.30
Yb	11.53	11.11	15.49	16.19	15.35
Lu	1.66	1.65	2.27	2.37	2.35
Cu	14	8	6	4	22
Zn	133	67	57	48	79
Ga	102	141	158	131	132
Pb	2.21	3.93	8.07	3.99	11.34
Na_2O+K_2O	5.37	5.95	4.88	5.82	5.37
A/CNK	0.92	0.90	1.17	0.91	0.83
La/Sm_{cn}	1.74	1.91	2.15	1.91	2.07
La/Yb_{cn}	2.36	3.22	2.75	2.66	2.64
Gd/Yb_{cn}	1.18	1.40	1.12	1.23	1.09
Eu/Eu*	0.52	0.43	0.46	0.43	0.59
Ce/Ce*	1.06	1.06	1.05	1.07	1.04
Sr/Y	0.01	0.01	0.01	0.00	0.01
Nb/Nb*	0.47	0.42	0.42	0.42	0.59
Sr/Sr*	0.14	0.05	0.06	0.05	0.10
Ti/Ti*	0.07	0.05	0.04	0.04	0.04
North	514938	515070	515030	515342	515665
East	5393961	5393874	5393907	5393642	5393685

b.d.: Below detection limit

Table 6. Oxygen isotope compositions of the Bad Vermilion Lake Anorthosite.

Sample #	Whole rock $\delta^{18}O$ (‰ VSMOW)	Fresh plagioclase $\delta^{18}O$ (‰ VSMOW)	Altered plagioclase $\delta^{18}O$ (‰ VSMOW)
BVL2013-048	+6.6	+6.7	+6.0
BVL2013-064	+5.7	+6.4	+5.3
BVL2013-070	+5.5	+6.7	+6.0
BVL2013-072	+6.7	**+5.7**	+5.7
BVL2013-077	+4.9	+4.8	+5.8
BVL2013-054		+7.2	
BVL2013-068		+6.5	
BVL2013-074		+5.8	
BVL2013-076		+6.6	
BVL2013-079		**+7.0**	
Average	+5.9±0.8	+6.3±0.7	+5.8±0.3
Average without BVL2013-077	+6.1±0.6	+6.5±0.5	+5.8±0.3

*Values in bold are the average of replicate analyses

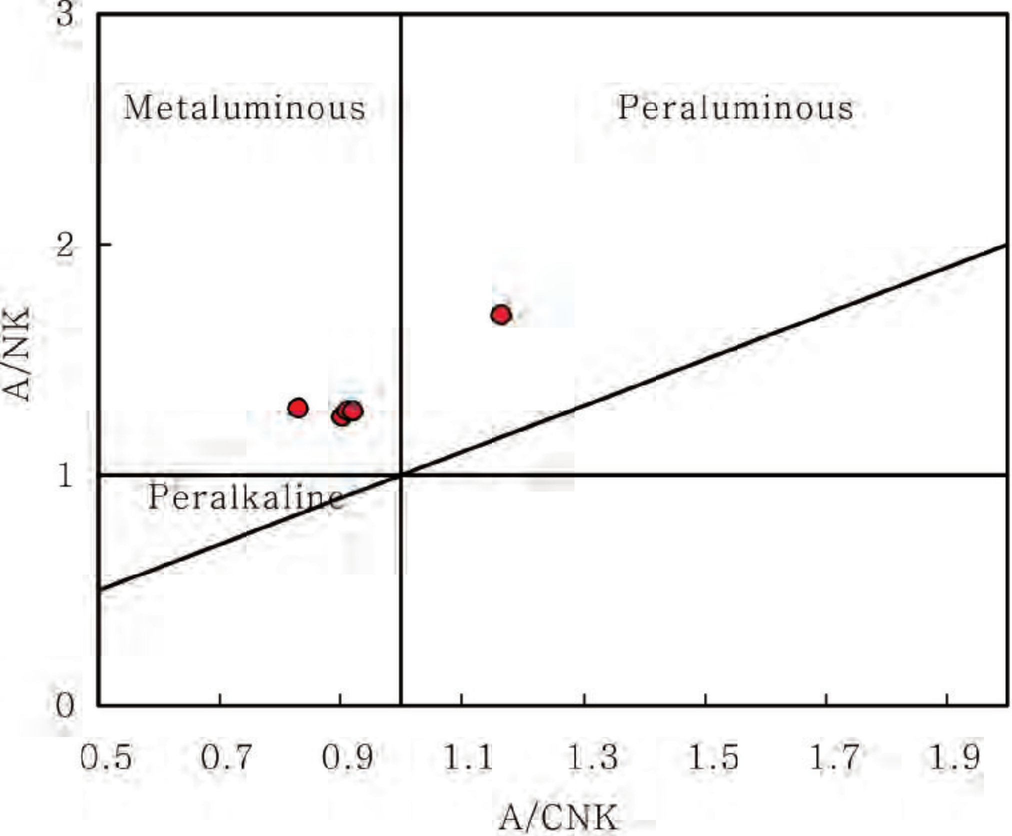

Supplementary Fig. 1. A/NK versus A/CNK diagram for the Bad Vermilion Lake granitic rocks indicating a metaluminous to peraluminous composition. A/NK = Al/(Na + K) (molar ratio). A/CNK = Al/(Ca + Na + K) (molar ratio).

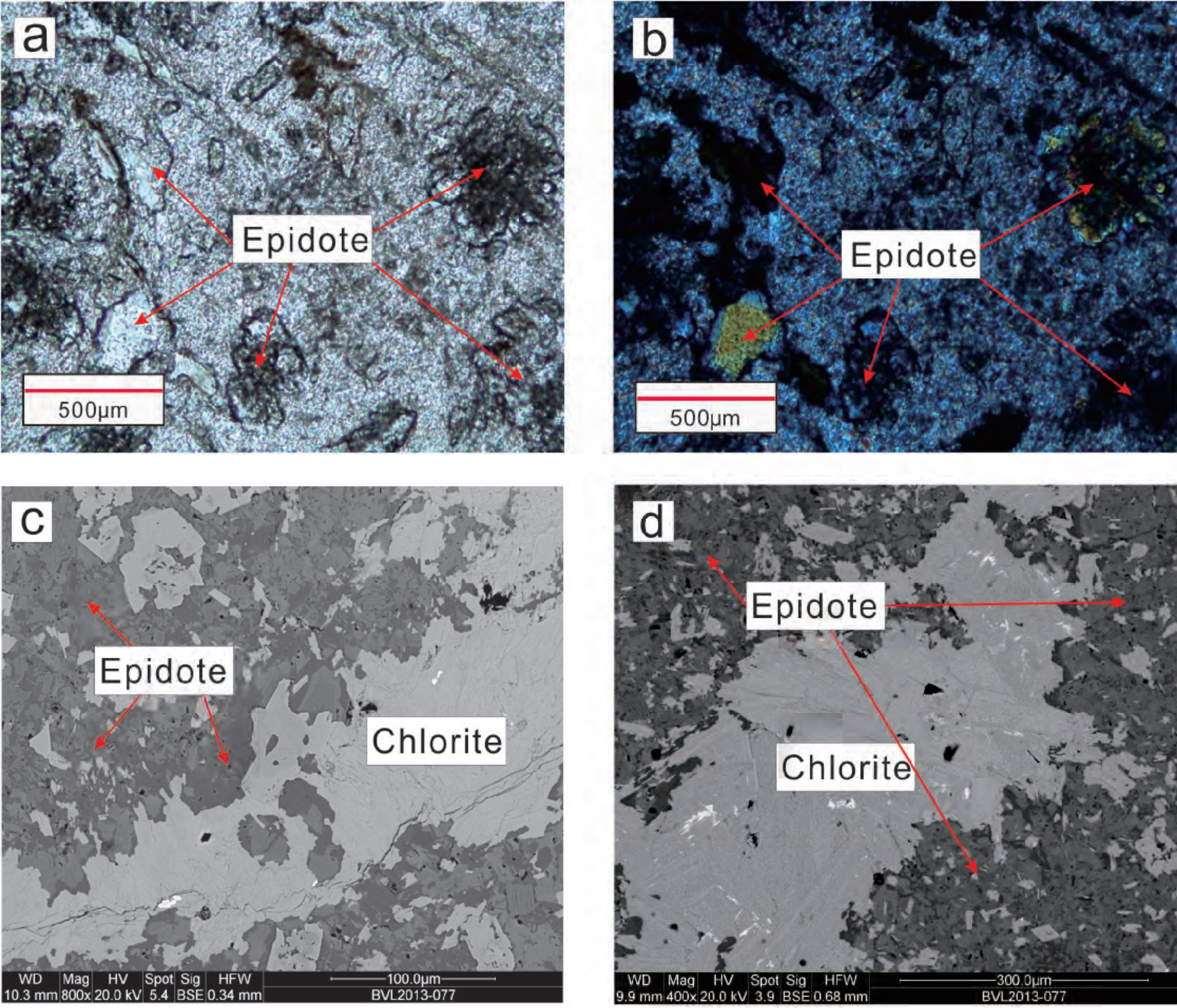

Supplementary Fig. 2. Photomicrographs illustrating petrographic characteristics of sample BVL2013-077 showing it underwent strong epidotization.

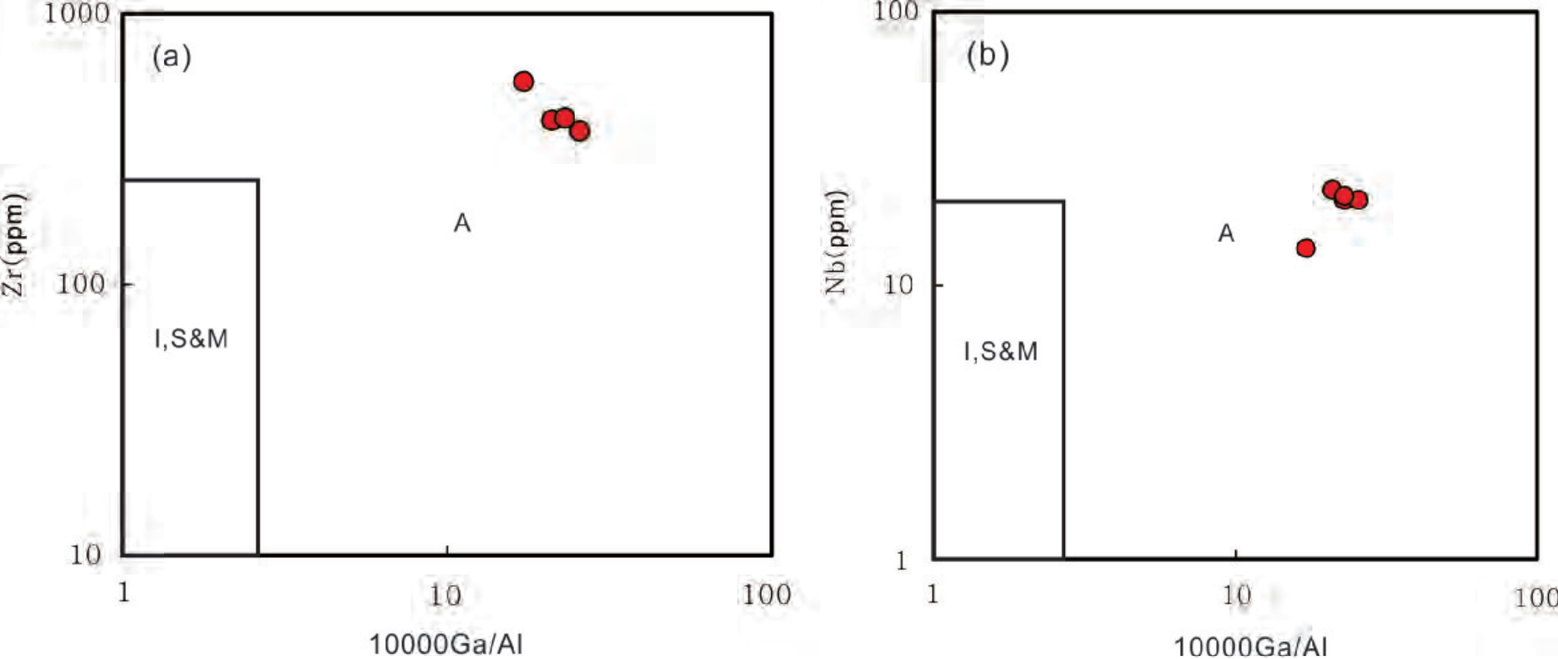

Supplementary Fig. 3. (a) Zr vs. 10000 Ga/Al, (b) Nb vs. 10000 Ga/Al classification diagrams for granites (after Whalen et al., 1987). I, S, M & A represent I-, S-, M-, and A-type granites.

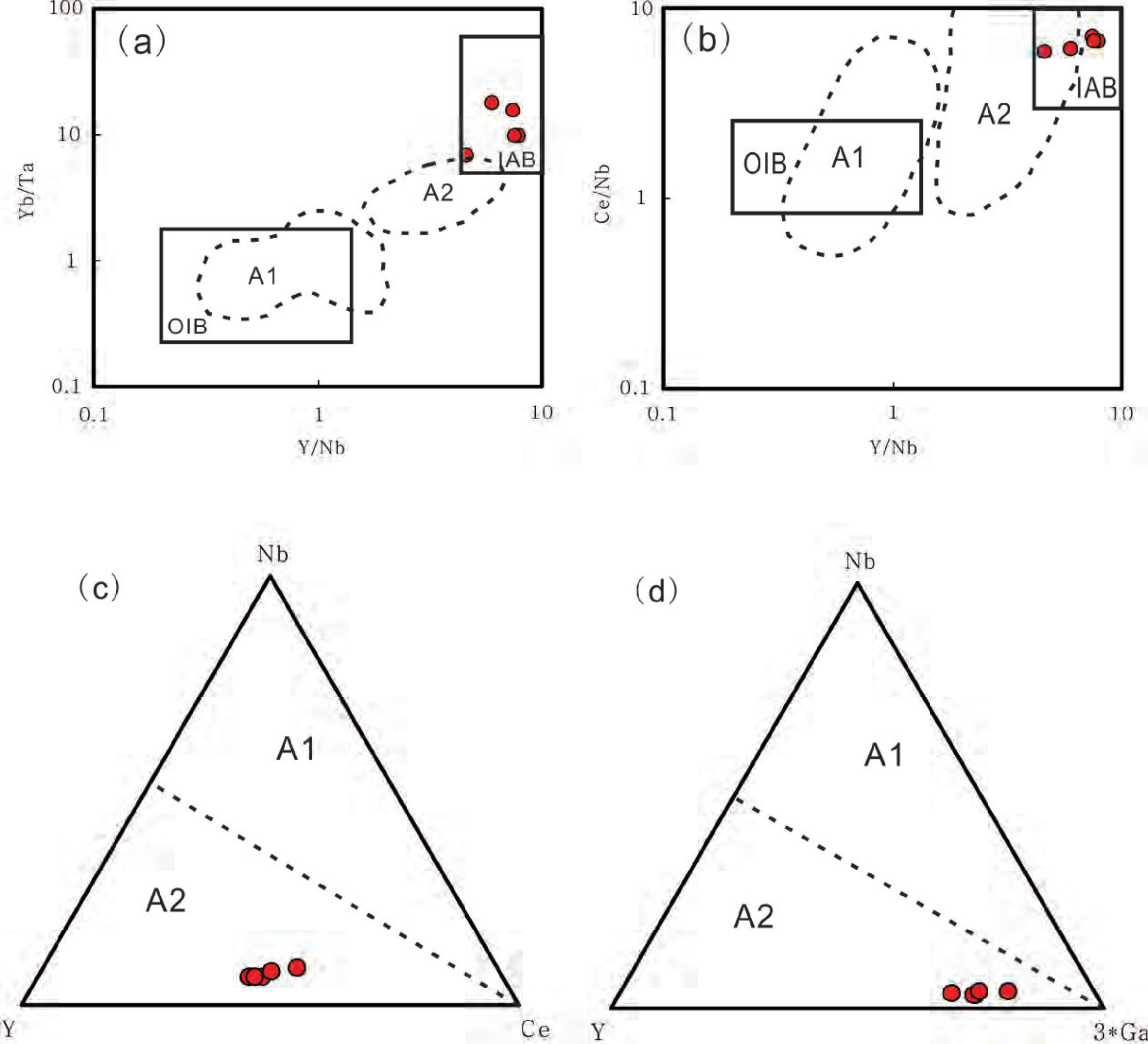

Supplementary Fig. 4. (a). Yb/Ta versus Y/Nb and (b). Y/Nb versus Ce/Nb diagrams (Eby, 1992) for the Bad Vermilion Lake granitic rocks. OIB = oceanic island basalt; IAB = island arc basalt. Fields with dashed lines represent A1- and A2-type granites of Eby (1990). (c) and (d) representative triangular plots showing the areas for A1- and A2-type granitoids. On both diagrams, dashed line corresponds to Y/Nb ratios of 1.2 (Eby, 1992). The granitic rocks of this study plot in the field of A2-type granite.